MULTIWAVELENGTH OBSERVATIONS OF JUPITER TROJANS AND RELATED PRIMITIVE ASTEROID POPULATIONS

By Oriel A. Humes

A Dissertation

Submitted in Partial Fulfillment

of the Requirements for the Degree of

Doctor of Philosophy

in Astronomy and Planetary Science

Northern Arizona University

May 2023

Approved:

Cristina Thomas, Ph.D., Chair

Joshua Emery, Ph.D.

Chadwick Trujillo Ph.D.

William Grundy, Ph.D.

ABSTRACT

MULTIWAVELENGTH OBSERVATIONS OF JUPITER TROJANS

AND RELATED PRIMITIVE ASTEROID POPULATIONS

ORIEL A. HUMES

The distribution of small Solar System bodies preserves a record of both initial conditions within the Solar nebula as well as the subsequent orbital evolution of planetary bodies. As they have undergone little geothermal evolution since their formation, primitive asteroids, including D- & P-type asteroids in the Main Belt and Jupiter Trojan clouds, represent an important reservoir of information about the history of the Solar System. The unique gravitational relationship between Jupiter and its Trojan asteroids closely ties their orbital migration histories together. Similarly, the distribution of D- & P-type asteroids within the Main Belt reveals the extent of delivery of volatile outer Solar System materials to the inner Solar System. Understanding both these processes is critical to telling the story of how our planetary system came to be.

Astronomers use spectroscopy as a tool to understand small bodies on a population level. The characteristic spectral features of asteroids reveal their compositions, and in turn, their origins. Much of asteroid spectroscopy is conducted in the visible and near-infrared (VNIR) due to its accessibility to ground-based telescopes. However, D- & P-type asteroids are red and spectrally featureless in the VNIR region, providing few constraints on the compositional makeup of these critical populations. To address this lack of constraints, I present three spectroscopic investigations of primitive asteroids in the Main Belt and Trojan clouds from the near-ultraviolet to the mid-infrared. Integrating ground-based, space-based, and airborne observations, I present analyses of the spectra of D- & P-type asteroids throughout the Solar System.

In the ultraviolet, I use the Hubble Space Telescope to observe a new spectral feature of the Jupiter Trojans, an increase in reflectance shortwards of 0.35 μm. I use Hapke optical modeling to derive compositional constraints based on this new spectral feature and demonstrate that Rayleigh scattering from submicroscopic opaques, including iron and carbon, can explain this increase in UV reflectance. In the mid-infrared, I combine observations from the Stratospheric Observatory for Infrared Astronomy (SOFIA) and the Spitzer Space Telescope to parameterize the 10- and 20-μm silicate emission feature of Main Belt D- and P-type asteroids, comparing the appearance of this feature in Main Belt asteroids to its appearance in literature spectra of the Jupiter Trojans. I show that asteroids that otherwise appear similar in the VNIR region show a diversity of spectral features in the mid-infrared. In the VNIR, I use the Lowell Discovery Telescope and the NASA Infrared Telescope Facility to search for steeply red-sloped primitive asteroids in the Main Belt. I identify red-sloped asteroids and show that subtle differences in the VNIR spectra of Main Belt red-sloped asteroids suggest multiple sub-populations of red-sloped asteroids are present in the Main Belt.

Copyright

Chapter 2 (Ultraviolet Spectroscopy of Lucy Mission Targets with the Hubble Space Telescope) and Chapter 3 (Comparative Mid-Infrared Spectroscopy of Dark, Primitive Asteroids: Does Shared Taxonomic Class Indicate Shared Silicate Composition?) have been written as papers for submission in *The Planetary Science Journal* and are presented here in manuscript form. At the time of submission, the contents of Chapter 2 are publicly available in Humes et al. (2022) under a Creative Commons Attribution 4.0 license. The version of the manuscript for Chapter 3 was received by *The Planetary Science Jornal* on March 9th, 2023 and is currently under review. The final published version will be similar to the version presented here. Finally, Chapter 4 (The Abundance of Red-Sloped Asteroids in the Main Belt) contains work that will be submitted for peer review. In order to comply with University formatting standards, some of the content has been reformatted as each chapter was written to stand alone.

Acknowledgements

Here is a list of some of the people without whom this dissertation would not exist. Your mentorship, support, and friendship have made my journey to this point possible. First, my family, especially my parents Todd and Lisa Humes, my sister Laura Humes Wahied (who shares her name with an asteroid in Chapter 4), and Mostafa Wahied. A long list of scientific mentors who guided my development as a scientist and communicator include my advisor, Dr. Cristina Thomas; my committee members, Dr. Josh Emery, Dr. Chad Trujillo, and Dr. Will Grundy; current and former NAU colleagues Dr. David Trilling, Dr. Lisa Chien, and Dr. Maggie McAdam; my undergraduate mentors at Caltech, Dr. Mike Brown, Dr. Mark Weidenbeck, and Richard Leske; and Dr. Ana Larson and the volunteers at the Theodor Jacobsen Observatory at the University of Washington. My fellow cohort of graduate students at NAU have been a great source of support over the years. Audrey Martin's advice on mid-infrared spectroscopy was indispensable. Lori Pigue has celebrated many Flagstaff holiday breaks with me over the years and has always been willing to help me out of a tight spot. I'm grateful for Sarah Lamm's constant encouragement, inspiring me to merge my scientific and artistic interests. Colin Orion Chandler and Will Oldroyd provided me with the LaTeX template and saved me many hours of code-wrangling. I'd like to thank my friends from Dabney's extended inter-network who were my go-to test audience: Sophie Piao, Sam Bardwell-Evans, Marcus Bintz, Kenyon Prater, Harel Dor, Danny Wendt, Cayla Dedrick, Brian Bouchard, who were always happy to learn about my favorite asteroids and Homeric heroes.

Table of Contents

List of Tables

List of Figures

Chapter 1
Introduction

Asteroids and other small Solar System bodies are the present-day remnants of planetary formation. Primitive asteroids, e.g. those that have undergone little geological and thermal processing since their formation, are particularly valuable source of information about conditions in the early Solar System. Unlike rocks on large planetary bodies like the Earth, which have undergone significant geothermal reprocessing over their histories, samples of primitive asteroids, such as chondritic meteorites, preserve the bulk chemistry of the region of the Solar nebula in which they condensed (Wood (1988)). These asteroids have not undergone the process of planetary differentiation, which results in the preferential sequestration of certain elements within the planetary interior (McCoy et al. (2006)) Thus, primitive asteroids preserve a relatively faithful record of their original compositions, which can in turn be traced back to the region of the solar nebula where they originally formed.

Population level trends in primitive asteroid compositions have informed our understanding of Solar System formation. The present-day distribution of primitive asteroids is thought to arise from a combination of initial conditions, e.g. the availability of different condensates available at different heliocentric distances (Gradie & Tedesco (1982)), and subsequent dynamical history, e.g. the interaction of asteroids with massive planetary bodies as they form and undergo orbital migration (DeMeo & Carry (2014)). An example that demonstrates the interplay between these two forces is the largest asteroid (1) Ceres: the presence of water ices and ammonia-rich clays on the surface of (1) Ceres suggest that the ice- and ammonia-rich materials on Ceres formed at a much greater distance and then were delivered to its present location at 2.86 AU, at which neither water ice nor ammonia are predicted to have been stable in the early Solar System (De Sanctis et al. (2015)).

One particularly intriguing population of primitive asteroids are the D- & P-type asteroids. These asteroids are characterized by their featureless, neutral to reddish slopes in the visible and near-infrared (DeMeo et al. (2009)) and low geometric albedos (Clark et al. (2004)). Dynamical modeling suggests these D- & P-types initially formed in the outer Solar System, but migrated to their current orbits interior to

or co-orbital with Jupiter during the era of giant planet formation and migration (Levison et al. (2009); Morbidelli et al. (2005)). Jupiter's Trojan clouds are a major reservoir of D- & P- type asteroids (DeMeo & Carry (2013)). These asteroids orbit in a 1:1 mean motion resonance with Jupiter near the L4 and L5 Lagrange points of the Sun-Jupiter system. Their unique gravitational relationship with Jupiter ties their orbital history to the orbital evolution of Jupiter since their capture. Their present observed properties, including distribution in orbital element space and composition, provide strong constraints on hypotheses of Jupiter's formation and orbital evolution, which in turn elucidate the mechanism for their capture into Jupiter's Lagrange regions (e.g. Morbidelli et al. (2005); Nesvorný et al. (2013); Pirani et al. (2019)). D- & P-type asteroids are also common in the middle and outer Main Belt. The specific distribution of D- & P- types within the Main Belt and their relationship to the Trojan D- & P-types depends on the dynamical model proposed to explain the delivery of these materials to the Main Belt (Levison et al. (2009)). Therefore the study of Trojan asteroids and their D- & P-type analogs in the Main Belt has the potential to distinguish between models of the early dynamical history of the giant planets and lead to a deeper understanding of Solar System formation. Understanding how the Jupiter Trojans reveal early Solar System history is a key priority of the recently launched Lucy mission to the Jupiter Trojans. Lucy will be the first spacecraft to visit D- & P-type asteroids anywhere in the Solar System (Levison et al. (2021)).

Spectroscopy is one line of investigation that sheds light on the origins of asteroids. Specific emission and absorption features present in asteroid spectra are signatures of chemical species on their surfaces. The presence of certain chemical species (such as volatiles like the ammoniated clays and water ice on (1) Ceres) are indicative of where in the protosolar nebula asteroidal materials formed (De Sanctis et al. (2015)). In some cases, the inferred initial formation region can be very far from the asteroid's present position. In this way, astronomers use the chemistry of asteroids to trace their orbital evolution. Tracing this history is particularly insightful for asteroids like the D- & P-types, whose present distribution is heavily influenced by the early orbital history of Jupiter. These asteroids preserve direct evidence of dynamical conditions from the earliest era of planetary formation. Unfortunately, the process of interpreting the records preserved by D- & P-type asteroids is frustrated by a lack of diagnostic spectral features in the visible and near-infrared (Emery & Brown (2004)), the region of the electromagnetic spectrum most easily accessible using ground-based observatories. Previous spectral modeling studies of the visible and near-infrared spectra of D- & P-type asteroids have suggested compositions suggestive of, but not unique to, an outer Solar System origin (Sharkey et al. (2019); Gartrelle et al. (2021a); Emery & Brown (2004)).

Fortunately, the development of spectroscopy beyond the visible and near-infrared, aided by the proliferation of space-based observing, has enabled exploration of primitive asteroid spectroscopy in other regions of the electromagnetic spectrum. The Spitzer Space Telescope observed many primitive asteroids in the

thermal mid-infrared. These observations demonstrate that many primitive asteroids including (65) Cybele (Licandro et al. (2011)) and a number of Jupiter Trojans (Emery et al. (2006); Mueller et al. (2010); Martin (2022)) show evidence of silicate emission features at 10- and 20-μm. These features have been interpreted as indicative of very fine grains of silicates in a loose fairy-castle structure (Emery et al. (2006)) or widely separated silicate suspended or dispersed in an optically transparent matrix (Yang et al. (2013); Sultana et al. (2023)). At shorter wavelengths, Brown (2016) reported an absorption feature in the spectra of some Trojans at 3.1 μm, hypothesizing that this feature was due to the presence of ammoniated compounds or fine-grained water frosts. Attention has turned towards ultraviolet spectroscopy as an avenue for constraining the compositions of D- & P-type asteroids. Ground-based observations suggested the presence of an absorption feature in the near-UV (Karlsson et al. (2009); Zellner et al. (1985)), while conceptual models of primitive asteroids hypothesized that materials with detectable UV absorptions could be present on the surfaces of D- & P-type asteroids (Wong & Brown (2016); Yang et al. (2013); Clark et al. (2007)). Following these leads, Wong et al. (2019) examined the near-UV reflectance spectra of six Jupiter Trojans and found a steepening in spectral slope at short wavelengths that was correlated with visible and near-infrared spectral type.

Expanding upon this body of work, I present three investigations of primitive asteroid spectroscopy spanning the electromagnetic spectrum from the ultraviolet to the mid-infrared. In Chapter 2, I use the Hubble Space Telescope to observe a number of Jupiter Trojans that will be visited by the Lucy mission in the ultraviolet. Ultraviolet spectral features can be used to derive novel constraints on the surface compositions of the Trojans. Small opaque scatterers have been hypothesized to explain increased reflectance at blue wavelengths for outer Solar System surfaces including Saturnian moons (Clark et al. (2008, 2012)) and Pluto's Cthulhu Regio (Fayolle et al. (2021)). These particles similar in size to those implicated in space weathering on other airless Solar System bodies (Lucey & Noble (2008); Lucey & Riner (2011)). How the process of space weathering proceeds on the surfaces of D- & P-type asteroids is still unclear. However, understanding the mechanisms that have altered Trojan surfaces since their emplacement can allow us to "turn back the clock" to predict what their surfaces would have looked like billions of years ago and more confidently identify where these asteroids initially formed. I use Hapke optical modeling to explore the hypothesis that the ultraviolet spectral features we observed are due to Rayleigh scattering from microphase particles.

In Chapter 3, I use the Stratospheric Observatory for Infrared Astronomy (SOFIA) and the Spitzer Space Telescope to examine the 10- and 20-μm silicate emission features of D- & P-type asteroids interior to Jupiter in comparison to the Jupiter Trojans. Though the Trojan asteroids lack distinctive absorption features in the visible and near-infrared, the Trojans show distinctive 10- and 20- μm silicate emission features (Emery

et al. (2006); Mueller et al. (2010)). These silicate features in the mid-infrared are diagnostic of a number of mineralogical properties including hydration state (McAdam et al. (2015); Beck et al. (2014); magnesium and iron abundance (Chihara et al. (2002); Koike et al. (1993); Lane et al. (2011)); and amorphous vs. crystalline mineral structure (Martin (2022)). Due to varying physical and chemical conditions within the protosolar nebula, these mineralogical properties are location dependent (Henning (2010)). Using techniques originally developed to measure the silicate emission features of Jupiter Trojans (Martin (2022)), I parameterize the emission features of Main Belt asteroids in the mid-infrared in order to directly compare their spectra to the spectra of the Trojans in order to determine whether the spectral similarity of D- & P-type asteroids in the Trojan and Main Belt populations extends to the mid-infrared. A shared silicate composition as revealed by the silicate emission features of Trojan and Main Belt asteroids would strongly support the idea that these two populations share a common region of origin.

In Chapter 4, I use the NASA Infrared Telescope Facility and the Lowell Discovery Telescope to confirm the steep visible and near-infrared spectral slopes of candidate "red" Main Belt asteroids identified using Sloan Digital Sky Survey (SDSS) Moving Object Catalog (MOC) spectrophotometry. Because many Centaurs and trans-Neptunian Objects (TNOs) have very red ($> 10\%/100nm$) spectral slopes exceeding those of typical D-type asteroids, primitive asteroids in the Main Belt with very red spectral slopes are thought to originate from the same source population as TNOs. This hypothesis is supported by dynamical models that that demonstrate how primitive D- & P-type asteroids originating from the same source population as the TNOs can migrate from the proto-Kuiper Belt to the Main Belt via gravitational interactions with outward-migrating giant planets (Walsh et al. (2012); Levison et al. (2009)). The recent observation of two asteroids Main Belt asteroids with ultra-red spectral slopes (Hasegawa et al. (2021)) resembling TNOs further supports the idea that TNO-like material has been delivered to the Main Belt. The abundance of steeply sloped asteroids confirmed by this survey can be used to place constraints on the delivery of material from the proto-Kuiper Belt to the Main Belt. Close examination of the spectra and orbits of steeply sloped asteroids can shed light on the processes that distribute material implanted into the Main Belt and may challenge the assumption that all steeply red sloped asteroids share a common parent population.

Through these investigations, I further expand spectral coverage of D- & P-type asteroids in the ultraviolet and mid-infrared. I also identify additional small Main Belt D-types and steeply red sloped asteroids that are promising candidates for future studies of outer Solar System material transported from the trans-Neptunian region to the Main Belt. These results together demonstrate the utility of studying asteroid populations across multiple wavelength regions and using correlations between spectral features in disparate wavelength regions to form a more complete understanding of asteroid compositions. Effectively utilizing ground- and

space-based telescopic facilities to understand the chemistry of primitive asteroids contributes to a clear picture of their origins, and in turn, the origins of the Solar System.

Chapter 2

Ultraviolet Spectroscopy of Lucy Mission Targets with the Hubble Space Telescope

The content of this chapter is reproduced from the original version of this manuscript published in the Planetary Science Journal (Humes et al. (2022)). The table formatting has been changed to comply with University requirements, but the text and figures are unaltered. Supplemental data, available in machine-readable formatting, are available at https://iopscience.iop.org/article/10.3847/PSJ/ac8059/meta.

Ultraviolet Spectroscopy of Lucy Mission Targets with the Hubble Space Telescope

Oriel A. Humes[1]; Cristina A. Thomas[1]; Joshua P. Emery[1] ; and Will M. Grundy[1,2]

[1] *Northern Arizona University*

Flagstaff, Arizona

86011, USA

[2] *Lowell Observatory*

Flagstaff, Arizona

86001, USA

(*Received 2022 February 1; revised 2022 July 8; accepted 2022 July 10; published 2022 August 10*)

Submitted to PSJ

ABSTRACT

Corresponding author: Oriel A. Humes
oah28@nau.edu

The recently launched Lucy mission aims to understand the dynamical history of the Solar System by examining the Jupiter Trojans, a population of primitive asteroids co-orbital with Jupiter. Using the G280 grism on the Hubble Space Telescope's Wide Field Camera 3 we obtained near ultraviolet spectra of four of the five Lucy mission targets–(617) Patroclus-Menoetius, (11351) Leucus, (3548) Eurybates, and (21900) Orus–to search for novel spectral features. We observe a local reflectance minimum at 0.4 μm accompanied by an increase in reflectance from 0.35-0.3 μm in the spectra of Patroclus and Orus. We use the principles of Rayleigh scattering and geometric optics to develop a Hapke optical model to investigate whether this feature can be explained by the presence of submicroscopic grains on Trojan surfaces. The near ultraviolet "bump" feature can be explained by scattering due to fine-grained opaques (iron, amorphous carbon, or graphite) with grain sizes ranging from 20 - 80 nm.

Unified Astronomy Thesaurus concepts: Jupiter trojans (874); Near ultraviolet astronomy (1094); Hubble Space Telescope (761); Spectroscopy (1558)

Supporting material: data behind figure

2.1 Introduction

The Jupiter Trojan asteroids, located near Jupiter's L4 and L5 Lagrange points, orbit in 1:1 mean motion resonance with Jupiter. The particular gravitational relationship between Jupiter and its Trojans has been leveraged to provide constraints on the early formation and migration history of Jupiter and other gas giants (eg. Marzari & Scholl (1998); Morbidelli et al. (2005); Nesvornỳ et al. (2013); Pirani et al. (2019)). Any explanation of the emplacement of the Trojan population must account for the physical and orbital properties of the Trojan population as a whole. Thus, understanding the characteristics of the Jupiter Trojan population is of particular interest, as these measurements can provide additional constraints on dynamical models of gas giant formation and migration. Furthermore, as primitive D-, P-, and C- type asteroids (Bendjoya et al. (2004); Roig et al. (2008); DeMeo & Carry (2014)), the Jupiter Trojan population is thought to have undergone very little geothermal processing (such as aqueous alteration) since their emplacement within the Trojan clouds (Lazzarin et al. (1995)). In contrast, geological processing through collisions is thought to play an important role in the evolution of Trojans, with the cutoff between primordial objects and collisional fragments occurring for diameters less than $\sim$ 90 km Binzel & Sauter (1992). The presence of collisional families within the Trojans (including the Eurybates family) provide additional evidence of the importance of collision processes in shaping the Trojan populations Vinogradova (2015); Rozehnal et al. (2016). The higher light curve amplitudes of collisional fragments in the Trojan swarms compared to Main Belt asteroids of the same sizes reported by Binzel & Sauter (1992) may be due to the Trojans being composed of lower-strength

material that is less resistant to collisional fragmentation than Main Belt asteroids. Due to the primordial nature of this population and the potential of further investigation of these objects to answer questions about the early Solar System, the Jupiter Trojans are the targets of the recently launched Lucy mission (Levison et al. (2021)).

Spectroscopy is one line of investigation that provides insight into the nature of the Trojan population. Spectroscopic studies can constrain the chemical composition of Trojan surfaces, which provide clues to their original source population and the changes this population have undergone since their emplacement. In the visible and near infrared (VNIR) region of the spectrum, Trojan asteroids display moderately red sloped, low albedo, featureless reflectance spectra as reported in Emery & Brown (2004). Compared to other populations with red sloped VNIR spectra, the spectral slopes of Jupiter Trojans are relatively moderate, comparable to populations such as the Neptune Trojans, as well as the more neutral-toned Centaurs and scattered disk Kuiper Belt objects (Sheppard & Trujillo (2006)). Among the Jupiter Trojans themselves, there is evidence of two distinct subpopulations: the R (red) and LR (less red) Trojans, which are distinguished by their VNIR spectral slopes (Emery et al. (2010); Wong et al. (2014)). The generally reddish and featureless VNIR slopes of Jupiter Trojans have been interpreted in the literature as due to the presence of anhydrous silicates and a small fraction of complex organics (Emery & Brown (2004)). In particular, Emery & Brown (2004) favor pyroxenes with low (0-40%) iron content. At longer wavelengths, Brown (2016) reports a 3.1 μm feature among LR population asteroids which may be due to either fine-grained water frosts or the N-H stretch. In the mid-infrared, the Trojan asteroids (624) Hektor, (1172) Aneas, (911) Agamemnon, and (617) Patroclus, 10- and 20- μm emission features have been interpreted as being due to fine grained silicates (magnesium rich olivines and pyroxenes) suspended in either a fairy-castle like structure or a medium transparent in this region of the infrared (e.g. Emery et al. (2006); Mueller et al. (2010); Yang et al. (2013)).

Given the limited constraints these features place on the compositions of Trojans, attention has recently turned from the relatively featureless VNIR region of the spectrum to the ultraviolet (UV). Prior ground based spectrophotometry (Karlsson et al. (2009); Zellner et al. (1985)) of the Trojans indicated a potential absorption feature in this region shortwards of 0.4 μm. In addition, Yang et al. (2013) posited that fine grained silicates suspended in a salt matrix could produce the 10-micron silicate emission feature. Similarly, Wong & Brown (2016) invoked H_2S as a coloring agent to explain the VNIR slope bimodality in Trojans. Both of these hypotheses predict an absorption feature in the UV, from salts in the case of the Yang et al. hypothesis (Clark et al. (2007)) and H_2S in the Wong & Brown hypothesis (Wong et al. (2019)). Exploring the H_2S hypothesis, Wong et al. (2019) used the Hubble Space Telescope (HST) to measure UV spectra of a group of six Trojan asteroids. While Wong et al. (2019) did not see evidence of either the salt or H_2S absorption in their spectra, their work showed that the R and LR group Trojans also looked distinct from

Table 2.1. Key properties of observed asteroids.

Name	Taxonomic Class	L_n	Effective Diam. (km)	Albedo	Eccentricity	Inclination (deg)
(617) Patroclus-Menoetius	P	L5	140	0.047	0.139	22.05
(11351) Leucus	D	L4	34.2	0.079	0.064	11.56
(3548) Eurybates	C	L4	63.9	0.052	0.089	8.06
(21900) Orus	D	L4	50.8	0.075	0.037	8.47

Note. — Patroclus-Menoetius is a near equal-size binary: the given diameter is the effective spherical diameter based on NEOWISE observations (Mainzer et al. (2019)). In Levison et al. (2021), the diameters of Patroclus and Menoetius are given as 113 km and 104 km, respectively. Taxonomic classes, eccentricities, and inclinations are also from Levison et al. (2021).

each other in the UV. LR Trojans showed a redder, steeper slope in the ultraviolet than the R Trojans, a reversal of the trend seen in the VNIR. The authors attributed this trend to a difference in either iron or organic content between the two subpopulations (Wong et al. (2019)).

2.2 Methods

2.2.1 Observations & Data Reduction

We used the Hubble Space Telescope (HST) to measure ultraviolet and visible spectra (0.2 - 1.0 microns) of four of the five Lucy mission targets (Eurybates, Leucus, Orus, and the Patroclus-Menoetius binary) during Cycles 25 and 26 as part of programs #15259 and #15504, as summarized in Tables 2.1 and 2.2. Spectra were obtained using the G280 grism on the Wide Field Camera 3 (WFC3) in slitless spectroscopy mode (R$\sim$ 70), along with contemporaneous imagery taken with the F300X filter (Cheng & WFC3 Team (1999)). The FOV of the UVIS camera is a 162" by 162" rhombus when projected on the sky (Dressel (2021)). Because the spectrograph operates in slitless mode and has a large field of view, background sources are also imaged: their contributions to the image are quantified and removed during reduction.

Spectra were reduced using the aXe slitless spectroscopy reduction pipeline (Kümmel et al. (2009)), with a slight modification to account for the non-sidereal motion of the targets across the sky. The pipeline uses Source Extractor (Bertin & Arnouts (1996)) on F300X images to locate all objects, then uses header information about the field of view of subsequent grism images to calculate the pixel location of each object in the generated catalog under the assumption that targets detected in the F300X images do not move in RA and Dec, though their pixel locations may move due to the motion of the telescope. Since our targets

Table 2.2. Summary of HST observations.

Object	Observation Midpoint (UTC)	V (mag)	Phase Angle (deg)	F300x exp. (s)	G280 exp.(s)	Program #
(617) Patroclus-Menoetius	2018-03-31 10:31:23	16.07	5.49	50	1924	15259
(11351) Leucus	2018-08-18 13:01:07	18.04	3.47	100	4228	15259
(3548) Eurybates	2019-08-11 17:18:25	16.99	6.47	10	1848	15504
(21900) Orus	2019-09-03 11:47:11	17.19	4.26	50	1928	15504

Note. — Exposure time refers to the total number of seconds, combining all integrations with the same filter. Note that all observations were taken within 1 orbit with the exception of Leucus, which required 2 orbits due it its relative faintness. Magnitudes and phase angles are from JPL's Horizons database.

move relative to the fixed RA-Dec coordinate system, for each subsequent image we must calculate and correct for the non-sidereal motion of the targets. To calculate this shift, we measured the pixel location of a fixed point in RA and Dec in each F300X and G280 image, then corrected by the difference between these measurements (in pixels) between the F300X and G280 image for the catalog entry corresponding to the asteroid. This method relies on the assumption that the telescope is tracking the target, i.e. that the pixel location of the asteroid does not vary significantly between each image, and can be verified by visual examination of the extracted spectral traces of the asteroids produced by the pipeline. A properly corrected catalog entry is easily identified by an extracted spectral trace that is linear and centered on its brightest pixels.

After each object is located, the reduction pipeline calculates where the spectral trace of each object falls on the chip. The pipeline then extracts the spectrum by projecting a virtual "slit" onto the image, its width and position based on the output of Source Extractor. We used a linear interpolation of the ten pixels on either side of the "slit" to calculate the background contribution, as we did not have master sky images for background subtraction.

Following spectral extraction with aXe pipeline, the data were combined to produce a single spectrum for each object. First, in order to remove potential noise from 0th order background sources that happened to intersect with the spectral trace, outliers were rejected from individual spectra by removing data points that exceeded 5 sigma from the 20 point moving mean box average spectrum. To convert from flux to relative reflectance, we used a solar spectrum from Meftah et al. (2018), smoothed by a 10-point wide Gaussian filter. Then, each spectrum fitted to the solar reference by applying a small (<10 nm) wavelength shift and multiplying by an overall scale factor to produce relative reflectance spectra normalized to unity at 500 nm.

Table 2.3. Summary of LDT observations.

Object	Observation Start (UTC)	V (mag)	Phase Angle (deg)	exp. (s)	Airmass	Standard(s)
(617) Patroclus-Menoetius	2019-06-25 04:33	16.51	9.96	1800	1.47	Land. 105-56 (G5V)
(21900) Orus	2021-11-13 04:34	17.01	10.71	1200	1.07	Land. 93-101 (G5V) HD 9986 (G2V)

Note. — Exposure time refers to the total number of seconds, combining all integrations. For Patroclus-Menoetius, no local standard was used, as the solar analog was at the same airmass as the asteroid. For Orus, both a local and solar standard were used to calibrate the reflectance spectrum. Spectral types for standard stars are from Marsset et al. (2020) and the SIMBAD database Wenger et al. (2000) Magnitudes and phase angles are from JPL's Horizons database.

The shifting step was performed to account for sub-pixel wavelength shifts to ensure proper alignment of narrow solar lines in the UV. This step is analogous to fitting subpixel shifts to align and correct for telluric absorption in ground based data. The final combined spectrum was produced by taking the mean of all measurements within 5 sigma of the median reflectance value to reject artifacts that affect individual frames.

In addition to taking UV spectra with the Hubble Space Telescope, we also obtained visible (0.35 - 1.0 microns) spectra of (617) Patroclus and (21900) Orus using the Lowell Discovery Telescope's DeVeny spectrograph (Bida et al. (2014)). Observations were taken using the DV1 grating (150 lines/mm, R∼450) and 3.0" slit. Observing circumstances are summarized in Table 2.3. Observations of each Trojan were accompanied by observations of standard stars bracketing the asteroid observation. Spectra were processed using the SPECTROSCOPYPIPELINE (SP) developed by Devogele & Moskovitz (2019) for the DeVeny spectrograph, which performs bias and flat correction, cosmic ray subtraction, wavelength calibration, telluric and solar correction. The extracted spectra were then smoothed and binned using a 10-point wide box filter.

2.2.2 Hapke Modeling

In order to investigate possible spectral features in our UV spectra, we constructed a model based on the Hapke model (e.g. Hapke (1981, 1993)) to produce simulated geometric albedo spectra at zero phase angle and without opposition surge. Our unscaled relative reflectance spectra obtained by HST were first scaled by a constant factor to convert them into geometric albedoes using data available from the literature. For (617) Patroclus, our reflectance measurements were scaled to the geometric albedo spectrum used in Emery & Brown (2004) using a simple chi-squared (χ^2) minimization routine to splice the visible range of our

observations to the existing VNIR spectrum of Patroclus, resulting in an albedo of 0.0471 at 550 nm. For (21900) Orus and (3548) Eurybates, we took the visual albedoes (0.075 and 0.052, respectively) reported in Grav et al. (2012) as the values of the geometric albedo at 550 nm and scaled our observations accordingly. Similarly, we scaled the spectrum of (11351) Leucus to the visible albedo (0.037) reported in Buie et al. (2021) at 550 nm. Using zero-phase angle geometric albedos as the output of our Hapke models both simplified the calculations required to obtain a spectrum and allowed us to incorporate albedo into our compositional fits, a constraint that is particularly important to include for relatively featureless spectra such as those of the Trojans in the VNIR as pointed out in Emery & Brown (2004).

Our spectral model simulates two different scattering regimes by calculating the single scattering albedo w from the real (n) and imaginary (k) indices of refraction and particle diameter d. Following the methods in Fayolle et al. (2021), we calculate the single scattering albedo in two different regimes: the Rayleigh scattering regime (Equations 2.1 through 2.4) and the geometric optics regime (Equations 2.5 through 2.10). For particles that are small compared to the wavelength of light ($\frac{\pi d}{\lambda} < 1$), we are in the Rayleigh scattering regime and obtain the single scattering albedo $w_{Rayleigh}$ (Equations 5.9, 5.13-5.14 in Ch 5. of Hapke (1993)) using

$$w_{Rayleigh} = \frac{Q_S}{Q_E}, \tag{2.1}$$

where

$$Q_E = \frac{24nk}{(n^2+k^2)^2 + 4(n^2-k^2) + 4} X \tag{2.2}$$

$$Q_S = \frac{8}{3} \frac{\left((n^2+k^2)^2 + n^2 - k^2 - 2\right)^2 + 36n^2k^2}{((n^2+k^2)^2 + 4(n^2+k^2) + 4)^2} X^4 \tag{2.3}$$

$$X = \frac{\pi d}{\lambda}. \tag{2.4}$$

For the Rayleigh regime, we capped the value of the single scattering albedo at 1, as a single scattering albedo larger than 1 is unphysical. For particles that are large compared to the wavelength of light (eg. $\frac{\pi d}{\lambda} \geq 1$), we are in the geometric optics regime and use the following equations to obtain the single scattering albedo $w_{Geometric}$. For particles that are large compared to the wavelength of light, $Q_E = 1$ Hapke (1981), and thus $w_{Geometric} = Q_S$ (Equations 2.69, 5.42, 6.39-6.41 of Hapke (1993)). To calculate the the single scattering albedo in the geometric optics regime, we use

$$w_{Geometric} = \frac{Q_S}{Q_E} = S_e + (1 - S_e), \frac{(1 - S_i)}{1 - S_i\Theta}\Theta \tag{2.5}$$

where

$$S_e = \frac{(n-1)^2 + k^2}{(n+1)^2 + k^2} + 0.05 \tag{2.6}$$

$$S_i = 1 = \frac{4}{n(n+1)^2} \tag{2.7}$$

$$\Theta = \exp(-\alpha\langle D\rangle) \tag{2.8}$$

$$\langle D\rangle = \frac{2}{3}\left(n^2 - \frac{1}{n}(n^2-1)^{3/2}\right)d \tag{2.9}$$

$$\alpha = \frac{4\pi k}{\lambda}. \tag{2.10}$$

For a modeled surface with i compositional components, each with grain diameter d_i, mass mixing ratio m_i, and density ρ_i, the average single scattering albedo can be computed from the single scattering albedos w_i of the individual components via the following equation (Equation 17 in Hapke (1981)), regardless of scattering regime,

$$w = \frac{\sum_i \frac{m_i}{\rho_i d_i} w_i}{\sum_i \frac{m_i}{\rho_i d_i}}. \tag{2.11}$$

The single scattering albedo w can be combined with the multiple scattering function H, backscattering function B, and phase function P to produce the bidirectional reflectance (Equation 16 from Hapke (1981)) using

$$r(\mu, \mu_0, g) = \frac{w}{4\pi}\frac{\mu_0}{\mu_0 + \mu}\left((1 + B(g))P(g) + H(\mu_0)H(\mu) - 1\right). \tag{2.12}$$

Here, μ, μ_0 and g are geometric factors with $\mu = \cos e$ and $\mu_0 = \cos i$, where e, i are the angles of exitance and incidence, respectively. To simplify our model, we took $B = 0$ and $P = 1$, as in the case for isotropic scatterers with no opposition effect. These assumptions were shown in Emery & Brown (2004) to result in effective models of Trojan surfaces in the VNIR. The H (Equations 8, 10 from Hapke (1981)) function is

Table 2.4. Hapke model compositional compnents and their densities

Composition	Density (g/cm^3)	Source(s)
H_2O Ice	0.82	Warren (1984); Westley et al. (1998)
CO_2 Ice	0.98	Warren (1986); Luna et al. (2012)
NH_3 Ice	0.47	Martonchik et al. (1984); Luna et al. (2012)
Fe	7.874	Cahill et al. (2012)
Pyroxene 2 ($f_{Mg} = 1$)	3.21	Dorschner et al. (1995); Emery & Brown (2004)
Pyroxene 4 ($f_{Mg} = 0.8$)	3.36	Dorschner et al. (1995); Emery & Brown (2004)
Pyroxene 5 ($f_{Mg} = 0.7$)	3.43	Dorschner et al. (1995); Emery & Brown (2004)
Pyroxene 6 ($f_{Mg} = 0.6$)	3.51	Dorschner et al. (1995); Emery & Brown (2004)
Olivine 1 ($f_{Mg} = 0.5$)	3.81	Dorschner et al. (1995); Emery & Brown (2004)
Olivine 2 ($f_{Mg} = 0.4$)	3.92	Dorschner et al. (1995); Emery & Brown (2004)
Titan Tholin	1.5	Khare et al. (1984)
Tholin/H_2O Mix	1.5	Khare et al. (1993)
Graphite	2.26	Draine (1985)
Amorphous Carbon	1.85	Rouleau & Martin (1991)

Note. — For entries with multiple citations, the first citation is the source of the optical constants followed by the source of the density. In cases with only one citation, the source contains both optical constants and material densities with the exception of the tholin mixtures, for which we assume a density of 1.5 following Emery & Brown (2004) and iron, for which the density of elemental iron was used. For the olivines and pyroxenes, we adopt the labeling scheme of Emery & Brown (2004) to keep track of silicates with different magnesium-iron ratios. For these silicates, the magnesium fraction f_{Mg} gives the fractional magnesium content of each sample such that the chemical formula for the pyroxenes is given by $Mg_{f_{Mg}}Fe_{1-f_{Mg}}SiO_3$ and the olivines by $Mg_{2f_{Mg}}Fe_{2-2f_{Mg}}SiO_3$

approximated as

$$H(\mu) = \frac{1 + 2\mu}{1 + 2\gamma\mu}, \tag{2.13}$$

where

$$\gamma = \sqrt{(1 - w)}. \tag{2.14}$$

To obtain the geometric albedo at a phase angle of zero from the bidirectional reflectance function, a numerical integration of the bidirectional reflectance function over 100 rings was performed by subdividing a spherical surface into areas with $\mu_i = \mu_e$, then summing the contribution to reflectance from each ring, weighted by projected cross sectional area as viewed face on.

The sources of optical constants (n and k) for the surface compositions used in the Hapke model are summarized in Table 2.4. Optical constants were interpolated to the wavelengths of our observations. For certain materials with k values that span several orders of magnitude, values of the real part of the optical constants were interpolated linearly in $\log \lambda$, n space, and the imaginary part of the optical constants were

interpolated linearly in $\log \lambda$, $\log k$ space as noted in Warren (1984, 1986), otherwise, optical constants were linearly interpolated in λ, n and λ, k space.

The compositions used to model the Trojan spectra were drawn from the results of previous Hapke modeling of Trojan spectra in the VNIR (eg. Emery & Brown (2004)). In addition to the silicate, organic, and tholin compositions suggested by previous literature, additional ice species (H_2O, CO2, and NH3) were chosen as potential Rayleigh scatterers based on laboratory measurements by Hapke et al. (1981). Ices were also chosen for their potential to explain the 3.1 micron absorption feature. Brown (2016) suggested the feature could be due to either very fine grained water frosts or species with the N-H stretch. Thermal modeling of the Trojans by Guilbert-Lepoutre (2014) has indicated that water ice may be present as a surface or near-surface component at depths ranging from $\sim$ 10 cm to $\sim$ 10 m depending on albedo, thermal inertia, and orbital characteristics of the asteroid. For low-obliquity Trojans, it is also possible that water ice is present at the surface near the poles. Thus, water ice is a plausible surface component to include in our modeling efforts. We include CO_2 and NH_3 as possible compositions due to the spectral similarities of Jupiter Trojans to comets (Ye et al. (2016); Kelley et al. (2017)), though we note that in pure ice form CO_2 and NH_3 are likely not currently stable on or near Trojan surfaces in the present day (Wong & Brown (2016)). Though altered residues from these ices may be present as surface components of Trojans (Brown (2016)), our model is limited in that it can only test for the presence of the unaltered ices. Additional opaque species, including iron and carbon, were also chosen as Rayleigh scatterers due to their hypothesized roles in space weathering and particular features in the UV (see Pieters et al. (2000); Cloutis et al. (2008); Hendrix et al. (2016).)

To obtain best-fits, the model was fed an initial "guess" composition based on adding a Rayleigh scattering species to the compositions of the best fit models in Emery & Brown (2004). The initial guess was then refined by allowing the particle diameters and mass mixing ratios (mass fraction relative to the abundance of the first composition, which was fixed at a mixing ratio of 1) to vary until the reduced χ^2 value of the difference between data and model was minimized. The model can also evaluate the χ^2 metric for any input composition without attempting to determine the best fit in order to quantify how changing variables such as particle size affects the shape of the resulting spectrum. For this modeling effort, we focused on three-component surface models, generally consisting of silicates, a Rayleigh scatterer, and an additional component. The addition of a fourth component did not significantly improve the goodness of the model fit.

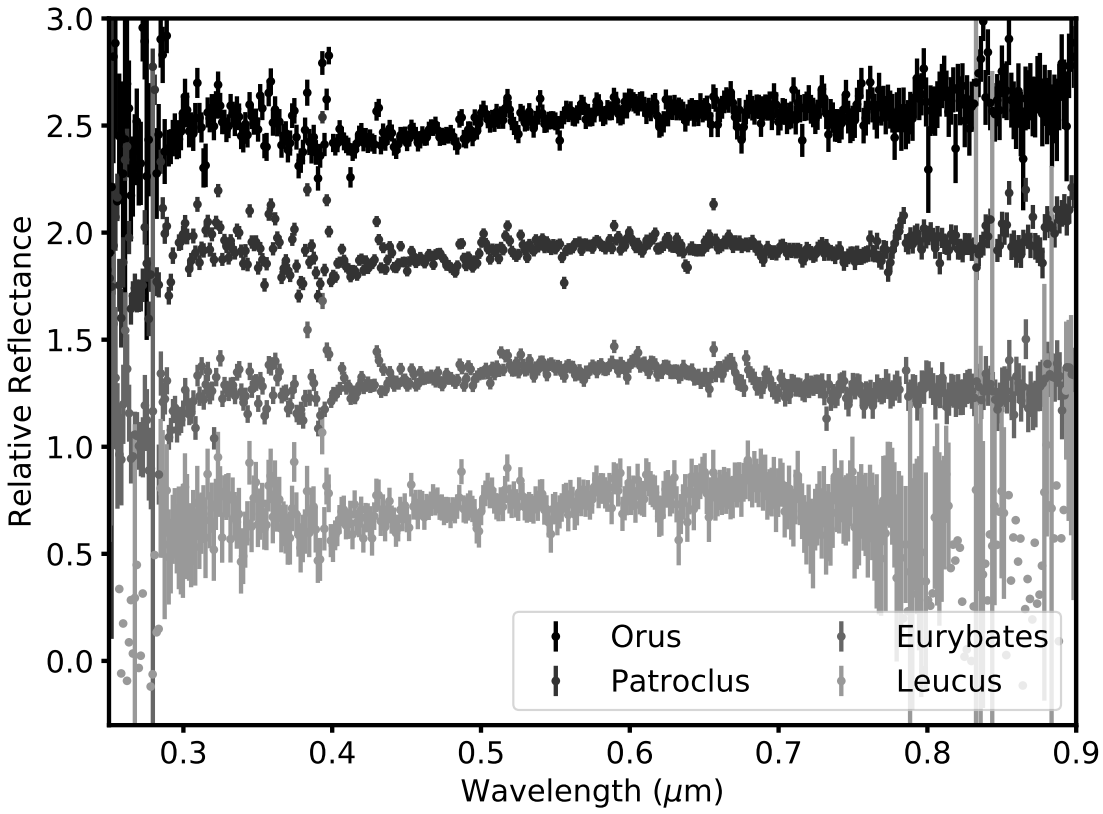

Figure 2.1 Ultraviolet and visible spectra of Orus, the Patroclus-Menoetius binary, Eurybates, and Leucus from the Hubble Space Telescope. Spectra are normalized to 0.5 μm and offset for clarity.

2.3 Results

The spectra of our four targets, normalized to 0.5 μm and offset for clarity are shown in Figure 2.1. While the visible spectra of the Trojans as observed by Hubble are fairly consistent with previous observations of these targets, we note that in the spectrum of Patroclus and Eurybates, there is a shallowing of slope and subsequent downturn in reflectance from 0.6-0.7 μm, as compared to the steeper slopes of the 0.4-0.6 μm region of the spectrum. Similar features have been reported in the spectrum of Eurybates (Souza-Feliciano et al. (2020)) and some Eurybates family members (Fornasier et al. (2007)). However, visible spectra of Patroclus including those in Emery & Brown (2004) and our LDT spectra (See Fig 2.2) do not show this downturn. Given that Patroclus is not a member of the Eurybates family and is typically classified as a P type rather than a C type asteroid, we do not expect similar features to appear in the spectra of both Patroclus and Eurybates. This feature may be due to instrumental issues at the long wavelength end of the G280 grism range, as higher spectral orders begin to overlap with the brightest spectral trace, as noted in Wakeford et al. (2020), though this explanation does not explain why this feature would be present in the spectra of some of our targets and not others. It is possible that this feature appears in the spectrum of Patroclus due to rotational variability in appearance, as seen with Eurybates by Souza-Feliciano et al. (2020). To assess what portions of the surfaces of Patroclus and Menoetius are observed at different times, we define a lat,lon coordinate system for Patroclus based on the Patroclus-Menoetius circular mutual orbit solution from Grundy et al. (2018). The positive pole is defined by the angular momentum vector of the mutual orbit. Zero longitude is defined by the direction from Patroclus to Menoetius, which is constant if the mutual orbit has been tidally circularized, the two bodies' spins are tidally locked to their orbit, and no libration occurs. The coordinate system assumes a spherical shape for Patroclus and is not distorted to account for its elongation into a triaxial ellipsoid. This coordinate system is analogous to that used for Pluto, where the mean direction to Charon defines zero longitude. Accounting for light time, we then compute the sub-Earth latitude and longitude on Patroclus at the mean time of each observation as a way of evaluating what hemispheres of the bodies were oriented toward Earth at the time of the observations. Using this method, we find the sub-earth latitude and longitude for the HST observations are +10.9, 26.5 and the sub-earth latitude and longitude for the LDT observations are -8.1, 280.2. These observations are separated by $\sim 106^{\circ}$, lending support to the interpretation that the difference in Patroclus's long wavelength spectrum may be due to a difference in viewing geometry between the two observations. In both these geometries, both Patroclus and Menoetius are visible (i.e. neither is eclipsing the other), though we cannot resolve the individual components in our imagery.

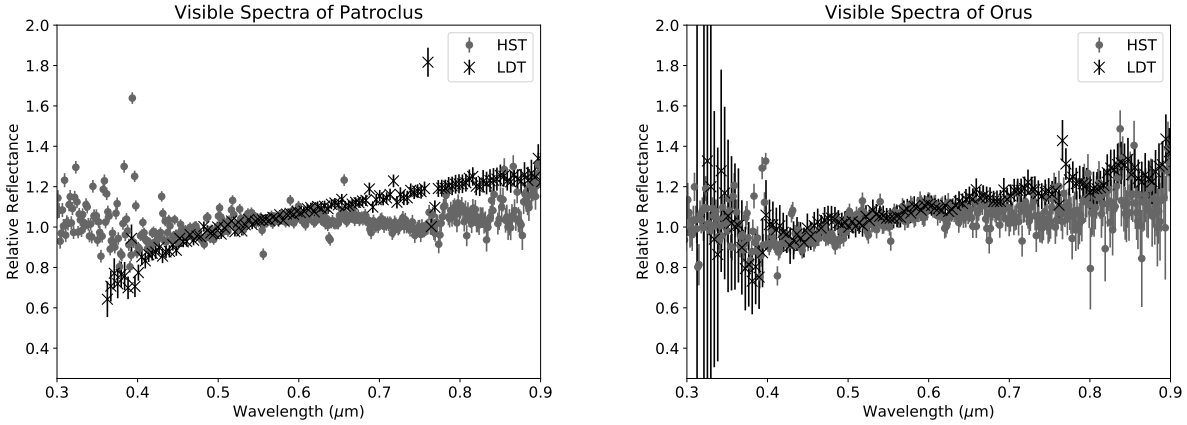

Figure 2.2 Visible spectra of Patroclus (a) and Orus (b) as observed by the Hubble Space Telescope (HST) and the Lowell Discovery Telescope (LDT). Spectra were normalized at 0.5 μm. The observed slopes of Patroclus in the 0.4-0.55 μm region agree for the two observations, but the HST spectrum shows a flattening in reflectance starting at 0.55 μm that is not seen in the LDT spectrum. Because this feature has not been reported in the spectrum of Patroclus before, it may be due to instrumental error or rotational variability (see text). In the same wavelength region, the two spectra of Orus are in better agreement.

Table 2.5. Results of Monte Carlo test for the "bump" feature

Asteroid	Mean Slope (10^{-5} per μm)	Slope Standard Deviation (10^{-5} per μm)	Bump?
(617) Patroclus-Menoetius	-6.3	1.3	Yes
(11351) Leucus	1.0	5.6	No
(3548) Eurybates	4.7	1.8	No
(21900) Orus	-6.0	2.8	Yes

Note. — For each asteroid, 10,000 synthetic spectra were produced and slopes fit to the 0.3-0.4 μm region to estimate the slope and slope error in the near UV (see text). We consider a spectrum to show the "bump" feature if an asteroid has a negative slope significant at the 2-sigma level.

In the ultraviolet, the spectra do not show evidence of absorption features, including the salt feature that would support the hypothesis of Yang et al. (2013) or the H_2S feature predicted by Wong & Brown (2016). However, the spectra of Orus and Patroclus show a local reflectance minimum at around 0.4 μm, followed by an increase in reflectance from 0.3 - 0.35 μm, which we refer to as the "bump" feature. To determine whether an asteroid spectrum showed evidence of the bump feature, we used a Monte Carlo approach. For each asteroid, we produced 10,000 synthetic spectra by drawing reflectance values for each wavelength from a Gaussian distribution with a mean equal to the reflectance and standard deviation equal to the error. Then, for each synthetic spectrum, we fit a line to the 0.3-0.4 μm region and measured its slope. Applying this method to all four asteroids (See Table 2.5), we find that Orus and Patroclus have negatively (e.g. blue) sloped reflectances at a confidence level of 2 sigma. Using this same method, Eurybates has a positively sloped (e.g. red) reflectance spectrum in this region at the 2 sigma level, while Leucus has an ambiguous or neutral slope at the 2 sigma level.

We used Hapke modeling in order to investigate whether this potential new feature in the near-UV can be explained by Rayleigh scattering due to fine grained particles on the surfaces of these two asteroids. Because Orus and Patroclus show this feature according to our Monte Carlo analysis, we focus our analysis on these two asteroids in particular. To account for the difference in Patroclus spectra from the HST and LDT, we fit models to two different versions of the spectrum: the unaltered spectrum from the Hubble Space Telescope (Patroclus a); and a spectrum constructed by splicing together short wavelength HST spectra and long wavelength LDT spectra at 0.55 μm (Patroclus b). We fit our model to the 0.25 - 0.8 micron range, excluding regions with large amounts of noise and point-to-point scatter. Our five best fitting models, as evaluated by minimum reduced χ^2, are summarized in Tables 2.6a and 2.6b. In general, Orus is well modeled by a three component spectral model consisting of a pyroxene, an opaque Rayleigh scatterer, and a third darkening component, the composition of which can vary. Patroclus shows consistently worse-fitting models, which may be due to spurious features in its visible spectrum, or its relatively smaller error bars.

For all of our best fit models (e.g. Fig 2.3), Pyroxene 5 and Pyroxene 2 are the most prominent silicates in the spectrum. The grain size of the pyroxenes is largely responsible for setting the gradient of the spectral slope in the visible: larger grain sizes result in stronger absorption in the blue, and steeper slopes. This finding is consistent with the results of Emery & Brown (2004), which found that silicates mixed with low albedo materials (such as organics) can reproduce the red slopes and low geometric albedos of the Trojans. The grain size of the Rayleigh scattering species is responsible for the spectral contrast and wavelength at which the "bump" feature begins to appear (see Figure 2.4). Similarly, the grain size and abundance of the third component in our models helps to set the overall geometric albedo. This component is generally a darkening agent like iron or amorphous carbon, or an additional pyroxene. In general, while Pyroxene 5 was

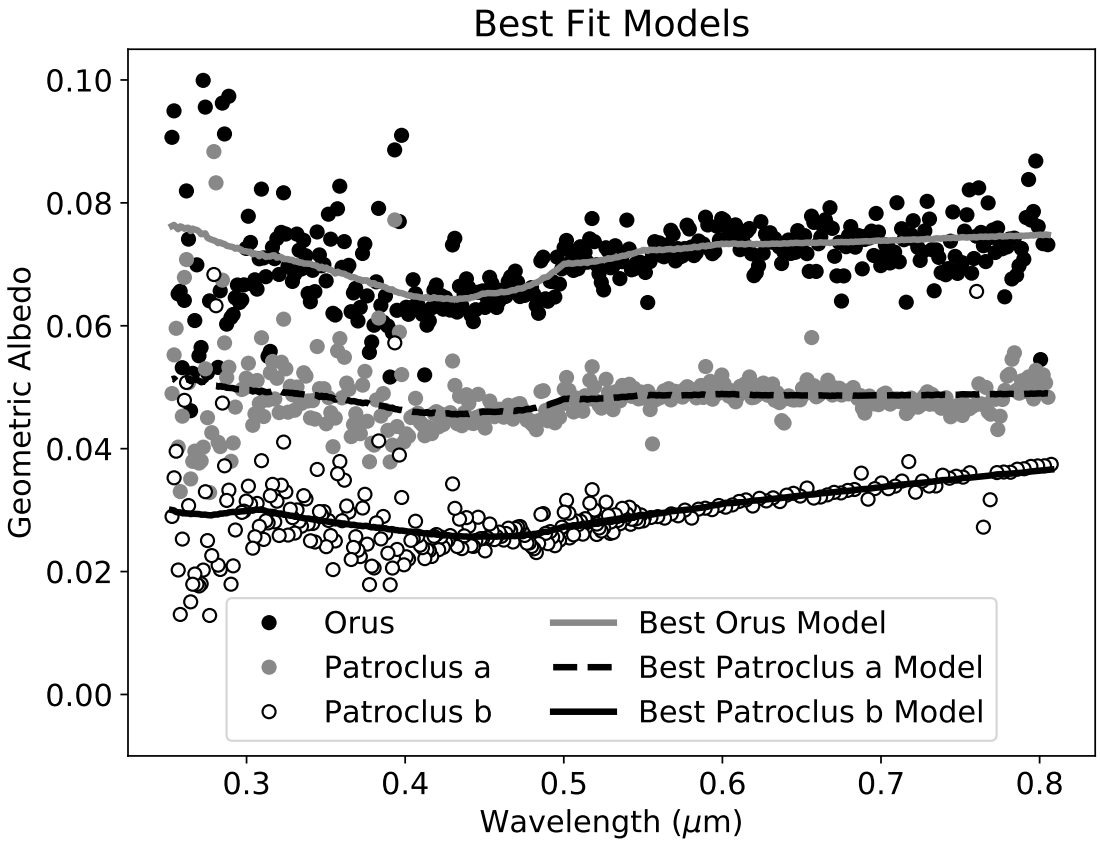

Figure 2.3 Best fit models for Orus and Patroclus (solid and dashed lines) plotted alongside geometric albedo data from HST and LDT observations (filled and open circles). The spectrum for Patroclus a uses only HST data, while the spectrum for Patroclus b uses HST data for short wavelengths ($< 0.55\mu$m) spliced with LDT data at longer wavelengths ($> 0.55\mu$ m). Patroclus b is offset for clarity. See tables 2.6a and 2.6b for details on the best fit models.

Table 2.6a. Best fit optical models for 21900 Orus and their compositions

Model	Comp.	Particle Diam. (μm)	Mixing Ratio	Reduced χ^2
Orus 1	Pyroxene 5	4.64	1.00	1.67
	Iron	0.06	0.05	
	Iron	0.43	0.14	
Orus 2	Pyroxene 5	4.66	1.00	1.68
	Iron	0.06	0.05	
	Pyroxene 2	13.1	1.34	
Orus 3	Pyroxene 5	4.19	1.00	1.70
	Iron	0.08	0.03	
	Amorph. C	4.51	0.54	
Orus 4	Pyroxene 5	4.02	1.00	1.73
	Amorph. C	0.04	0.02	
	Pyroxene 2	10.2	4.90	
Orus 5	Pyroxene 5	4.02	1.00	1.73
	Graphite	0.06	0.02	
	Iron	1.86	2.50	

Note. — The top 5 best fitting models for Orus. For each model we give the compositional components, their diameters, and mixing ratios. Amorphous carbon is abbreviated in this table as Amorph. C.

present in all the best fit spectra presented here, silicates of other compositions, including other pyroxenes and olivines, could be substituted as the primary silicate component, though these compositions did not match the observed spectra as well. The fine grained Rayleigh scatterers in our models are all opaques (eg. iron, carbon), rather than ices. While our best fitting models use iron as a Rayleigh scatterer, amorphous carbon and graphite can both be substituted as Rayleigh scatterers to provide a good fit. Though not the main focus of our modeling efforts, we also find that the inclusion of 0.01-0.02 (mass mixing ratio, compared to pyroxene) of iron Rayleigh scatterers can improve compositional models of Leucus in particular, but the inclusion of Rayleigh scatters is not required to explain the spectral shapes of Leucus and Eurybates among the best fit models for these asteroids.

Table 2.6b. Best fit optical models for (617) Patroclus-Menoetius and their compositions

Model	Comp.	Particle	Mixing Diam. (μm)	Reduced Ratio	Model χ^2	Comp.	Particle Diam. (μm)	Mixing Ratio	Reduced χ^2
Pat. 1a	Pyroxene 5	4.38	1.00	6.37	Pat. 1b	Pyroxene 5	6.60	1.00	8.05
	Iron	0.05	0.09			Iron	0.08	0.02	
	Iron	1.84	0.93			Amorph. C	0.29	0.12	
Pat. 2a	Pyroxene 5	3.53	1.00	6.39	Pat. 2b	Pyroxene 5	10.5	1.00	8.08
	Iron	0.08	0.04			Amorph. C	0.04	0.01	
	Amorph. C	0.92	0.62			Iron	0.60	0.22	
Pat. 3a	Pyroxene 5	4.33	1.00	6.43	Pat. 3b	Pyroxene 6	0.80	1.00	8.09
	Iron	0.04	0.12			Iron	0.08	0.19	
	Pyroxene 2	0.84	0.25			Amorph. C	0.43	1.38	
Pat. 4a	Pyroxene 5	3.98	1.00	6.56	Pat. 4b	Pyroxene 5	10.6	1.00	8.11
	Amorph. C	0.03	0.06			Graphite	0.05	0.01	
	Pyroxene 2	0.25	0.29			Iron	0.32	0.11	
Pat. 5a	Pyroxene 5	3.63	1.00	6.56	Pat. 5b	Pyroxene 6	1.19	1.00	8.13
	Graphite	0.04	0.06			Amorph. C	0.04	0.08	
	Iron	0.86	2.06			Iron	0.65	3.13	

Note. — The top 5 best fitting models for Patroclus. We present two versions of the Patroclus spectra: Pat. a models were fit to Hubble Space Telescope data; while Pat. b models were fit to the Hubble Space Telescope data at short wavelengths ($< 0.55\mu m$) spliced with data from the Lowell Discovery Telescope at long wavelengths ($> 0.55\mu m$). For each model we give the compositional components, their diameters, and mixing ratios. Amorphous carbon is abbreviated in this table as Amorph. C.

To quantify error in particle diameter and mixing ratios, we generated a large number of synthetic spectra drawn from Gaussian distributions for each data point with a mean equal to the observed geometric albedo and standard deviation equal to the error in albedo. Then, the best fit model was fitted to each synthetic spectrum using the same model components to determine the scatter in particle diameter and mixing ratio. The resulting differences in particle diameter and mixing ratio only appeared in the third or fourth significant figures of each model parameter. This error is negligible compared to systematic errors arising from model assumptions.

In order to better understand the range of possible model parameter values, we vary model parameters individually and compute how the spectrum and value of χ^2 changes when the parameter is varied by small ($\sim$1-10%) increments about the best fit model. In particular, we are interested in the range of possible sizes for the Rayleigh scattering component, which is responsible for the shape of the spectrum in the UV, as other modeling efforts have addressed the range of possible compositions responsible for the visible and near infrared spectra of Jupiter Trojans (Cruikshank et al. (2001); Emery & Brown (2004); Sharkey et al. (2019); Gartrelle et al. (2021a)). We focus on the five best-fit models of Orus in order to understand the range of possible Rayleigh scatterer sizes due to Orus's overall better fit to the model. We identified the Rayleigh scatterer grain sizes for which each model has a χ^2 statistic of 2 or smaller, since all models with a χ^2 statistic less than 2 produce optical models with geometric albedos that fall within the range of the scatter observed in the spectrum of Orus. Using this method, we find that the Rayleigh scatterers can be 0.001 - 0.002 μm larger or smaller and still provide a reasonable fit.

We note that the main source of error in our model is due to model limitations. In reality, Trojan surfaces are much more complex than a simple three component model. There will be grain size variation among each component and surface in-homogeneity, which is not accounted for in our model.

2.4 Discussion

In the most general terms, the compositional mix of our best fit models include a silicate, darkening agent, and a Rayleigh scatterer. This mixture agrees with previous modeling efforts for Jupiter Trojans and dark (D type) asteroids. Both Emery & Brown (2004) and Gartrelle et al. (2021a) find that Trojans are well modelled by silicates mixed with opaques. However, unlike Emery & Brown (2004) and Gartrelle et al. (2021a), we include iron on its own as a darkening agent. Cruikshank et al. (2001) report including iron sulfide (as an analog for metallic iron) as a component in their modeling but find no reason to prefer FeS as a component in comparison to their magnesium-rich pyroxene models. Like Emery & Brown (2004), we find that the red slopes of the Trojans can be accounted for with silicates alone, without needing to invoke

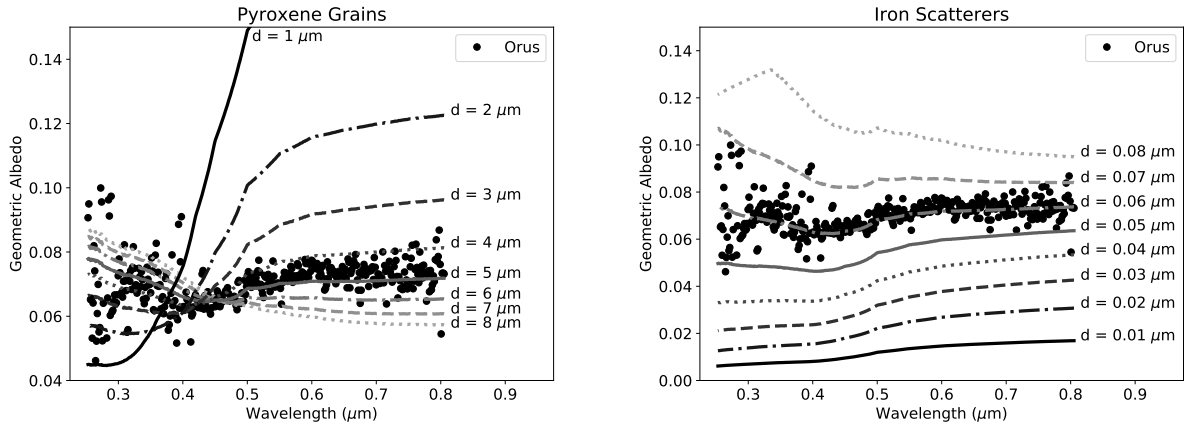

Figure 2.4 The effect of changing grain sizes of different components of the best fit model for Orus (See Table 2.6a, Orus 1). Changing the grain size of the pyroxene in this model (panel a) controls the magnitude of the slope in the visible and the extent of absorption in the UV. Changing the grain size of the iron scatterers in this model (panel b) controls the spectral contrast of "bump" feature in the UV, as well as the wavelength at which the spectrum begins to brighten. The spectrum of Orus is also shown for reference purposes, without error bars for clarity–note that the scale used to display the finer details of the spectra cuts off one prominent outlier.

organic components (e.g. tholins) in large quantities, in contrast with Sharkey et al. (2019), which used Triton tholins as a primary component. In Gartrelle et al. (2021a) phylosilicates provide the best fits for D type asteroid spectra, with opaque species masking characteristic absorption features. We were unable to test phylosilicates as silicate materials since optical constants in the near-UV are not publicly available for relevant phylosilicate species. However, like Emery & Brown (2004), we find that while other silicate species can be substituted for pyroxene and still produce a reasonable fit, the best fits contained anhydrous silicates. Whether the Trojans are composed of hydrous or anhydrous silicates is an open question which this study does not have sufficient scope to answer, but may be addressed by the recently launched Lucy mission (Levison et al. (2021)). Silicates have previously been observed in the spectra of Trojans; in particular, the silicate emission features at 10 and 20 microns have been noted by Emery et al. (2006) and Mueller et al. (2010).

Our spectra also show evidence of a new spectral feature in the near-UV–the "bump" that is present in the spectra of Orus and Patroclus. Based on the spectra presented here, the presence of this "bump" feature is not correlated with VNIR spectral properties of these asteroids: Orus is a member of the R group and Patroclus is a member of the LR group and both display this feature. Leucus is an R group asteroid and Eurybates is a more neutral-toned C type asteroid and neither asteroid displays the feature. Our findings contrast with the findings of Wong et al. (2019), who examined a sample of six Trojan asteroids ((1143)

Odysseus, (624) Hektor, (3451) Mentor, (659) Nestor, (911) Agamemnon, and (1437) Diomedes). Wong et al. (2019) observed that slope features in the UV show a correlation to VNIR slopes: redder asteroids in the VNIR tended to have shallower slopes in the UV than their less-red counterparts, which showed a steepening in spectral slope starting around 0.45 μm. Not only do we not observe this slope reversal trend among our sample, we do not observe the "bump" feature in the spectra of Wong et al. (2019), though their spectra examine the same region at sufficient resolution to detect the "bump." Applying the same Monte Carlo approach to quantifying the "bump" feature to the spectra from Wong et al. (2014), we find all asteroids in their sample are positively sloped (e.g. red) in the 0.4-0.3 μm region of the spectrum at the 2 sigma level. Taken together, our results and those of Wong et al. (2019) suggest a diversity of UV spectral features among the Trojans.

Based on the results of Hapke modeling, we hypothesize that the "bump" feature we observe in the spectra of Orus and Patroclus is due to Rayleigh scattering from fine grained (20-80 nm), opaque particles consistent with iron or carbonaceous compositions. Rayleigh scattering has been invoked to explain the spectral properties of planetary surfaces. The conditions necessary for observing the bluing effect of small particles on the spectra of planetary surfaces was explored in Brown (2014), which found that Rayleigh scattering induced bluing can overtake the effects of absorption for sufficiently small, dark particles. In Clark et al. (2008) and Clark et al. (2012), a Rayleigh scattering peak coupled with an ultraviolet absorber was shown to explain the spectral properties of dark materials on the Saturnian moons Dione and Iapetus. In those papers, the dark material is presumed to be exogenous in origin, and is present either embedded within or as a thin layer on top of the icy surfaces of the satellites. Only a small weight percentage is needed for Rayleigh scattering to affect the spectrum.

However, unlike in our model, the Rayleigh scatterers in the Iapetus and Dione papers are embedded within an ice matrix. In our model, our scattering grains are mixed assuming separate particles averaged in an areal mixture, rather than as small grains embedded in a matrix. We implemented the option to test inclusions of fine grained materials within a silicate matrix using Maxwell-Garnett theory following methods outlined in Fayolle et al. (2021), but found that these models did not provide a good fit to the UV spectral features of interest. One key feature contributing to the shape of the Rayleigh peak in the spectra from Clark et al. (2008, 2012) is the transition between a regime dominated by Rayleigh scattering and a regime dominated by absorption of the iron particles. Due to large amounts of noise at the shortest wavelength end of our spectra, it is difficult for us to say if or where this transition happens for our Trojans, but given the results of Wong et al. (2019) that showed the reddish slopes of the Trojans continue into the UV, we postulate that eventually the Rayleigh feature on the the Trojans could turn over as well, returning to the reddish slope trend at shorter wavelengths in the UV.

In terms of size, the Rayleigh scattering species in our best fit models are referred to in the planetary literature as submicroscopic particles. Submicroscopic particles have been implicated in space weathering on airless bodies including Earth's moon (Pieters et al. (2000)), Mercury (Lucey & Riner (2011)), and asteroids (Britt & Pieters (1994)). However, the particles in our models are significantly larger than the nanophase iron inclusions in lunar agglutinate rims–iron inclusions of this size (>25 nm) that tend to darken spectra without reddening (Lucey & Noble (2008); Noble et al. (2007)). While submicroscopic particles are found throughout the space weathering literature, our Rayleigh scattering particles differ from those studied in the lunar context as they are not modeled as inclusions within a silicate matrix but as separate particles. Our Rayleigh scattering particles also may be different in composition, as our best-fitting models include both amorphous carbon and graphite as potential scattering species, along with the traditional iron. Additionally, studies of space weathering on asteroids focus mainly on C- and S- type asteroids, rather than the D- and P- type asteroids represented by Orus and Patroclus, respectively, so it is unclear how space weathering affects Trojans in particular. Further research is needed to distinguish between iron-based and carbon-based Rayleigh scatterers and understand the role these submicroscopic particles may play in space weathering on the Trojans.

2.5 Conclusions

Using the G280 grism on the Hubble Space Telescope, we measured near-ultraviolet and visible spectra of four Trojan asteroids in order to investigate potential absorption features in the near UV. Absorption features in the near-UV were expected based on previous ground and space-based observations of Trojans (e.g. Wong et al. (2019); Karlsson et al. (2009); Zellner et al. (1985), as well as predicted compositional components of Trojan surfaces invoked to explain their infrared spectral features (e.g. Yang et al. (2013); Wong & Brown (2016)). Though we did not observe the predicted absorption features, we detected a novel spectral feature: an increase in spectral reflectance from 0.35-0.3 μm. This "bump" feature is present in the spectra of both Orus and the Patroclus-Menoetius binary. We developed a modified Hapke model in order to test whether this feature could be due to Rayleigh scattering from fine grained, submicroscopic particles on the surfaces of Trojans, testing two general classes of Rayleigh scatterers: ices (including H_2O, CO_2, and NH_3); and opaques (including iron, graphite, and amorphous carbon). We find that our spectra are consistent with a silicate surface mixed with opaques, including opaque Rayleigh scattering species. Though our results identify the opaque class of scatterers as a potential species responsible for producing the "bump" feature, our model does not distinguish between the individual opaques species (iron, graphites, and amorphous carbon). We find that the feature could be caused by Rayleigh scattering particles ranging in size from 20

- 80 nm. Particles of this size have been implicated as space weathering agents in the literature, acting to darken the spectra of airless bodies (e.g. Lucey & Riner (2011); Lucey & Noble (2008); Pieters et al. (2000); Britt & Pieters (1994)). Whether these particles are the products of space weathering and responsible for the dark surfaces of the Trojan asteroids is beyond the scope of the research presented in this paper, but may be addressed by the upcoming Lucy mission, which will have the capability to measure the photometric properties of Trojan surfaces of different ages (Levison et al. (2021)).

2.6 Acknowledgements

The authors wish to acknowledge Keith Noll for his assistance in preparing the Hubble Space Telescope proposal. We would also like to thank the two anonymous peer reviewers whose comments improved the quality and clarity of the manuscript.

These observations are associated with programs #15259 and #15504. Support for programs #15259 and #15504 was provided by NASA through a grant from the Space Telescope Science Institute, which is operated by the Association of Universities for Research in Astronomy, Inc., under NASA contract NAS5-26555.

These results made use of the Lowell Discovery Telescope (LDT) at Lowell Observatory. Lowell is a private, non-profit institution dedicated to astrophysical research and public appreciation of astronomy and operates the LDT in partnership with Boston University, the University of Maryland, the University of Toledo, Northern Arizona University and Yale University. The upgrade of the DeVeny optical spectrograph has been funded by a generous grant from John and Ginger Giovale and by a grant from the Mt. Cuba Astronomical Foundation.

Chapter 3

Comparative Mid-Infrared Spectroscopy of Dark, Primitive Asteroids: Does Shared Taxonomic Class Indicate Shared Silicate Composition?

This chapter contains work to be published in the Planetary Science Journal. This manuscript is currently undergoing peer review. As such, this chapter is in manuscript form and represents an initial draft of the paper. The table formatting has been changed to comply with University requirements, but the text and figures are unaltered. The final published manuscript will be similar to this version.

Comparative Mid-Infrared Spectroscopy of Dark, Primitive Asteroids: Does Shared Taxonomic Class Indicate Shared Silicate Composition?

Oriel A. Humes[1]; Audrey C. Martin[2]; Cristina A. Thomas[1] ; and Joshua P. Emery[1]

[1] *Northern Arizona University*

Flagstaff, Arizona

86011, USA

[2] *University of Central Florida*

Orlando, Florida

32816, USA

(Received 2023 March 9)

Submitted to PSJ

ABSTRACT

Primitive asteroids with low albedos and red slopes in the visible and near infrared (VNIR) are found in both the Main Belt and the Jupiter Trojan clouds. In order to determine whether the VNIR spectral similarities of primitive Main Belt asteroids and Jupiter Trojans are reflective of a true compositional similarity,

Corresponding author: Oriel A. Humes
oah28@nau.edu

we compare the mid-infrared silicate emission features of Main Belt and Jupiter Trojan asteroids. Using archival data from the Spitzer Space Telescope's IRS spectrograph and observations from the Stratospheric Observatory for Infrared Astronomy's (SOFIA) FORCAST instrument, we analyze the 5-40 μm spectra of thirteen primitive Main Belt asteroids and compare them to those of Jupiter Trojans in the literature. We find that while many primitive asteroids in the Main Belt resemble their Trojan counterparts with strong spectral signatures of olivine-rich high-porosity silicate regoliths, we identify (368) Haidea as a particularly olivine-poor D-type asteroid, indicating a diversity in silicate compositions among primitive asteroids. Differences in silicate compositions among D-type asteroids imply a diversity of origins for primitive asteroids.

Keywords: Asteroids (72); Infrared Spectroscopy (786); Small Solar System Bodies (1469); Silicate Grains (1456)

3.1 Introduction

Small Solar System bodies, including asteroids and comets, are understood as tracers of the evolutionary history of the Solar System. Primitive asteroids—those that have undergone little to no geothermal evolution since their formation—in particular are valuable sources of information about conditions in the early Solar System as their compositions closely reflect the composition of the Solar nebula in which they formed. The present-day compositional distribution of asteroids is thought to reflect of a combination of initial conditions in the protosolar nebula and the subsequent transport of small bodies (DeMeo & Carry (2013)). In general for large (>50 km) asteroids, the abundance of high-melting point materials at low heliocentric distances and abundance of relatively more volatile materials at high heliocentric distances suggests that these compositions reflect thermal and chemical gradients within the early Solar System (Gradie & Tedesco (1982); DeMeo & Carry (2013)). For instance, the presence of hydrated silicates in carbonaceous chondrites, analogs for C-type asteroids common in the Main Belt, suggests a formation region beyond the water frost line but not so far from the Sun that long orbital timescales preclude the accretion of asteroids prior to the decay of short-lived radionuclides that provide the heat source necessary for thermal alteration to occur (Grimm & McSween Jr (1989)). Thus, the locations of primitive C-type asteroids can indicate the availability of water within the solar nebula (e.g. Ceres in McCord & Sotin (2005)). On the other hand, the diversity of all asteroid types at small scales throughout the Main Belt (DeMeo et al. (2014); DeMeo & Carry (2013)) provides evidence for substantial migration and mixing among small bodies after their formation. Both initial compositional gradients and subsequent mixing of asteroid materials are necessary to explain the distribution of asteroids we see today.

The D- & P-type asteroids, characterized by their low albedos and red sloped, featureless spectra (Tholen (1984); Tholen & Barucci (1989); DeMeo et al. (2009)) in the visible and near infrared (VNIR), are a particularly intriguing population of primitive asteroids. Dynamical modeling has led to the suggestion that Trojan (Morbidelli et al. (2005)) and Main Belt (Levison et al. (2021)) D- and P-types originated from the relatively cooler outer regions of the protoplanetary disk. Their increasing frequency at larger heliocentric distances (Tholen & Barucci (1989); DeMeo & Carry (2013)) and spectral resemblance to some outer Solar System populations including Centaurs and trans-Neptunian Objects (Sheppard (2010)) supports this idea. As primitive asteroids, the D- & P-types preserve much of their original compositions, thus by understanding their compositions we gain unique insights into conditions in the early Solar System, and by understanding their distribution in location we can provide constraints on dynamical models of the early Solar System. Previous spectral modeling studies of D- & P-types in the VNIR (Emery & Brown (2004); Sharkey et al. (2019); Gartrelle et al. (2021a)) have proposed compositions rich in silicates with trace amounts of organics and ices, suggestive of an outer Solar System origin. However, the lack of VNIR spectral features limits our ability to infer the compositions of these asteroids. Understanding the origin of primitive asteroids is a priority for a number of recent and upcoming spacecraft missions including the Lucy (Levison et al. (2021)) mission.

The Jupiter Trojan population is a major reservoir for D- & P-type asteroids, which comprise the majority of asteroids in the Jovian Trojan swarms (Emery et al. (2010); DeMeo & Carry (2013)). The Jupiter Trojans orbit in proximity to the Sun-Jupiter L4 and L5 Lagrange points, and because of their unique orbital relationship to Jupiter, many dynamical hypotheses have been proposed to explain their emplacement within the Lagrange points (e.g. Morbidelli et al. (2005); Nesvorný et al. (2013); Pirani et al. (2019)). These models demonstrate that the properties of the Trojans we observe today depend both on where the Trojans initially formed and the subsequent migration history of the giant planets that led to their emplacement within Jupiter's Lagrange regions. For instance, the Nice model (Morbidelli et al. (2005)) predicts a primarily outer Solar System origin for Trojans, while the Jumping Jupiter (Nesvorný et al. (2013)) model predicts that the Trojans sample regions including both the inner and outer Solar System. Probing the relationship between D- & P-types in the Main Belt and Trojan swarms can provide an observational test for these models of giant planet migration. For example, the Nice model predicts a common, specifically outer Solar System, parent population for D- & P-types across the Main Belt, Hilda, and Trojan populations (Levison et al. (2009)).

In contrast to the relatively featureless VNIR, in the mid-infrared, many D- & P-type asteroids exhibit 10- and 20-μm silicate emission features (Emery et al. (2006); Mueller et al. (2010); Licandro et al. (2011)). These features are diagnostic of both physical and chemical properties of silicates, including regolith porosity (Martin et al. (2022); Martin (2022)), Mg# (the ratio of magnesium to iron in a mineral lattice) for both

Table 3.1. Physical and orbital properties of primitive asteroids examined in this paper

Asteroid	Semimajor Axis (AU)	Eccentricity	Inclination (deg)	H (mag.)	Taxonomic Classification
46 Hestia	2.52	0.17	2.35	8.59	P/Xc
65 Cybele	3.44	0.12	3.56	6.89	P/Xc
87 Sylvia	3.48	0.09	10.9	6.98	P/X
140 Siwa	2.73	0.21	3.19	8.5	P/Xc
190 Ismene	3.99	0.17	6.18	7.7	P/X
267 Tirza	2.78	0.10	6.01	10.3	DU/D
269 Justitia	2.62	0.21	5.48	9.79	Ld/IR-RR
336 Lacadiera	2.25	0.10	5.65	9.86	D/Xk
368 Haidea	3.07	0.20	7.8	10	D/
944 Hidalgo	5.73	0.66	42.6	10.56	D/
1268 Libya	3.98	0.10	4.43	9.12	P/
1702 Kalahari	2.86	0.14	9.96	11.1	D/L
3552 Don Quixote	4.26	0.71	31.1	13.07	D/D

Note. — Taxinomic classifications are given as (Tholen/SMASSII) classifications from Neese (2017), except in the cases of Justitia, which has been classified using Tholen and the TNO classification scheme from Hasegawa et al. (2021) and Don Quixote, which uses the Tholen/SMASSII classification and comes from from Binzel et al. (2004). Note that the IR-RR classification for Justitia indicates that it is redder than the typical D type.

pyroxenes (Hamilton (2000); Chihara et al. (2002)) and olivines (Koike et al. (2003); Hamilton (2010); Lane et al. (2011)), amorphous vs crystalline mineral structure (Martin (2022)), and silicate hydration state (Beck et al. (2014); McAdam et al. (2015). The compositional properties as revealed by silicate emission features in the mid-infrared ($\sim$ 5-40 μm) are indicative of formation region, as temperature conditions within the initial solar nebula influence the materials and formation pathways available to condense silicates at varying heliocentric distances (Gail (2004); Henning (2010); Morlok et al. (2014)). In Martin (2022) the silicate emissivity spectrum was characterized in detail to determine composition and regolith porosity of several Jupiter Trojans. That study concluded that Jupiter Trojans likely originate from the outer Solar System due to the abundance of magnesium-rich silicates, absence of hydrated silicates, and high porosity regoliths similar to those of comets.

In this paper we present the spectra of thirteen D- & P-type asteroids as observed by the Stratospheric Observatory for Infrared Astronomy (SOFIA) and Spitzer Space Telescope (see Table 3.1). This group samples objects in the Main Belt, Cybele, and near-Earth populations, but not the Trojans previously characterized in Martin (2022). We examine silicate emission features in the mid-infrared to compare the spectra of Main Belt D- & P-types and literature spectra of Jupiter Trojan D- & P-types (Martin (2022);

Emery et al. (2006)) to determine whether these two populations, which are similar in the VNIR, resemble each other in the mid-infrared. Similarities in silicate compositions among these two populations would point to a shared region of origin for primitive asteroids across the Trojan and Main Belt populations, while compositional differences would indicate separate parent populations for primitive Main Belt and Trojan asteroids. Determining whether primitive asteroids in the Main Belt share the outer Solar System origin suggested by Martin (2022) for the Trojans will allow us to determine the extent of mixing between inner and outer Solar System materials within the Main Belt and provide new observational constraints on formation and emplacement mechanisms for primitive asteroids. Constraining the amount of outer Solar System material that has been delivered to the Main Belt and inner Solar System subsequently will lead to a greater understanding of the mechanisms responsible for delivering volatiles from beyond the frost line to the inner Solar System.

3.2 Methods

3.2.1 Spitzer Space Telescope Observations

We identified eleven non-Trojan D- & P-type asteroids in the Spitzer Heritage archive. These asteroids were observed using the Infrared Spectrograph (IRS) instrument (Houck et al. (2004)) by programs IRS_P/666, IRS_R/668, ASTEROIDS-1/88, and ASTEROIDS-2/91. These targets included observations in all four IRS modes: short-low (SL, 5.2-14.5 μm), long-low (LL, 14.0-38.0 μm), short-high (SH, 9.9-19.6 μm), and long-high (LH, 18.7-37.2μm). Observations in any one of these modes are useful for identifying silicate emission features, as the SL and SH modes cover the 10 μm region and the LL and LH modes cover the 20 μm region, and the choice of observing mode was influenced by the brightness of individual targets. For observations in the low resolution modes (SL and LL), background pair subtraction was performed by pairing images in two different nod positions. In some cases (e.g. Siwa), the two nod positions resulted in the spectral trace falling on two different regions of the same section of the chip, while most asteroids had spectra that nodded between the two different sections of the chip (i.e. orders 1 & 2 vs. order 3). For observations in the high resolution modes (SH and LH), background subtraction was done by subtracting the average of "shadow" observations taken of empty sky at the observed location of the asteroid after some time had passed and the asteroid had moved. While SH and LH spectra were available for Siwa and Lacadiera in these modes, the lack of corresponding "shadow" observations prevented these additional spectra from being extracted since they lacked an appropriate measurement of background.

Table 3.2. Observation circumstances for D- & P-type asteroids in the Spitzer Heritage Archive

Asteroid	Modes	Program	Obs. Time UTC	Exp. Time (sec)	r AU	Δ AU	Phase Angle deg
65 Cybele	Spitzer SH	ASTEROIDS-2/91	2005-Feb-08 6:05	12	3.79	3.30	14.1
	Spitzer SL	ASTEROIDS-2/91	2005-Feb-08 6:00	43	3.79	3.3	14.1
87 Sylvia	Spitzer SH, LH	ASTEROIDS-1/88	2004-Nov-12 6:40	12, 13	3.22	2.71	17.1
	Spizter SL	ASTEROIDS-1/88	2004-Nov-12 5:47	26	3.22	2.71	17.1
140 Siwa	Spitzer SL	ASTEROIDS-2/91	2004-Feb-29 9:01	14	2.65	2.23	21.4
267 Tirza	Spitzer SL, LL	ASTEROIDS-2/91	2005-Nov-17 1:40	135, 25	3.02	2.97	19.6
269 Justitia	Spitzer SL	ASTEROIDS-2/91	2005-Apr-15 7:54	25	2.12	1.66	27.5
336 Lacadiera	Spitzer SL	ASTEROIDS-2/91	2004-Oct-03 17:29	24	2.43	1.96	24.0
368 Haidea	Spitzer SL, LL	ASTEROIDS-1/88	2004-Mar-25 23:29	46, 25	3.69	3.15	14.1
944 Hidalgo	Spitzer SL, LL	ASTEROIDS-2/91	2006-Jul-24 10:18	53, 25	1.96	1.71	30.7
1268 Libya	Spitzer SL, LL	IRS_R/666	2003-Nov-16 10:32	609, 148	4.19	4.00	13.9
1702 Kalahari	Spitzer SL, LL	ASTEROIDS-2/91	2005-Jul-03 4:42	513, 58	3.09	2.67	18.6
3552 Don Quixote	Spitzer LL	ASTEROIDS-1/88	2004-Mar-23 4:43	4696	6.91	6.49	7.76

Note. — For each asteroid, we report the modes used to observe the asteroid, the associated observing program, the mean observation time, total exposure time for each mode, as well as the observational geometries including heliocentric distance r, distance from the asteroid to the telescope Δ, and the phase angle as calculated by the JPL Horizons online ephemeris.

After background subtraction, the spectra were extracted using the Spitzer IRS Custom Extraction software (SPICE), following the general procedure outlined in Recipe 16 of the Spitzer Data Analysis Cookbook (Spitzer Science User Support and Instrument Teams and IRSA Science User Support Team (2017)). Next, the extracted spectra were adjusted so that each order was scaled to the same flux value in regions where the orders overlapped. This was accomplished by fitting low (first, second, or third) order polynomials to the data, then determining the resulting multiplicative scaling factor necessary such that the polynomials would have the same value–that is the mean of the predicted fluxes–at a specific wavelength. For some data, obvious outliers due to instrumental effects (e.g. the SL teardrop at long wavelengths) were excluded from the fit to ensure better alignment of the orders. For the SL and LL observations, the alignment wavelengths were 7.5 and 21 μm respectively, that is, each spectrum was scaled to the average predicted flux measurement of all orders at 7.5 or 21 μm. For asteroids with both SL and LL observations, we aligned the two modes to the average predicted flux at 15 μm. For the SH and LH observations, no single wavelength region overlaps in all spectral orders, so predicted fluxes and scale factors required to align the spectral orders were calculated at wavelengths of 10.5, 11, 11.65, 12.4, 13.1, 14.3, 15.1, 16.4, and 17.8 μm for the SH and 20.5, 21, 22.5, 24, 25.5, 27, 29, 31.25, and 34 μm for the LH data, then scaled by the average of the all scale factors calculated for each mode. This has the effect of weighting each region of overlap equally.

For most asteroids, only two spectra were taken, but for some especially bright targets (e.g. the SL observations of Cybele, Sylvia, Justitia, Lacadiera, Hidalgo, Libya, Tirza, and Siwa), IRS was used in mapping mode to ensure the target was well centered in the slit. Rather than using the peak-up cameras to locate the centroid of the target, which saturated for bright targets, observations were taken by stepping across the disk of the asteroid to ensure at least one pair of observations were well centered in the slit. In these instances, only the brightest pair of extracted spectra were used in the rest of the analysis to exclude observations that were not well-centered in the slit. While LH observations of Cybele and corresponding shadow observations exist in the Spitzer Heritage Archive, the fluxes at the long wavelength end of the SH data did not match the fluxes at the short wavelength end of the LH data at 19 μm, indicating that in the LH data the asteroid was not well centered in the slit. Therefore, we exclude the LH data for Cybele in our analysis. A summary of the Spitzer observations and their observing circumstances can be found in Table 3.2.

We note that the Spitzer IRS spectra of several asteroids already exist in the published literature. In particular, Spitzer IRS spectra of 65 Cybele (Licandro et al. (2011)), 87 Sylvia (Marchis et al. (2012)), 386 Haidea (Vernazza et al. (2013)), and 3552 Don Quixote (Mommert et al. (2014)) have been examined by previous authors. In these cases we re-reduced the data starting from the Level 2 data products available in

the Spitzer Heritage Archive in ensure consistency between all asteroids in our dataset in the reduction and thermal modeling process.

3.2.2 Stratospheric Observatory For Infrared Astronomy (SOFIA) Observations

In addition to the Spitzer observations described above, we also observed four primitive asteroids using the Stratospheric Observatory For Infrared Astronomy (SOFIA). We observed these asteroids using the Faint Object infraRed Camera for the SOFIA Telescope (FORCAST) instrument (Herter et al. (2018)) as part of program 08_0105. Each asteroid was observed using the G111 and G227 grisms along with contemporaneous imagery in the F111 and F253 filters. Initial processing of these images, including background subtraction and spectral extraction were performed by the Universities Space Research Association (USRA) and the extracted spectra and background-subtracted images were downloaded directly from the Infrared Science Archive (IRSA). We located the centroid of each asteroid in the F111 and F253 images then performed background-subtracted aperture photometry using an object radius of 12 pixels and an background annulus with inner and outer radii of 15 and 25 pixels, respectively, according to the procedure described in the *FORCAST Basic Photometry cookbook* (SOFIA/USRA (2022a)). We then used the photometric measurements to align the G111 and G227 spectra for each asteroid. By convolving the object spectra and the transmission spectra of the F111 and F253 filters (SOFIA/USRA (2022b)), we computed the predicted F111 and F253 photometric fluxes. Using the ratio between the predicted and actual fluxes, we calculated the multiplicative factor needed to bring the grism spectra into alignment with the measured photometry such that the predicted convolved fluxes were equal to the measured photometry. While this procedure generally follows the procedure outlined in the *FORCAST Grism Spectra: Basic Inspection and Assessment* notebook in SOFIA/USRA (2022b) we used a multiplicative (rather than additive) correcting factor to align our spectra to the photometry. Our rationale is that in order to convert from flux to emissivity, we must divide by a model of the black body emission of the asteroid. An additive correction factor would then distort the shape of the resulting emissivity spectrum, while a multiplicative factor would maintain its shape. Using a multiplicative factor also parallels the process of aligning the spectral orders of the Spitzer data as described above.

Table 3.3. Observation circumstances for primitive asteroids using SOFIA

Asteroid	Filters/Grisms	Exposure Times (sec)	Obs.Time UTC	r AU	Δ AU	Phase Angle deg
46 Hestia	G227	544	2021-Jun-30 5:32	2.63	1.87	17.5
	G111, G227, F111, F253	838, 454, 46.4, 36.2	2021-Jul-09 5:14	2.62	1.95	19.6
87 Sylvia	G111, G227, F111, F253	1280, 699, 67.1, 55.8	2022-May-24 6:47	3.55	2.58	5.37
140 Siwa	G111, G227, F111, F253	935, 349, 70.3, 53.7	2022-May-27 5:36	2.51	1.61	13.1
190 Ismene	G227, F253	1360, 44.6	2022-Feb-02 8:33	3.41	2.46	5.17
	G111, F111	2350, 70.9	2022-Feb-09 9:14	3.41	2.5	7.23

Note. — For each asteroid, we report the filters used to observe the asteroid, the mean observation time, total exposure time for each filter, and the observational geometries including heliocentric distance r, distance from the asteroid to the telescope Δ, and the phase angle as calculated by the JPL Horizons online ephemeris.

3.2.3 Thermal Modeling

Both the Spitzer Space Telescope and SOFIA observe the thermal emission from asteroids in Jansky. In order to convert from a thermal emission spectrum to an emissivity spectrum, we must model the predicted thermal emission for each asteroid, then divide the emission data by this predicted emission spectrum to obtain an emissivity spectrum (Harris (1998)). The Near Earth Asteroid Thermal Model (NEATM), while initially developed to model thermal emission of near-Earth asteroids, is commonly used to predict thermal fluxes for Main Belt and Trojan asteroids throughout the literature (e.g. Emery et al. (2006); Hargrove et al. (2012); Licandro et al. (2011)). By equating incoming solar energy (a factor of the geometric albedo a) and outgoing thermal emission, this model computes the thermal emission due to solar heating at each point on the sunlit hemisphere of an asteroid (the contribution from the unlit hemisphere is assumed to be 0). Then, using the geometric circumstances of the observation, the flux received by the observer is computed by integrating the predicted emission over the hemisphere visible to the observer (Harris (1998)). In addition to the geometric factors, the NEATM we used also includes two empirical corrections: a beaming parameter η to correct for surface roughness and a mean emissivity ϵ.

For our observations, we used the NEATM included in the `mskpy surfaces` package developed for python by Michael Kelley (Kelley (2021)). This model uses χ^2 minimization to derive the best fit diameter and mean emissivity given observing geometry, albedo, and the beaming parameter and computes the corresponding modeled fluxes at a given wavelength. We assumed a beaming parameter of $\eta = 0.96$, the mean beaming parameter for asteroids as reported in Mainzer et al. (2011). To convert from flux to emissivity, we divided the fluxes as measured by the telescope by the modeled flux, then multiplied by the mean emissivity value output by the χ^2 minimization routine. For most asteroids, we used a single NEATM to model the flux, that is to say that both short wavelength spectra (e.g. from Sptizer SL or SOFIA G111) and long wavelength spectra (e.g. from Spitzer LL or SOFIA G227) were combined into a single spectrum that was used as input into the thermal model if the observations were taken on the same day. For 368 Haidea and 1702 Kalahari, we found that the long wavelength end of the Spitzer SL spectrum was heavily affected by the SL teardrop, a noted artifact affecting this region of Spitzer spectra. The artifact led to difficulty in aligning the SL and LL spectra. For these two asteroids, we fit a separate NEATM for the SL and LL segments.

Table 3.4. Results of Thermal Modeling

Asteroid	Instrument and Mode(s)	Literature Albedo	Literature Diameter (km)	Derived Diameter (km)	Derived Mean Emissivity
46 Hestia	SOFIA G227*	0.046	131	90.5	0.47
	SOFIA G111, G227	0.046	131	131	0.96
65 Cybele	Spitzer SH	0.071	237	290	0.97
	Spitzer SL	0.071	237	292	0.93
87 Sylvia	Spitzer SH, LH	0.046	253	246	0.96
	Spizter SL	0.046	253	263	0.98
	SOFIA G111, G227	0.046	253	267	0.89
140 Siwa	Spitzer SL	0.068	110	92.6	0.87
	SOFIA G111, G227	0.068	110	98.4	0.76
190 Ismene	SOFIA G227	0.066	159	179	0.84
	SOFIA G111	0.066	159	174	0.75
267 Tirza	Spitzer SL, LL	0.051	5.6	64.7	0.40
269 Justitia	Spitzer SL	0.061	50.7	50.4	0.84
336 Lacadiera	Spitzer SL	0.054	63.4	69.9	0.99
368 Haidea	Spitzer SL	0.038	69.3	66.7	0.88
	Spitzer LL	0.038	69.3	67.1	0.84
944 Hidalgo	Spitzer SL, LL	0.060	38.0	45.6	0.77
1268 Libya	Spitzer SL	0.043	96.7	101	0.91
	Spitzer LL	0.043	96.7	95.8	0.91
1702 Kalahari	Spitzer SL	0.065	34.6	34.7	0.85
	Sptizer LL	0.065	34.6	33.7	0.75
3552 Don Quixote	Spitzer LL	0.030	19.0	18.7	0.76

Note. — For each asteroid, literature values for diameter and albedo were taken from JPL Horizons based on IRAS (Tedesco et al. (2004)) and NEOWISE (Mainzer et al. (2019)) measurements. Note that a lack of contemporaneous photometry for the June G227 observations of 46 Hestia (starred) resulted in a fit with an asteroid diameter that does not agree with literature values, as these observations could not be scaled to account for potential slit losses.

3.3 Results

3.3.1 Emissivity Spectra and Thermal Modeling

The results of the NEATM modeling are summarized in Table 3.4. We note good agreement between the reported literature values and NEATM derived diameters, with the notable exception of the June SOFIA G227 observations of 46 Hestia. These observations were taken without contemporaneous photometry, so these spectra could not be scaled to account for potential slit losses. Accordingly, the NEATM derived diameter and mean emissivity is lower for this observation than for the other observation of 46 Hestia. For this observation in particular, the June SOFIA G227 observations were converted to emissivity by dividing by the thermal model, then multiplying the resulting emissivity spectrum by a scaling factor to align the June G227 observations that lacked photometry to the July G227 observations. These two G227 observations were averaged together to produce the final G227 spectrum of 46 Hestia, so the June values of mean emissivity and diameter are likely a reflection of observation circumstances (e.g. slit misalignment) rather than reflective of a true physical property of 46 Hestia.

3.3.2 Feature Characterization

We present the complete SOFIA spectra (8-14 μm & 18-28 μm) in Figure 3.1 and the Spitzer Space Telescope spectra (5 - 40 μm) in Figures 3.2 and 3.3. In general, the Spitzer spectra tend to show a sharp emissivity dip at short wavelengths, followed by the broad 10-μm silicate feature in emission. At longer wavelengths, the spectra tend to show additional silicate features around 15 and 20 μm followed by a flat or linear continuum. To describe the general shapes of the features we employ the terminology used in Kelley et al. (2017) to compare the mid-infrared spectra of comets and Jupiter Trojans: the broad 10-μm features are characterized as trapezoidal, rounded, or present.

Among our sample, we see trapezoidal 10-μm features in the spectra of 65 Cybele, 87 Sylvia, 267 Tirza, and 944 Hidalgo. These asteroids all show sharp shoulders (e.g. a change in slope from the relatively flat slope of the 10-μm plateau to a decreasing slope) near 11 μm, bounding the long wavelength edge of the emission features.

We see rounded 10-μm features in the spectra of 269 Justitia, 336 Lacadiera, 1268 Libya, and 1702 Kalahari. These asteroids show 10-μm features bounded by dips at 8 and 12 μm like the trapezoidal asteroids, but the shoulder at 11 μm is less distinct but still present. 386 Haidea also has a rounded 10-μm feature, but unlike the previous examples, 386 Haidea lacks a peak or shoulder near 11 μm. Instead, the spectrum of 386 Haidea begins to turn downwards at 10.55 μm.

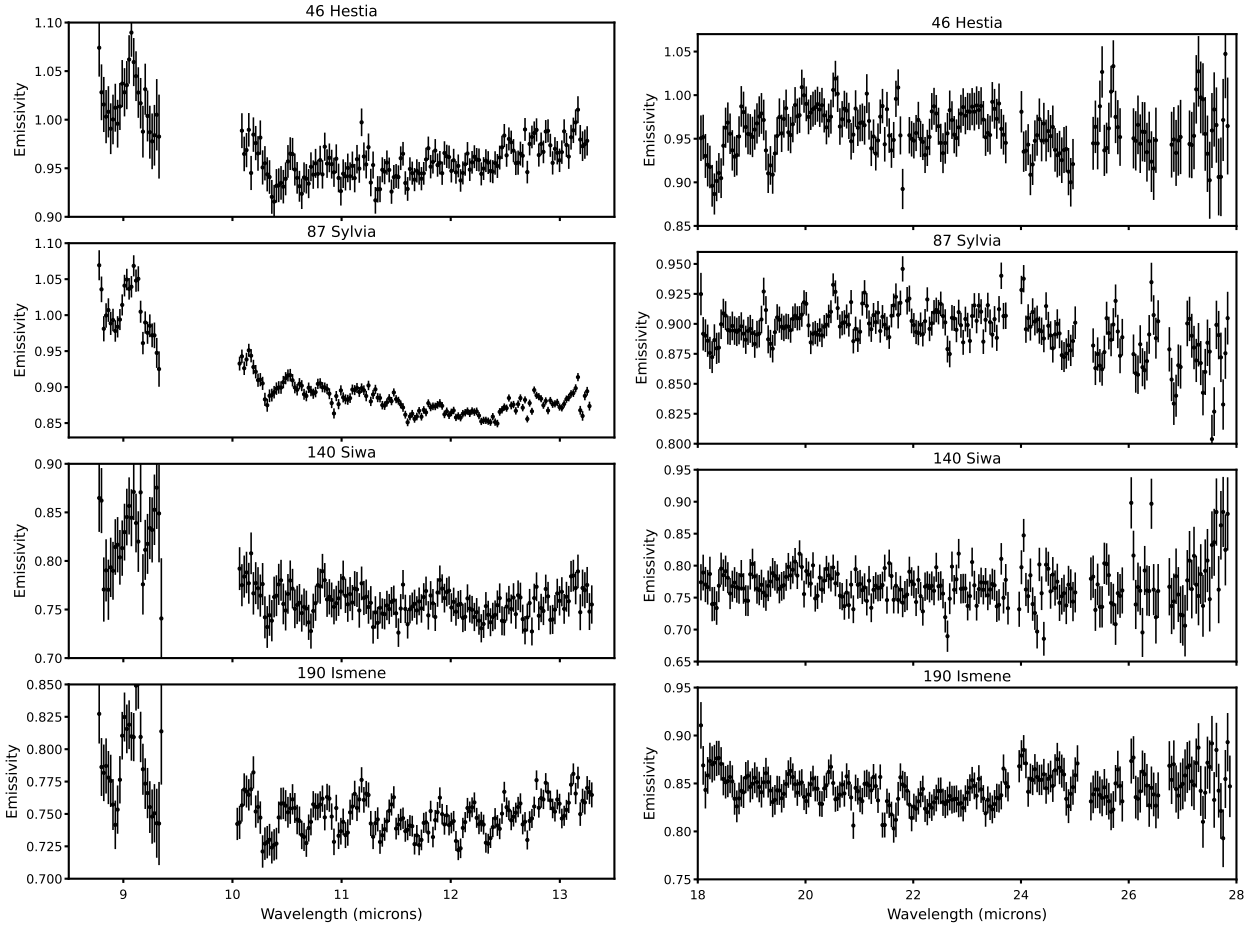

Figure 3.1 Mid-infrared spectra of asteroids (46) Hestia, (87) Sylvia, (140) Siwa, and (190) Ismene as observed by the SOFIA FORCAST instrument, using the G111 (panel a) and G227 (panel b) grisms. Note that we do not display data points for which atmospheric transparency is low (< 0.9).

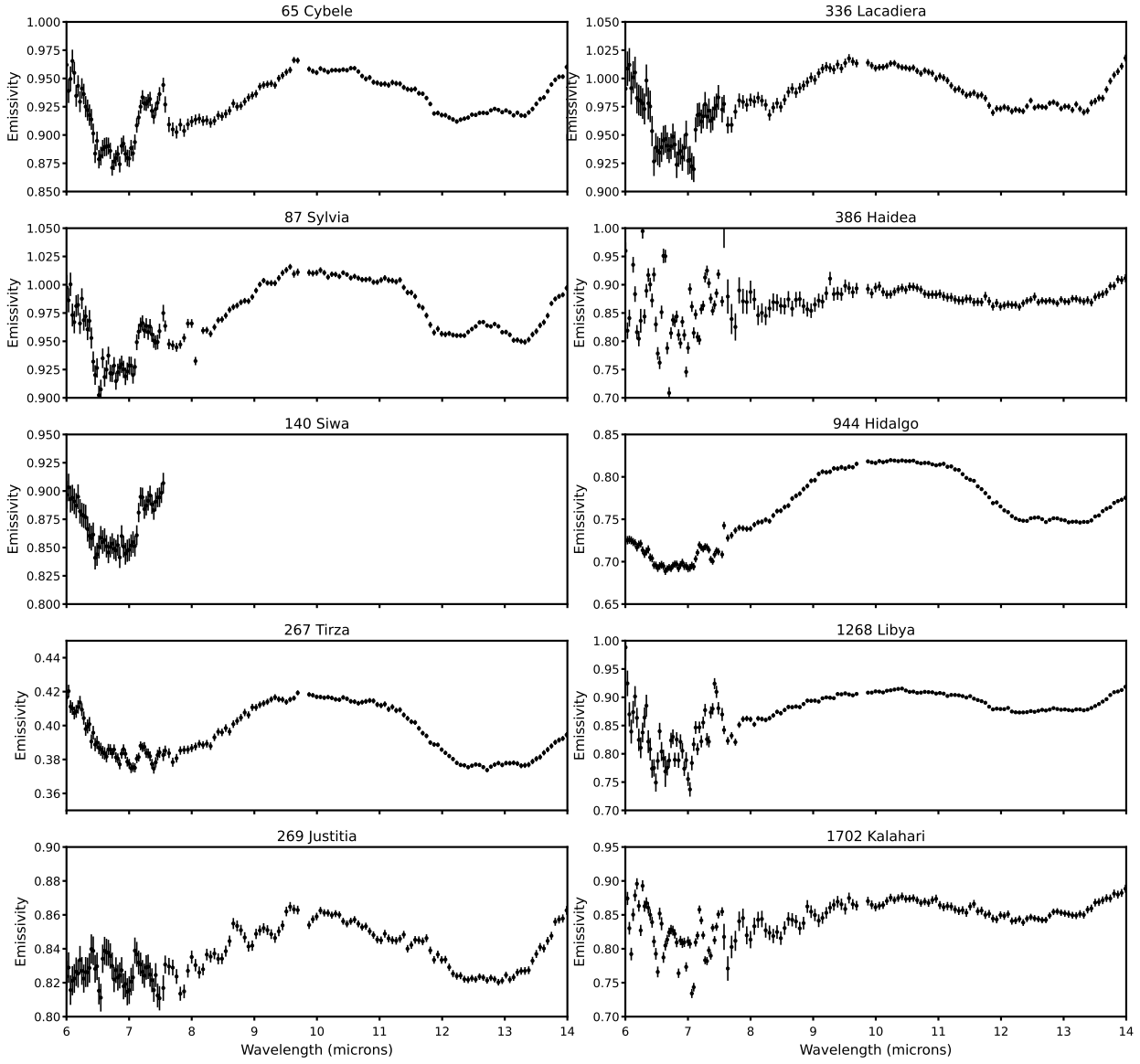

Figure 3.2 Mid-infrared spectra of asteroids (65) Cybele, (87) Sylvia, (140) Siwa, (267) Tirza, (269) Justitia, (336) Lacadiera, (386) Haidea, (944) Hidalgo, (1268) Libya, and (1702) Kalahari from 6-14 μm as observed by the Spitzer IRS instrument in SL mode.

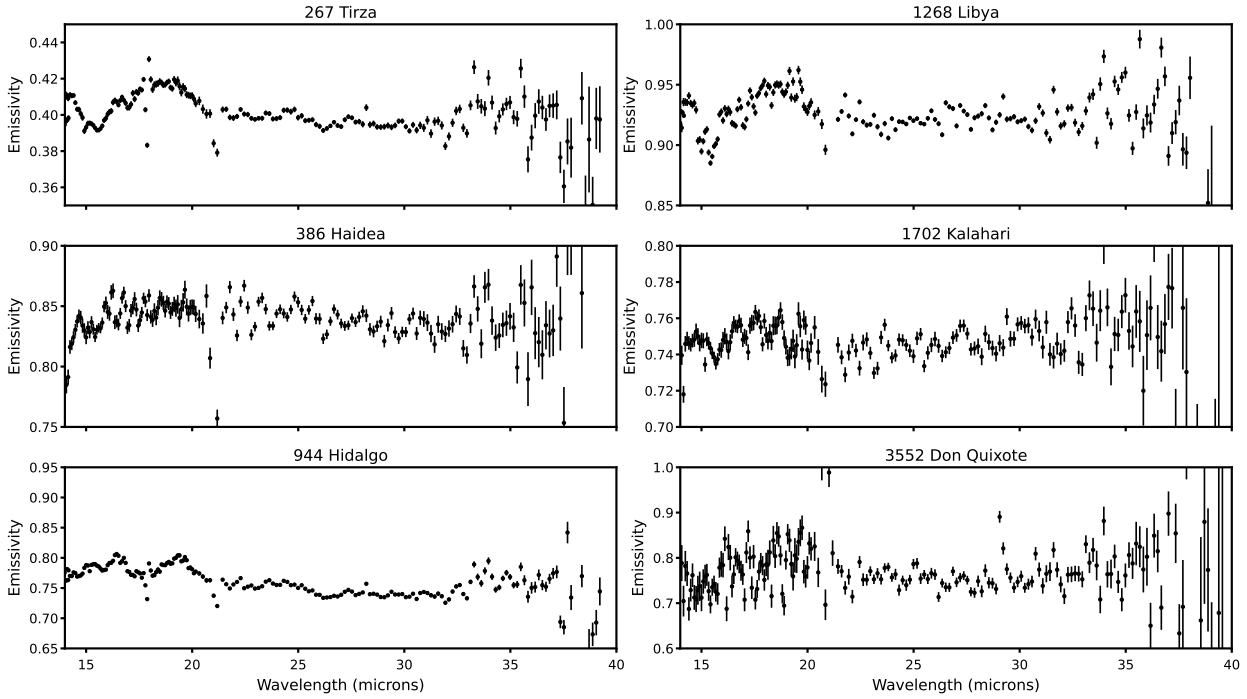

Figure 3.3 Mid-infrared spectra of asteroids (267) Tirza, (386) Haidea, (944) Hidalgo, (1268) Libya, (1702) Kalahari, and (3552) Don Quixote from 14-40 μm as observed by the Spitzer IRS instrument in LL mode.

Without complete coverage of the short wavelength end of the 10 μm feature, it is harder to classify the shapes of the 10-μm feature in the SOFIA data. However, the spectra of 87 Sylvia is consistent across the SOFIA and Spitzer spectra, and the general decrease in emissivity from 10 μm to 12.5 μm is evidence of the 10-μm silicate emission feature in the SOFIA spectrum of 87 Sylvia. Similarly, the higher average emissivities from 10 to 11 μm and presence of the 12.5 μm dip in the SOFIA spectra of both 87 Sylvia and 140 Siwa (which is associated with and defines the long wavelength edge of the 10 μm feature) suggests that the 10 μm feature is present in the spectra of both these asteroids. For 190 Ismene, interpretation of spectral features is complicated by the presence of a systematic, high frequency 'wiggle' in wavelength space present in the G111 spectrum (8 - 14 μm), which shows a series regular peaks separated by ~ 0.34 μm across the short-wavelength portion of the spectrum. For 46 Hestia, we see an increase in emissivity from 10 to 12.5 μm and absence of a clear high wavelength bound on the 10 μm feature suggesting that the 10 μm feature is not present in emission at all.

To determine the precise locations of spectral features in each asteroid spectrum (See Tables 3.5a and 3.5b), we used a Monte Carlo estimation method. For each asteroid in our sample, we generated 1000 synthetic asteroid spectra by drawing emissivity values from a Gaussian distribution centered around the emissivity value of each data point with a standard deviation equal to the error for that point. Then, for each

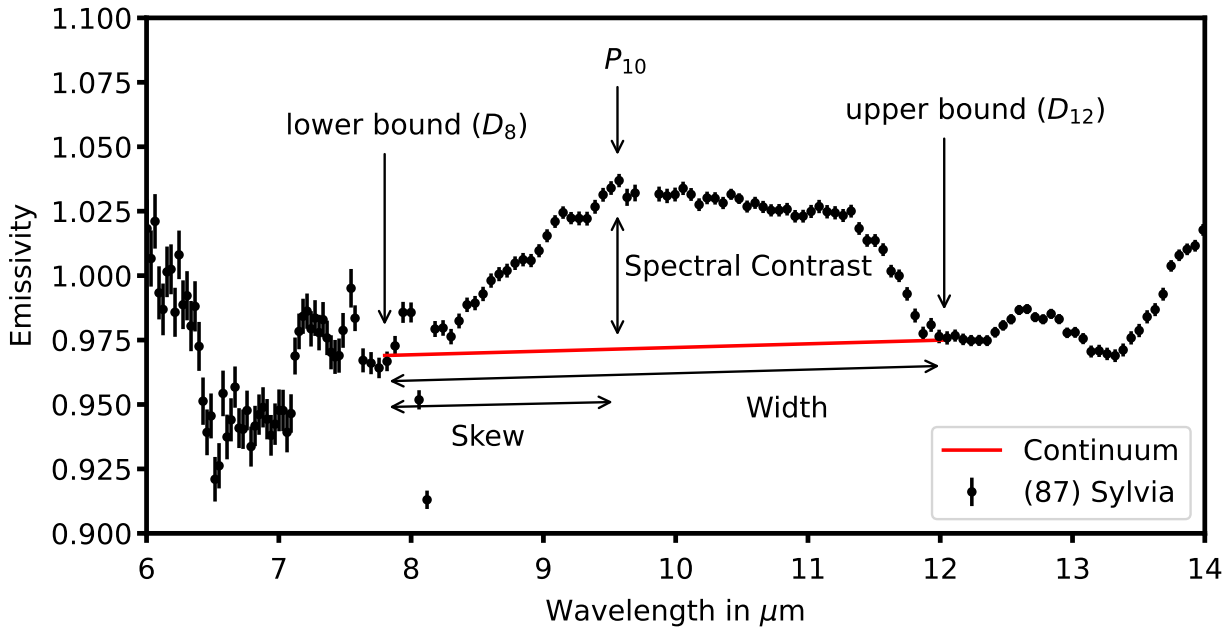

Figure 3.4 Graphical explanation of the band parameters of the 10-μm feature, with the spectrum of (87) Sylvia, normalized to an average emissivity of 1, as an example. Band parameters are measured as described in Martin (2022), except for skew (see text).

synthetic spectrum, we fit a fourth-order polynomial spline to smooth the data, resulting in 1000 smoothed splines for each spectrum. Using a polynomial spline allows local extrema the spectrum to be efficiently identified as the derivatives of polynomials are straightforward to compute. To identify a particular local maximum (minimum), we first identify a range over which to determine the maximum (minimum) visually, then calculate the local extrema for each spline by determining where its derivative is 0. In the case where there are multiple points with a derivative of 0, we evaluate the spline at each point and take the wavelength corresponding to the maximum (minimum) value as the location of the local maximum (minimum). Given the locations of the spline maxima (minima) in wavelength space, we then fit a Gaussian to these measurements to get an average feature position (corresponding to the mean) and error (corresponding to the standard deviation) of the distribution of measurements. Repeating this process for different local extrema allows us to measure the position of various features in the spectrum. This procedure is similar to the feature measurement process described in Martin (2022).

In addition to measuring the locations of various features, we also use the methods described in Martin (2022) to characterize the shape of the 10-μm silicate emission feature to enable direct comparison of the spectral features of our Main Belt sample to the Trojans (See Figure 3.4). In Martin (2022), local minima near 8 and 12 μm are used to define the bounds of the silicate emission feature. In particular, the minimum

at 8 μm is bounded on the lower wavelength side by a sharp dip in emissivity which identifies the edge of the feature. For two asteroids (368 Haidea and 1702 Kalahari) in our sample, we identify the feature edge closer to 7 μm than 8 μm because of the location of this sharp dip. Once the bounds are identified using the procedure described previously to locate local extrema, the mean location of the 8- and 12-μm features are used to define endpoints for a linear continuum, which can be subtracted from the spectrum to isolate the spectrum of the 10-μm feature itself. We parameterize the feature by its width, continuum slope, spectral contrast, and skew (see Table 3.6) as follows:

- Width is measured by subtracting the locations of the 12- and 8-μm bounds.
- Continuum slope is given by the slope of the linear continuum passing between the 12- and 8-μm bounds.
- To obtain spectral contrast, we normalize the spectrum to a mean emissivity of 1, then determine the location of the continuum removed peak near 9.8 μm. Subtracting the emissivity at this peak by the predicted emissivity from the continuum gives a difference in emissivity that can be multiplied by 100 to give a percentage increase in emissivity
- We measure skew as a proportion, dividing the distance from the 9.8-μm peak to the 8-μm bound by the width of the feature. A left-skewing feature has a skew < 0.5, indicating that the continuum-removed peak falls before the midpoint of the bounds, whereas a right-skewing feature has a skew > 0.5, indicating that the continuum-removed peak falls after the midpoint of the bounds. Note that this method for measuring skew matches the one described for measuring the skew of laboratory spectra in Martin (2022) but is different from the one that paper uses to measure the skew of asteroid spectra.

All the asteroids we examine are skewed towards shorter wavelengths, that is, they have skews < 0.5. We also note that for many of the asteroids in our sample, the continuum slopes are flat: this is in contrast with the Trojans in Martin (2022), which in general have positive slopes (e.g. increasing emissivity with increasing wavelength). 944 Hidalgo, 1268 Libya, and 1702 Kalahari are exceptions to this general trend: these asteroids all have positive continuum slopes significant at the 1-σ level. We do not see any asteroids with statistically significant negative continuum slopes. In terms of spectral contrast, the contrasts we calculate are comparable to those seen in the Trojans (Licandro et al. (2011); Martin (2022)).

Table 3.5a. Location of Common Spectral Features

Asteroid	$D_{5.5}$ (μm)	P_6 (μm)	D_7 (μm)	$P_{7.5}$ (μm)	D_8 (μm)	P_9/S_9 (μm)	P_{10} (μm)
46 Hestia	-	-	-	-	-	9.06 ± 0.01*	-
65 Cybele	5.68 ± 0.09	5.97 ± 0.01	6.88 ± 0.06	7.38 ± 0.10	7.90 ± 0.10	X	9.73 ± 0.05
87 Sylvia	5.77 ± 0.06	6.04 ± 0.06	6.62 ± 0.16	7.54 ± 0.06	7.80 ± 0.04	9.15 ± 0.05	9.56 ± 0.02
140 Siwa	5.73 ± 0.02	5.95 ± 0.01	6.77 ± 0.17	7.46 ± 0.07	X*	9.14 ± 0.24*	X*
190 Ismene	-	-	-	-	-	9.12 ± 0.02*	-
267 Tirza	5.72 ± 0.04	6.03 ± 0.01	7.05 ± 0.02	X	7.70 ± 0.03	9.34 ± 0.05	9.77 ± 0.04
269 Justitia	5.78 ± 0.03	6.72 ± 0.08	7.00 ± 0.05	X	7.85 ± 0.02	X	9.66 ± 0.13
336 Lacadiera	5.65 ± 0.12	5.95 ± 0.07	6.60 ± 0.12	7.51 ± 0.09	7.63 ± 0.08	9.14 ± 0.10	9.77 ± 0.06
368 Haidea	X	X	6.69 ± 0.01	7.59 ± 0.08	8.18 ± 0.05	9.26 ± 0.02	10.55 ± 0.08
944 Hidalgo	5.66 ± 0.04	5.93 ± 0.04	6.52 ± 0.05	7.20 ± 0.04	7.41 ± 0.06	9.20 ± 0.04	9.85 ± 0.19
1268 Libya	X	X	6.82 ± 0.19	7.43 ± 0.01	7.74 ± 0.03	X	10.3 ± 0.14
1702 Kalahari	X	X	7.07 ± 0.01	7.52 ± 0.05	7.99 ± 0.04	9.66 ± 0.08	10.3 ± 0.17
3552 Don Quixote	-	-	-	-	-	-	-
Feature Description	Sharp dip	Plateau	Dip	Plateau	Low bound of 10μm feature	Shoulder minor peak	Peak of 10μm feature

Note. — Positions and locations of various features common to the mid-IR spectra of the asteroids analyzed. Measurements based on Spitzer Space Telescope except those marked with a star (*) indicating observations from the SOFIA spectra. The letters P, D, and S indicate whether the feature is a peak, dip, or shoulder, while the corresponding number gives the *approximate* position of the feature. Each feature is also briefly described. An X indicates the feature was not present in the spectrum while a dash (-) indicates there was no coverage of the relevant wavelength region. The X? symbol, used only for (190) Ismene indicates that while this wavelength region was covered, systematic issues in the spectrum complicates the interpretation of individual features.

Table 3.5b. Location of Common Spectral Features

Asteroid	P_{11}/S_{11} (μm)	$D_{12.5}$ (μm)	P_{13} (μm)	$P_{14.5}$ (μm)	P_{17} (μm)	P_{20} (μm)	Shape of 10 μm feature
46 Hestia	X*	X*	X*	-	-	20.74 ± 0.57*	X
65 Cybele	11.68 ± 0.12	12.27 ± 0.07	13.30 ± 0.04	14.23 ± 0.03	17.66 ± 0.01	-	Trapezoidal
87 Sylvia	11.2 ± 0.07	12.03 ± 0.11	12.63 ± 0.03	15.00 ± 0.31	17.39 ± 0.35	20.13 ± 0.45	Trapezoidal
140 Siwa	10.9 ± 0.09*	12.45 ± 0.11*	11.91 ± 0.15*	-	-	20.07 ± 0.46*	Present
190 Ismene	X?*	X?*	X?*	-	-	X*	X?
267 Tirza	11.21 ± 0.05	12.45 ± 0.09	13.01 ± 0.06	14.27 ± 0.01	16.70 ± 0.06	19.08 ± 0.42	Trapezoidal
269 Justitia	11.72 ± 0.07	12.82 ± 0.07	X	-	-	-	Rounded
336 Lacadiera	11.5 ± 0.03	11.97 ± 0.11	12.51 ± 0.12	-	-	-	Rounded
368 Haidea	X	12.18 ± 0.04	12.64 ± 0.21	14.76 ± 0.08	16.93 ± 0.718	X	Rounded
944 Hidalgo	11.12 ± 0.04	12.28 ± 0.06	12.88 ± 0.04	X	16.47 ± 0.07	19.38 ± 0.06	Trapezoidal
1268 Libya	11.49 ± 0.05	12.30 ± 0.04	13.00 ± 0.08	14.27 ± 0.01	X	19.14 ± 0.06	Rounded
1702 Kalahari	11.5 ± 0.16	12.27 ± 0.05	12.93 ± 0.15	15.11 ± 0.30	17.93 ± 0.85	X	Rounded
3552 Don Quixote	-	-	-	-	16.44 ± 0.53	20.65 ± 0.01	-
Feature Description	Shoulder or minor peak	High bound of 10-μm feature	Minor peak	Peak	Broad peak	Broad peak	

Note. — Positions and locations of various features common to the mid-IR spectra of the asteroids analyzed. Measurements based on Spitzer Space Telescope except those marked with a star (*) indicating observations from the SOFIA spectra. The letters P, D, and S indicate whether the feature is a peak, dip, or shoulder, while the corresponding number gives the *approximate* position of the feature. Each feature is also briefly described. An X indicates the feature was not present in the spectrum while a dash (-) indicates there was no coverage of the relevant wavelength region. The X? symbol, used only for (190) Ismene indicates that while this wavelength region was covered, systematic issues in the spectrum complicates the interpretation of individual features.

Table 3.6. Characterization of the 10-μm feature

Asteroid	Width (μm)	Continuum Slope (Emissivity/μm)	Continuum Removed Peak (μm)	Skew	Spectral Contrast (%)
65 Cybele	4.37 ± 0.12	0.001 ± 0.002	9.68 ± 0.04	0.41 ± 0.07	5.8 ± 0.6
87 Sylvia	4.23 ± 0.12	0.003 ± 0.001	9.68 ± 0.14	0.44 ± 0.10	6.1 ± 0.6
267 Tirza	4.75 ± 0.09	-0.001 ± 0.001	9.80 ± 0.16	0.44 ± 0.09	10 ± 0.8
269 Justitia	4.87 ± 0.07	0.002 ± 0.001	9.64 ± 0.15	0.36 ± 0.09	5.1 ± 0.8
336 Lacadiera	4.34 ± 0.14	0.001 ± 0.003	9.63 ± 0.17	0.46 ± 0.11	4.6 ± 0.9
368 Haidea	3.9 ± 0.06	0.004 ± 0.005	9.26 ± 0.02	0.25±0.06	6.5 ± 2.1
944 Hidalgo	4.87 ± 0.08	0.009 ± 0.002	9.81 ± 0.17	0.49 ± 0.08	11 ± 0.7
1268 Libya	4.56 ± 0.05	0.010 ± 0.002	9.61 ± 0.26	0.41 ± 0.14	6.7 ± 0.7
1702 Kalahari	4.63 ± 0.05	0.014 ± 0.004	9.43 ± 0.12	0.39 ± 0.07	7.3± 1.8

Note. — Band parameters of the 10 μm feature. Band parameters are measured as described in Martin (2022), except for skew (see text).

3.4 Discussion

In general, we see many commonalities in the mid-infrared spectra of the D- & P-type asteroids in our sample and the Trojans. We see evidence of the 10-μm silicate emission features in the spectra of all the asteroids we examined, with the exception of 46 Hestia. In both the Trojans (Martin (2022)) and our sample, we see these features exhibiting both rounded and trapezoidal shapes. The range of spectral contrasts of these features are also comparable to the range of contrasts exhibited by the Trojans: 624 Hektor has an estimated spectral contrast of $\sim$ 15% (Licandro et al. (2011)) and 617 Patroclus has a spectral contrast of $\sim$ 4% (Martin (2022)), while our sample spans contrasts from $4 - 17\%$. Since spectral contrast of the 10-μm feature is associated with high regolith porosity (Martin et al. (2022); Martin (2022)), this finding implies similar regolith surface properties on both Trojans and Main Belt asteroids. Previous authors have suggested the suspension of regolith particles within a 'fairy-castle' structure (Emery et al. (2006); Mueller et al. (2010)) or transparent (in the mid-IR) matrix (Yang et al. (2013)) to explain the high porosities of Trojan surfaces. Our results suggest these mechanisms are also relevant to the surfaces of D- & P-type asteroids outside of the Trojan population.

In addition to similarities in physical regolith properties, our results also suggest mineralogical similarities between the Trojans and D- & P-types in the Main Belt. In particular, the peak or shoulder between 11.2 and 11.4 μm is associated with crystalline olivine, with the range of feature positions associated with the

different Mg# within the crystal structure of olivine (Koike et al. (1993, 2003)). Like Martin (2022), we take the presence of the 11-μm features as indicative of the presence of the Mg-rich olivine endmember, forsterite. We also see evidence of amorphous silicates on the surfaces of asteroids in our sample, in particular, with the presence of a broad peak near 9.8-μm (particularly in continuum-removed space) being indicative of amorphous olivine that is also found in Trojan spectra (Emery et al. (2006); Martin (2022)). Other features our spectra have in common with the Trojans examined in Martin (2022) include the small emissivity peak at 13 μm (ex. 87 Sylvia, 65 Cybele, and 944 Hidalgo) in the overall emissivity dip between 12 and 14 μm, and the broad emission peaks near 17-18 μm, though these features were not attributed to any particular silicate composition. However, there are some slight differences between the Main Belt sample presented here and the spectra of the Trojans in Martin (2022) in terms of the shape of the 10-μm feature: our Main Belt asteroids have flatter continuum slopes and skew to shorter wavelengths. As noted in Martin (2022), 10-μm features are not well reproduced by meteoritic analogs in the ASTER spectral library. Martin (2022) identified ALHA 77003, Isna, Happy Canyon, and Allende meteorites as the closest matches to the Trojan asteroids. The 10 μm features of these meteorites tend to have more leftward skews than the Trojans, as do the 10 μm features of the asteroids in our Main Belt samples. Though the physical mechanism responsible for the skewing the 10-μm feature to longer wavelengths is unclear, with their leftward skews Main Belt asteroids may provide a better match to meteoritic analogs, suggesting that this population is well represented in meteoritic collections.

In the long wavelength region we observe emission peaks near 20 μm are generally associated with olivines and pyroxenes, with olivines showing additional structure including a peak near 24 μm (Koike et al. (1993)). While 46 Hestia lacks evidence of a 10-μm feature, we do see silicate emission features associated with silicates in the 20-μm region. The spectrum of 944 Hidalgo shows the additional olivine silicate peaks most clearly, while these peaks are less clear for 267 Tirza and 1268 Libya. We suggest that this difference may be due to mixing of olivine and pyroxene in the spectra of 267 Tirza and 1268 Libya. Pyroxenes show a prominent and broad long wavelength peak between 19 and 20 μm (Chihara et al. (2002)) consistent with this interpretation. Additionally, 267 Tirza shows a 9.3-μm peak associated with pyroxene at shorter wavelengths (Chihara et al. (2002)). Alternatively, the sharp peaks of crystalline olivines and pyroxenes can be broadened by a higher percentage of amorphous silicates (Martin (2022)), so a higher fraction of amorphous silicates may be responsible for the less distinct peaks of 267 Tirza and 1268 Libya. We conclude that, like the Trojans, mixtures of anhydrous olivines and pyroxenes can explain the mid-infrared spectral features of the majority of the asteroids in our sample.

In Martin (2022) VNIR spectral slope was found to be correlated with the spectral contrast of the 10-μm feature among the Jupiter Trojans. Therefore, we might expect the objects with redder VNIR spectral slopes,

e.g. the D-types(267 Tirza, 336 Lacadiera, 368 Haidea, 944 Hidalgo, and 1702 Kalahari) and 269 Justitia would all have high spectral contrasts. While the asteroids with the three highest spectral contrasts (944 Hidalgo, 267 Tirza, and 1702 Kalahari) are all D-types (Neese (2017)), the more moderate spectral contrasts of 336 Lacadiera, 368 Haidea, and 269 Justitia do not align with this expectation. In particular, with 269 Justitia's exceptionally red slope (Hasegawa et al. (2021)), we would expect 269 Justitia to have a prominent 10-μm feature, but its spectral contrast is comparable to the more moderately sloped P-types. The authors in Hasegawa et al. (2021) hypothesize that 269 Justitia's extreme red spectral slope in the VNIR suggests this asteroid originated from the 20 - 30 AU region. Similarly, Martin (2022) suggests a cometary or Kuiper Belt origin for the Trojans based on their spectral similarity to comets. While 269 Justitia's 10-μm emission feature resembles the rounded 10-μm emission features of some Trojans (e.g. 617 Patroclus-Menoetius in Martin (2022); Mueller et al. (2010)) supporting a common distant outer Solar System origin for both 269 Justitia and the Trojans, the spectrum of 269 Justitia shows additional spectral structure (a series of peaks and dips from 7.5 - 10 μm superimposed on the short wavelength 10-μ shoulder) not seen among the Trojans, potentially indicating an additional compositional component present on 269 Justitia that is absent from the Trojans and complicating the interpretation that 269 Justitia and the Trojans are sourced from the same population.

We note that two of the D-types in our sample, 944 Hidalgo and 3552 Don Quixote, are unique among our sample population for their high eccentricities ($e > 0.5$) and semimajor axes ($a > 4.0$) AU. Both 944 Hidalgo and 3552 Don Quixote are extinct comet candidates, with 3552 Don Quixote likely originating from the Jupiter Family Comet (JFC) population (Weissman et al. (2002)). The spectra of 944 Hidalgo and 3552 Don Quixote also resemble those of 10P/Tempel 2 and 49P/Arend-Rigaux, two JFCs, with their 10- and 20-μm silicate emission features Kelley et al. (2017). The resemblance of the mid-infrared spectrum of 3552 Don Quixote to comets has also been noted in Mommert et al. (2014). That paper also noted evidence of cometary activity on 3552 Don Quixote including a coma and tail. The resemblance of 944 Hidalgo and 3552 Don Quixote to comet populations in the mid-infrared lends support to the hypothesis that these objects originated in cometary populations.

The spectrum of 368 Haidea represents an exception to the trends described above. 368 Haidea lacks a strong peak or shoulder at 11 μm and its continuum-removed peak is shifted to shorter wavelengths resulting in a highly leftward skew. The lack of an 11 μm features suggests that unlike the other asteroids in the sample, 368 Haidea is olivine-poor. In addition, 368 Haidea's strongest peaks are located at 9.2 μm and 10.5μm, both prominent peaks associated with pyroxenes, particularly enstatite (Chihara et al. (2002)). However, shortward shifts of the 10-μm feature, in concert with weakening 11 μm olivine features have been associated with increasing degrees of aqueous alteration in meteorites, leading to the alternative conclusion that 368

Haidea may be hydrated (Beck et al. (2014)). This interpretation is supported by the spectral similarity (in the VNIR and mid-IR) of 368 Haidea to the Tagish Lake meteorite noted in Vernazza et al. (2013). The Tagish Lake meteorite has been shown to have widespread evidence of aqueously altered minerals, including phyllosilicates (Zolensky et al. (2002); Gilmour et al. (2019)). While the pyroxene-rich and phyllosilicate-rich interpretations of 368 Haidea imply different geochemical histories for this asteroid, the lack of strong olivine features in the mid-infrared spectrum of 368 Haidea clearly distinguishes it from the Trojans (see Figure 3.5).

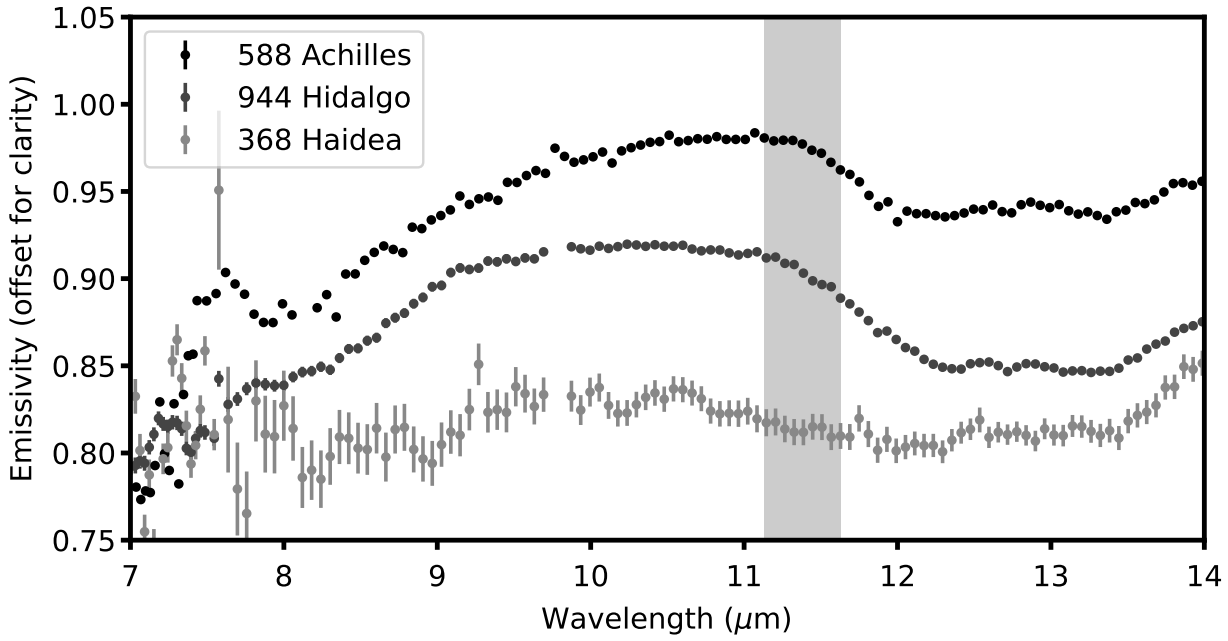

Figure 3.5 Comparison of the spectra of 588 Achilles from Martin (2022), 944 Hidalgo and 368 Haidea. In the VNIR, 588 Achilles, 944 Hidalgo, and 368 Haidea are all classified as D-types and have similar albedos yet 368 Haidea lacks a strong peak or shoulder in the 11 μm region indicative of olivine (see highlighted region). Comparing the spectra of 944 Hidalgo and 588 Achilles, we can also see how the asteroids examined in this work have shallower continuum slopes and more leftward skewed 10 μm feature than the Trojans in Martin (2022).

Overall, we see that the majority of the primitive asteroids in our sample, with the exception of 368 Haidea, resemble both each other and the Trojans. The similarity in spectral shape of the 10-μm features extends to a similarity in both anhydrous silicate composition (olivine and pyroxene mixtures) and high regolith porosity. Asteroids that resemble the Trojans in this way include both D- & P-types. Some major divergences from the spectra of the asteroids examined in this paper and previously published Trojan spectra are the lower continuum slopes and leftward skews of the 10 μm features seen in our sample. In the Trojans, the 10 μm feature tends to have a continuum slope that increases steeply with increasing

wavelength and rightward skewing 10 μm features (Martin (2022)). The mineralogical significance of these spectral differences, however, is unclear.

The distinctive spectral features of 368 Haidea indicate a composition poor in olivine, distinguishing it from the other asteroids in our sample and the Trojans (Martin (2022); Emery et al. (2006)). The shortward shift of 368 Haidea's features may be due to either a particularly pyroxene or phylosilicate rich composition, 368 Haidea does not originate from the same source populations as the Trojans and other Main Belt D-types. Comparing 368 Haidea to the other D-types in our sample demonstrates the need for observations outside of the VNIR region, particularly for asteroids with few spectral features in the VNIR, to augment our understanding of the compositions of these asteroids. The recently launched JWST will be able to extend mid-infrared observations to a larger population of primitive asteroids, sampling cooler and fainter populations of primitive small Solar System bodies and supplement our understanding of ground-based VNIR asteroid taxonomies.

3.5 Conclusions

Combining new observations from the SOFIA observatory and archival data from the Spitzer Space Telescope, we present the mid-infrared (5-40 μm) spectra of thirteen primitive Main Belt D- & P- type asteroids. While these two asteroid populations resemble each other in the VNIR, a lack of strong spectral features in the VNIR limits the extent to which we can unambiguously determine their compositions. We analyze the spectra of these asteroids, including using techniques to characterize the 10-μm region developed in Martin (2022), to compare the composition and regolith properties of D- & P-types in the Main Belt to the Jupiter Trojans. We find that the majority of D- & P- type Main Belt asteroids resemble the Trojans in the mid-IR, with high regolith porosities and a silicate composition incorporating crystalline and amorphous olivines and pyroxenes, suggesting a common origin for primitive asteroids in the Main Belt and Trojan swarms. However, we also note some differences in the general shapes of the 10-μm features of Main Belt and Trojan asteroids including lower continuum slopes and leftward skewing 10 μm emission features among Main Belt asteroids as compared to Trojans. In addition, we identify a D-type asteroid, 368 Haidea, that is distinguished from both the Trojans and Main Belt asteroids in our sample by its particularly olivine-poor composition. Despite their shared D-type classification, 368 Haidea does not resemble D-type Jupiter Trojans, suggesting that similarity in VNIR spectra does not guarantee a shared surface composition as reflected by silicate features in the mid-infrared.

3.6 Acknowledgements

The authors would like to thank Dr. Maggie McAdam for her assistance in preparing the SOFIA proposal. This work is based in part on observations made with the NASA/DLR Stratospheric Observatory for Infrared Astronomy (SOFIA). SOFIA is jointly operated by the Universities Space Research Association, Inc. (USRA), under NASA contract NNA17BF53C, and the Deutsches SOFIA Institut (DSI) under DLR contract 50 OK 2002 to the University of Stuttgart. Financial support for this work was provided by NASA through award #08-0105 issued by USRA. This work is based in part on archival data obtained with the Spitzer Space Telescope, which was operated by the Jet Propulsion Laboratory, California Institute of Technology under a contract with NASA. This research has made use of data and/or services provided by the International Astronomical Union's Minor Planet Center. This majority of this work was completed at Northern Arizona University in Flagstaff, Arizona. Northern Arizona University sits at the base of the San Francisco Peaks, on homelands sacred to Native Americans throughout the region. We honor their past, present, and future generations, who have lived here for millennia and will forever call this place home.

Chapter 4

The Abundance of Red-Sloped Asteroids in the Main Belt

This chapter contains work to be published in a scientific journal in the near future. As such, it is presented in manuscript form and the submitted manuscript will be similar to this version.

ABSTRACT

Red ($S > 10\%/100$ nm) spectral slopes are common among Centaurs and Trans-Neptunian Objects (TNOs) in the outer Solar System. Interior to and co-orbital with Jupiter, the red ($S \sim 10\%/100$ nm slopes of D-type Main Belt and Jupiter Trojan asteroids are thought to reflect their hypothesized shared origin with TNOs beyond the orbit of Jupiter. In order to quantify the abundance of red-sloped asteroids within the Main Belt, we conduct a survey using the NASA IRTF and Lowell Discovery Telescope, following up on 28 candidate red objects identified via spectrophotometry from the Sloan Digital Sky Survey's Moving Object Catalog to confirm their steep spectral slopes and determine their taxonomic classifications. We find that our criteria for identifying candidate red objects from the Moving Object Catalog result in a $\sim 50\%$ confirmation rate for steeply red sloped asteroids. We also compare our observations of Main Belt asteroids to existing literature spectra of the Jupiter Trojans and steeply red-sloped Main Belt asteroids. We show that some red sloped asteroids have approximately linearly increasing reflectance with increasing wavelength, while other red-sloped asteroids show a flattening in slope at longer near-infrared wavelengths, indicating a diversity among the population of spectrally red Main Belt asteroids suggestive of a variety of origins among the population of steep sloped asteroids.

4.1 Introduction

Many outer Solar System populations, including trans-Neptunian Objects (TNOs), comets, and Centaurs are characterized by their red ($S > 10\%/100$ nm) colors in the visible and near infrared (VNIR) (e.g. Sheppard (2010); Perna et al. (2010); Lamy & Toth (2009)). That is, their VNIR spectra show increasing reflectance with increasing wavelength. To precisely quantify the 'redness' of a spectrum, many studies use spectral

slope (S), typically measured as a percentage increase in reflectance over a certain spectral range, usually 100 nm, relative to a reference wavelength, typically 550 nm (Hainaut et al. (2012); Doressoundiram et al. (2008)). The colors of small bodies can also be quantified using color indices, or the difference in astronomical magnitude of an object as seen in different standard filter sets, a photometric technique that is particularly useful for quantifying the color of distant, faint objects like TNOs. Among TNOs, the reddest surfaces are found among the cold Classical Kuiper Belt object population and the extremely distant inner Oort cloud objects which are thought to have formed and remained far from the Sun (Sheppard (2010); Doressoundiram et al. (2008)). Some authors have interpreted this trend to reflect a primordial color gradient within the early Solar nebula, with objects that initially formed at high heliocentric distances retaining more volatile organics, which become red upon irradiation (Brown et al. (2011)).

The general trend of increasing abundance of spectrally red materials at increasing distances is also seen among small body populations interior to and co-orbital with Jupiter. In the Main Belt, the proportion of dark, red-slope asteroids increases with increasing heliocentric distance (Gradie & Tedesco (1982); DeMeo & Carry (2013)). Further out, in the Jupiter Trojans, a population of asteroids co-orbital with Jupiter at 5.2 AU, asteroids are classified into the less red (LR) and red (R) spectral groups, with the majority of Trojans belonging to the R group Emery et al. (2010). The average VNIR slope of an R group Trojan ($\sim 10\%/100$ nm, Wong et al. (2014)) is slightly steeper than a typical D-type Main Belt asteroid ($\sim 9\%/100$ nm, Gartrelle et al. (2021a)), the reddest class of asteroids commonly found in the Main Belt. The spectral slopes of small bodies interior to and co-orbital with Jupiter, such as Trojans and D-type Main Belt asteroids, are generally shallower than those of the reddest small bodies in the outer Solar System, such as TNOs and Centaurs, which can have ultra-red slopes as steep as $\sim 40 - 55\%/100$ nm (Hainaut et al. (2012); Wong & Brown (2016)), further demonstrating the association of steep red spectral slopes with outer Solar System populations.

The current distribution of small Solar System bodies does not perfectly reflect initial conditions within the protoplanetary nebula (DeMeo & Carry (2013)). The processes of planetary formation and migration have led to the displacement of small bodies from their formation locations via gravitational interaction, with many models positing that the migration of the gas giant planets resulted in the delivery of outer Solar System materials from the proto-Kuiper Belt to the Main Belt (Levison et al. (2009); Walsh et al. (2012)), resulting in the diversity of asteroid spectral types we see in the Main Belt today. Based on their spectral similarity to TNOs and Centaurs, red-sloped D-types and R group Trojans have been identified as possible migrants that originated from a source population beyond the present day orbit of Jupiter (DeMeo & Carry (2013); Wong & Brown (2016)). Dynamical simulations also support this idea, suggesting the Trojans were captured from the same parent population as the present day TNOs (Morbidelli et al. (2005); Nesvorný

et al. (2013); Pirani et al. (2019)). Thus, the presence and distribution of red, TNO-like material can be used to provide indirect constraints on the mechanisms of planetary formation. The constraints provided by observational studies can then be used to test the predictions of dynamical models and further refine their accuracy. The recent serendipitous discovery of extremely red, TNO-like asteroids within the Main Belt has sparked discussion of dynamical implications of the presence of objects that could have migrated from 20-30 AU to Main Belt (Hasegawa et al. (2021)).

The distribution of red material within the Main Belt has been the subject of recent observational surveys. In DeMeo et al. (2014), the distribution of D-types in the inner Main Belt (interior to 2.5 AU) is investigated by identifying D-type "candidate" asteroids via Sloan Digital Sky Survey (SDSS) photometry and confirming the taxonomy of these asteroids using near-infrared spectroscopy from the NASA Infrared Telescope Facility (IRTF). Those authors observed 13 candidate D-types in the inner Main Belt and confirmed the D-type taxonomy of three of these candidates, resulting in a $\sim$ 20% confirmation rate (DeMeo et al. (2014)). Similarly, in this work, we follow up on candidate red asteroids with slopes in excess of the average R group Trojan identified using SDSS photometry using the NASA IRTF and Lowell Discovery Telescope (LDT). Unlike DeMeo et al. (2014), we seek to identify asteroids that are redder than the average Main Belt D-types, using the slightly steeper average spectral slope of the R group Trojans as the criterion for selection those steeply-sloped red objects currently located in the Main Belt of potentially sourced from the same population as the TNOs.

4.2 Methods

4.2.1 Target Selection

To identify candidate red Main Belt asteroids, we used the Sloan Digital Sky Survey (SDSS) Moving Object Catalog (MOC) (Ivezić et al. (2002)). The SDSS captures photometric measurements of objects in the *u*, *g*, *r*, *i*, and *z* filters in sequential order. We removed all observations in the MOC with apparent magnitudes fainter than 22.0, 22.2, 22.2, 21.3, and 20.5 for each of the *u*, *g*, *r*, *i*, and *z* filters, respectively, as these magnitudes correspond to the limiting magnitudes for 95% survey completeness (Ivezić et al. (2001)). Following DeMeo & Carry (2014), observations taken during non-photometric conditions were removed from the target list by removing those observations flagged with *edge, badsky, peakstooclose, notchecked, binned4, nodeblend, deblenddegenerate, badmovingfit, toofewgooddetections,* and *stationary.* These conditions narrowed the target list from over 220,000 observations to approximately 68,000 moving object observations.

The asteroid magnitudes reported in the MOC were converted to measurements of spectrophotometric reflectance by calculating color indices for each asteroid (g-r, r-i, and i-z), subtracting solar colors from each color index, and normalizing to the r band reflectance value. The effective wavelength of each observation was estimated as the center wavelengths of the u, g, r, i, and z filters, (0.3551, 0.4686, 0.6166, 0.7480, and 0.8923 μm, respectively). Spectral slopes were measured directly from the photometric data by fitting a line to the solar corrected g, r, i, and z measurements. To quantify the error in slope, we generated 20,000 synthetic spectrophotometric measurements for each candidate asteroid by drawing values from a Gaussian distribution with a mean equal to the observed normalized color indices and error drawn from the propogated error in reflectance. For each synthetic observation, slope was calculated by fitting a line to the synthetic spectrophotometry. The slope error was estimated using the standard deviation of all 20,000 synthetic spectrophotometric measurements. Asteroids with spectral slopes exceeding 12% per 100 nm were chosen as candidate targets to ensure only the reddest objects were selected (the average slope of R group Trojans was found to be 10.3% per 100 nm using the same slope estimation method using data from Emery et al. (2010)).

Targets with semimajor axes less than 2.5 AU were excluded, since D-types in the inner Main Belt have already been surveyed using similar methods in DeMeo et al. (2014). This resulted in a list of 75 candidate objects with at least one slope measurement exceeding the 12% per 100 nm. We refined this list further by requiring objects with multiple slope measurements to have consistently steep slopes. Similarly, if independent albedo measurements of an object were available (Mainzer et al. (2019)), we required objects on the most restrictive final list to have low (< 0.15) albedos. In total, 60 of the 75 objects were included in the final candidate list. The remaining 15 objects that did not meet the strictest criteria for inclusion were used as a list of lower priority backup targets.

The targets we observed were ultimately determined by their visibility from the observing sites during the survey period. We prioritized asteroids that reached low (< 1.5) airmasses for several hours a night over at least ten days of each observing semester. Because both telescopes we used are located at mid-latitudes in the Northern Hemisphere, we favored targets with moderately negative to positive declinations during the observing period. We also prioritized targets that were visible from both observing locations in the same semester. To get the best estimate of spectral slope, our signal-to-noise requirement restricted observations to asteroids with V magnitudes < 19.0.

4.2.2 NASA Infrared Telescope Facility Observations

We used the SpeX Spectrograph (Rayner et al. (2003)) on the NASA Infrared Telescope Facility (IRTF) in prism mode to observe candidate asteroids in the near-infrared (0.7 - 2.5 μm). The IRTF has a long history of use in asteroid surveys (Marsset et al. (2020)), which we leveraged to obtain as accurate measurements of spectral slopes as possible. Observations of each target were taken at airmasses < 2.0 with the slit aligned to the parallactic angle to reduce the chance of variation in the spectral slope due to differential atmospheric refraction. For bright targets, we used the GuideDog infrared slit viewer to ensure each target was well aligned in the slit, while for faint targets ($V > 17.5$) we used the MIT Optical Rapid Imaging System (MORIS) (Bus et al. (2011); Gulbis et al. (2010)) to guide on a visible wavelength image of the target to ensure slit alignment. Each observation used a local standard star and a solar standard star to correct for the solar spectrum. Local standards were chosen by querying the SIMBAD astronomical database for bright (12 - 6 V mag) G dwarf stars within a 7 degree radius of the mean position of the asteroid on each night (Wenger et al. (2000)). Solar standard stars were selected from a list of commonly used solar analogs (see Marsset et al. (2020)). Observations of each asteroid were bracketed by observations of the local standard, returning to obtain local standard spectra after $\sim$ 60 minutes of integration time on each asteroids. Solar standards were observed once a night at low (< 1.5) airmasses. This observing strategy allowed us to produce reflectance spectra for each object by averaging different calibrated versions of that object's spectrum from throughout each night. To account for the sky background emission, spectral measurements of each target, solar, and local standards were taken in A-B pairs. Spectra were extracted from raw FITS files using SpeXtool. SpeXtool performs flat field correction, wavelength registration, A-B pair subtractions, telluric correction, and conversion from absolute fluxes to relative reflectance spectra (Cushing et al. (2004)). We observed a total of 15 targets with the IRTF.

The correction from absolute flux (uncorrected for solar color) to reflectance was accomplished using both the local and solar standards: first the asteroid spectrum was divided by the spectrum of the local standard to produce a locally-corrected spectrum. Then, the solar analog spectrum was divided by the average spectrum of the local standard to produce a solar comparison spectrum and confirm the similarity of the local standard to the solar analog spectrum. Then, the locally-corrected spectrum was divided by the solar comparison spectrum. The effect of this correction is to account for both variations in local atmospheric transparency (accomplished using the local standard) as well as correct for solar color (using the solar standard). Reflectance spectra taken using the IRTF were normalized to 1 at 1.0 μm. Typically, the differences between the solar analog and local standard spectra were confined to regions of telluric absorption and introduced minimal variation in slope. For IRTF spectra heavily affected by differences in

telluric absorption between the solar and local standard spectra, we corrected the spectra using only the local standard if the local standard used had a J-H color index (Cutri et al. (2003)) no more than ± 0.1 magnitudes away from the solar J-H value (Casagrande et al. (2012)). Asteroids for which this correction was performed are noted in Table 4.1 with an 'X' in the solar standard column. The choice to include or exclude the solar standard in the reduction did not affect the slope significantly enough to change the classification of an asteroid from red to not red, or vice versa. This finding is in line with the results of Marsset et al. (2020), which found that slope varies by less than 1% per μm per 0.1 difference in airmass: all our targets were observed within at most 1 airmass of each other. This variation in slope is comparable to the slope variance between G2V and G5V stars (Marsset et al. (2020)).

Table 4.1. Observation circumstances for asteroids observed with the NASA Infrared Telescope Facility

Asteroid	Provisional Designation	Obs. Start (UTC)	RA/Dec	Mag. (V)	Airmass Range	Exp. (min)	Local Standard	Solar Standard
(203) Pompeja	A879 SA	03-07-2022 09:10	12:37:30 -05:20:58	13.1	1.51-1.15	77	HD 110029	SA 105-56
(467) Laura	A901 AA	02-05-2023 13:18	12:25:29 -07:34:18	16.0	1.14-1.13	40	HD 108808	SA 105-56
(1947) Iso-Heikkila	1935 EA	07-16-2021 11:56	23:05:31 -20:02:47	16.6	1.51-1.34	16	HD 220145	X
(3248) Farinella	1982 FK	02-17-2022 10:25	12:51:27 -02:48:12	16.7	1.54-1.24	64	HD 111662	SA 105-56
(5819) Lauretta	1989 UZ4	09-07-2021 09:35	00:39:27 -00:29:44	16.8	1.30-1.10	60	HD 4096	SA 115-271
(7562) Kagiroino-Oka	1986 WO9	05-15-2021 10:52	15:13:48 -14:44:44	16.8	1.43-1.25	50	HD 130958	SA 105-56
(9934) Caccioppoli	1985 UC	08-06-2022 10:58	23:09:21 -31:03:37	16.4	1.77-1.67	32	HD 219180	X
(21867)	1999 TQ251	07-25-2022 11:23	20:21:49 -01:49:12	17.9	1.26-1.1	68	HD 191595	SA 112-1333
(21867)	1999 TQ251	07-28-2022 11:37	20:19:51 -02:04:31	17.9	1.48-1.14	60	HD 191595	SA 112-1333
(22110)	2000 QR7	07-20-2021 09:39	18:33:21 -19:06:07	17.5	1.37-1.30	52	HD 172404	SA 112-1333
(22422) Kenmount Hill	1995 YO5	07-25-2022 10:00	20:06:51 -28:13:45	18.0	1.50	40	HD 189327	SA 112-1333
(22422) Kenmount Hill	1995 YO5	07-28-2022 09:55	20:04:05 -28:27:58	18.0	1.52-1.50	52	HD 189327	SA 112-1333
(23690)	1997 JD14	05-15-2021 06:00	12:26:33 -04:32:01	18.1	1.16-1.10	48	HD 108808	SA 105-56
(25835) Tomzega	2000 EO20	02-05-2023 14:23	11:38:43 -12:15:02	18.3	1.77-1.27	72	HD 100044	X
(25835) Tomzega	2000 EO20	02-10-2023 13:47	11:37:07 -12:06:01	18.2	1.94-1.24	92	HD 100044	X
(27378)	2000 EG55	02-23-2022 09.25	10:33:39 +24:37:11	18.0	1.27-1.00	160	HD 90183	SA 102-1081
(31056)	1996 RK25	10-28-2022 09:51	02:10:40 +00:16:44	17.4	1.11-1.07	68	HD 15166	SA 93-101
(31499)	1999 CS64	01-09-2021 12:25	07:14:09 +19:26:30	16.7	1.28-1.15	48	BD+161450	SA 98-978
(60378)	2000 AL165	01-23-2023 11:01	07:15:36 +26:56:30	17.7	1.32-1.08	72	HD 53532	SA 102-1081
(52628)	1997 WO3	05-15-2021 08:03	14:35:03 -19:06:01	17.9	1.39-1.29	52	HD 130958	SA 105-56
(52628)	1997 WO3	05-19-2021 09:12	14:31:44 -18:46:50	18.0	1.58-1.28	44	HD 130958	SA 105-56
(67244)	2000 EH58	08-13-2022 12:07	21:52:00 -12:58:43	18.3	1.77-1.08	52	HD 202497	X
(76391)	2000 FP7	08-07-2022 09:26	21:14:31 -22:18:15	17.9	1.49-1.35	96	HD 202153	X
(80052)	1999 JV62	05-19-2021 11:30	15:02:19 -15:00:21	17.7	1.78-1.40	52	HD 135532	SA 105-56
(81819)	2000 KS35	08-20-2022 09:16	21:40:18 -16:34:04	17.4	1.29-1.24	52	HD 206835	X
(85911)	1999 CY91	08-13-2022 09:47	21:09:41 -27:29:15	17.9	1.62-1.48	84	HD 224251	X

Note. — For each asteroid, we report the name, provisional designation, observation start time, position of the asteroid in right ascension and declination at the start of observations, visible magnitude (as retrieved from JPL's Horizons online ephemeris service), the range of airmasses during the observation, total exposure time, and solar and local standard stars used. Observations with an 'X' were heavily affected by telluric absorptions when correction to the solar standard was performed, so for these observations we only used the local standard during flux to reflectance conversion (see text).

4.2.3 Lowell Discovery Telescope Observations

We used the DeVeny Spectrograph's DV1 grating (Bida et al. (2014)) on the Lowell Discovery Telescope (LDT) to observe candidate asteroids in the visible (0.3 - 0.9 μm). Our observation strategy for the LDT is similar to the observing strategy for the IRTF described in the previous section. Observations of each target were taken at airmasses < 2.0 with the slit aligned to the parallactic angle to reduce the chance of variation in the spectral slope due to differential atmospheric refraction. Each observation used a local standard star and a solar standard star to correct for the solar spectrum. Local standards were chosen by querying the SIMBAD astronomical database for bright (12 - 6 V mag) G dwarf stars within a 7 degree radius of the mean position of the asteroid on each night (Wenger et al. (2000)). Solar standard stars were selected from a list of commonly used solar analogs (see Marsset et al. (2020)). Observations of each asteroid were bracketed by observations of the local standard, returning to obtain local standard spectra after $\sim$ 60 minutes of integration time on each asteroid. Solar standards were observed once a night at low < 1.5 airmasses. This observing strategy allowed us to produce reflectance spectra for each object by averaging different calibrated versions of that object's spectrum from throughout each night.

Data from the LDT were extracted using SPECTROSCOPYPIPELINE (SP) developed for python by Maxime Devogele. SP performs bias subtraction, flat field correction, wavelength registration, telluric correction and conversion from absolute fluxes to relative reflectance (Devogele & Moskovitz (2019)). The correction from absolute flux (uncorrected for solar color) to reflectance was accomplished using both the local and solar standards: first the asteroid spectrum was divided by the spectrum of the local standard to produce a locally corrected spectrum. Then, the solar analog spectrum was divided by the spectrum of the local standard to produce a solar comparison spectrum. The effect of this correction is to account for both variations in local atmospheric transparency (accomplished using the local standard) as well as correct for solar color (using the solar standard). SP also provides a provisional classification of each asteroid according to the Bus-DeMeo taxonomy (DeMeo et al. (2009); Bus (1999); Bus & Binzel (2002)). This classification is accomplished by comparing the normalized asteroid spectrum to the normalized spectra of a collection of 'average' visible spectra for each spectral type and identifying the best fit as the spectral class with the smallest χ^2-goodness-of-fit metric. Reflectance spectra taken using the LDT were normalized to 0.55 μm. The extracted spectra were smoothed and binned using a 10-point wide box filter prior to additional analysis. We observed a total of 19 targets with the LDT.

Table 4.2. Observation circumstances for asteroids observed with the Lowell Discovery Telescope

Asteroid	Provisional Designation	Obs. Start (UTC)	RA/Dec	Mag. (V)	Exp. (min)	Airmass Range	Local Standard	Solar Standard
(203) Pompeja	A879 SA	03-04-2022 11:15	12:39:26 -05:29:17	13.2	2.5	1.53	HD 110029	SA 105-56
(269) Justitia	A887 SA	05-24-2022 10:49	19:09:38 -13:41:10	12.8	6	1.51	HD 180510	SA 110-361
(467) Laura	A901 AA	11-13-2021 06:55	06:24:42 +31:28:21	15.2	15	1.36-1.26	HD 259516	SA 93-101
(1947) Iso-Heikila	1935 EA	08-07-2021 09:24	22:58:17 - 22:28:39	16.2	20	1.84	HD 215393	SA 115-271
(1947) Iso-Heikila	1935 EA	12-02-2022 04:02	02:58:13 +05:58:48	16.4	20	1.25-1.21	HD 17762	SA 93-101
(3248) Farinella	1982 FK	03-04-2022 10:48	12:44:30 -02:28:41	16.4	15	1.38-1.35	HD 111662	SA 105-56
(7562) Kagiroino-Oka	1986 WO9	05-03-2021 08:47	15:24:03 -15:36:23	17	30	1.68-1.60	HD 131864	SA 105-56
(8967) Calandra	4878 T-1	08-07-2021 10:08	00:11:31 +02:04:35	17.6	30	1.19	HD 1386	SA 115-271
(13381)	1998 WJ17	11-13-2021 02:01	00:03:10 +04:00:39	18.0	25	1.34-1.24	HD 224251	SA 93-101
(16551)	1991 RT14	05-03-2021 04:25	10:24:24 +11:16:12	18.3	40	1.15-1.28	HD89525	SA 105-56
(17350)	1968 OJ	05-24-2022 08:12	14:51:37 +04:23:53	18.4	48	1.54-1.33	HD 128593	SA 110-361
(21867)	1999 TQ251	09-04-2022 03:33	19:56:23 -06:30:25	18.3	58	1.37-1.32	HD 187490	SA 112-1333
(22689)	1998 QQ84	11-13-2021 08:03	07:06:40 +13:06:18	18.3	80	1.43-1.15	HD 52634	SA 93-101
(23248) Batchelor	2000 WW178	11-13-2021 09:58	09:08:29 +22:08:22	19.0	90	1.35-1.08	HD 76752	SA 93-101
(27378)	2000 EG55	03-04-2022 09:50	10:26:07 +25:10:37	18.0	40	1.42-1.25	HD 90183	SA 105-56
(31056)	1996 RK25	10-28-2022 08:14	01:55:12 -02:40:58	17.4	30	1.38-1.32	HD 11752	SA 93-101
(31786)	1999 KO13	10-28-2022 09:03	03:01:53 +28:37:45	17.5	25	1.05-1.03	HD 19823	Hya 64
(33693)	1999 KA	11-13-2021 06:07	03:29:42 -01:59:53	17.7	35	1.33-1.27	HD 21316	SA 93-101
(36249)	1999 VT178	05-24-2022 09:27	17:41:11 -06:01:47	18.4	60	1.45-1.33	HD 159006	SA 110-361
(40131)	1998 QJ48	03-04-2022 09:01	11:16:04 -01:01:31	17.6	30	1.34-1.29	HD 97275	SA 105-56
(67141)	2000 AC169	08-07-2021 08:41	21:01:32 - 12:59:20	17.7	30	1.67-1.57	HD 197759	SA 115-271
(81819)	2000 KS35	09-04-2022 06:26	21:41:30 -18:25:11	17.9	44	1.73-1.66	HD 205291	SA 112-1333
(85911)	1999 CY91	09-04-2022 05:04	21:35:30 -15:26:17	18.4	60	1.64-1.56	HD 203812	SA 112-1333
(106063)	2000 SR319	10-28-2022 09:43	04:00:56 +37:06:47	17.2	25	1.03-1.01	HD 26182	Hya 64
(158762)	2003 RS	11-13-2021 05:06	03:07:20 +25:46:45	18.0	35	1.12-1.05	HD 19445	SA 93-101
(246945)	1999 RP116	11-13-2021 02:57	00:51:20 +38.:38:41	18.5	70	1.09-1.01	HD 6664	SA 93-101

Note. — For each asteroid, we report the name, provisional designation, observation start time, position of the asteroid in right ascension and declination at the start of observations, visible magnitude (as retrieved by JPL's Horizons online ephemeris service), the range of airmasses during the observation, total exposure time, and solar and local standard stars used.

4.2.4 Analysis and Spectral Classification

Following spectral extraction and conversion from flux to relative reflectance, we evaluated each spectrum using various classification methods. First, we determined the spectral slopes of each asteroid by performing a linear fit on each normalized spectrum. To estimate errors in spectral slope for each spectrum, we used a Monte Carlo method, generating 1000 synthetic spectra per measurement by drawing reflectance values from a Gaussian distribution centered at the mean reflectance value at each wavelength and error equal to the associated error in reflectance. For each synthetic spectrum, we computed the spectral slope of the best fitting line, taking the mean spectral slope of all 1000 synthetic spectra as the spectral slope measurement, and the standard deviation of the slope measurements as the error. To improve the accuracy of these linear fits, we excluded regions of high noise from the linear fitting process. For the LDT data, we excluded wavelengths $< 0.35\mu$m and $> 1.0\mu$m, fitting slope over the $0.35 - 1.0\mu$m range. For the IRTF data, we excluded wavelengths $> 2.4\mu$m, fitting slope over the $0.8 - 2.4\mu$m range. The resulting linear fit was assessed visually against each spectrum to ensure an appropriate fit. Given a linear fit, we calculate spectral slope as the predicted increase in spectral slope over the 550 - 650 nm range relative to reflectance at 550 nm. That is, spectral slope S as a percentage is given by the equation

$$S(\%) = \frac{R(650nm) - R(550nm)}{R(550nm)} \times 100 \tag{4.1}$$

Where $R(x)$ is the predicted solar corrected reflectance at wavelength x. We also calculated the slope of the R group average spectra from Emery et al. (2010) over the $0.35 - 1.0$ μm and $0.8 - 2.4$ μm ranges. Note that, because many asteroid spectra deviate from perfectly linear that the spectral slopes measured over the visible range ($0.35 - 1.0$ μm) and the near-infrared range ($0.8 - 2.4$ μ m) are not necessarily equal. For the average R group Trojan, we find the average slope from $0.35 - 1.0$ μm, $S_{0.35-1.0\mu m} = 10.7\%$ and the average slope from $0.8 - 2.4$ μm, $S_{0.8-2.4\mu m} = 4.99\%$.

We also classified the asteroids using the Bus-DeMeo taxonomy (DeMeo et al. (2009); Bus (1999); Bus & Binzel (2002)). For the IRTF spectra, we used the Bus-DeMeo Classification Web tool developed by Stephen M. Slivan to determine taxonomic type. This method uses principle component analysis (PCA) to classify asteroid spectra and provides several possible "best fit" classifications. For spectra classified using the Bus-DeMeo classifier, we report the best fit classification as measured by the lowest absolute residual. The Classification Web tool requires either full VNIR coverage (0.45 to 2.45 μm) or NIR coverage (0.85 to 2.45 μm) to classify an asteroid spectrum. Therefore, for objects that were only observed with the LDT, we used the taxonomic classifications provided by the SPECTROSCOPYPIPELINE tool, which determines

spectral type using a χ^2 goodness of fit metric (See Section 2.3, Devogele & Moskovitz (2019)). We note that spectral classifications based only on visible data are less reliable than those taken in the near infrared (or across both the visible and near infrared) as many characteristic spectral features, such the subtle broad but shallow 1.0 - 1.3 μm feature that distinguishes C-type asteroids from X-type asteroids (DeMeo et al. (2009)), are either absent from or located in low signal-to-noise regions of the LDT spectra.

Ten of our targets have full wavelength coverage from both the IRTF and the LDT. For these targets, we used the linear fits we derived to predict reflectance at 0.85 μm, in the region of overlap between the LDT and IRTF data, then scaled the IRTF spectra to the predicted visible flux. The effect of this scaling is to normalize the entire spectrum (0.3 - 2.5 μm) to a value of 1 at 0.55 μm. When combining the data, we excluded LDT data longwards of 1.0 μm due to the greater noise in this region, which was well-characterized in the IRTF spectra. These full wavelength spectra can be classified using the Bus-DeMeo Classification Web tool. Though we performed classifications on the IR-only and visible-only data we do not report these classifications, prioritizing classifications derived using the full wavelength coverage when these data were available. For all classifications that relied on the Bus-DeMeo Classification Web tool, we did not assign a class to asteroids with absolute residuals > 0.1 as none of the Bus-DeMeo taxonomic classes provided a good match to the spectrum.

For spectra obtained with the IRTF, we also calculated synthetic color indices in the near-infrared. In Emery et al. (2010), the LR and R group Trojans were found to form two distinct clusters in (0.85 μm - J) and (J - K) color space. We computed synthetic color indices by averaging reflectance values within $\pm 0.1\mu$m of each band center, e.g. 0.85 μm, 1.25 μm (J band), and 2.2 μm (K band). Average reflectances ($r_{0.85}, r_J, r_K$ were then converted to differences in magnitudes to obtain synthetic color index estimations using

$$(0.85 - J) = -2.5 \log_{10} \left(\frac{r_{0.85}}{r_J} \right) \tag{4.2}$$

and

$$(J - K) = -2.5 \log_{10} \left(\frac{r_J}{r_K} \right). \tag{4.3}$$

4.3 Results

We report the average spectral slopes over 0.8 - 2.4 μm, Bus-DeMeo classification, 0.85 - J and J - K color indices for all asteroids observed using the NASA IRTF in Table 4.3. The individual spectrum for each

asteroid is also displayed alongside the average spectra for the R and LR group Trojans from Emery et al. (2010) in Figure 4.1. We observed a total of 22 asteroids with the IRTF, 15 of which were drawn from the final, most restrictive list of SDSS MOC 'red' candidate objects with multiple steep slope measurements and/or low albedos. Six of the other asteroids were drawn from the backup list of SDSS MOC candidates that had at least one steep slope observation, but did not consistently show high slopes, and the seventh was (203) Pompeja, which was observed after its steep spectral slope was reported in Hasegawa et al. (2021). Of those 15, 10 asteroids have slopes equal to or exceeding the average R group Trojan and 4 are classified as D types.

Table 4.3. Slope measurements and classifications for asteroids observed with the IRTF

Asteroid	Provisional Designation	$S_{0.8-2.4\mu m}$ (%/100nm)	0.85 - J	J - K	Bus-DeMeo classification
(203) Pompeja	A879 SA	1.85 ± 0.01	0.10 ± 0.01	0.13 ± 0.01	X*
(467) Laura	**A901 AA**	**5.92 ± 0.01**	**0.24 ± 0.01**	**0.34 ± 0.01**	**D***
(1947) Iso-Heikkila	1935 EA	4.17 ± 0.09	0.25 ± 0.01	0.21 ± 0.01	D*
(3248) Farinella	1982 FK	3.91 ± 0.03	0.24 ± 0.01	0.20 ± 0.01	D*
(5819) Lauretta	1989 UZ4	1.97 ± 0.02	0.18 ± 0.01	0.08 ± 0.01	S
(7562) Kagiroino-Oka	1986 WO9	2.78 ± 0.03	0.16 ± 0.01	0.14 ± 0.01	-*
(9934) Caccioppoli	**1985 UC**	**5.81 ± 0.03**	**0.24 ± 0.01**	**0.32 ± 0.01**	**D**
(21867)	**1999 TQ251**	**6.18 ± 0.07**	**0.26 ± 0.01**	**0.33 ± 0.01**	**-***
(22110)	**2000 QR7**	**6.96 ± 0.14**	**0.23 ± 0.01**	**0.38 ± 0.01**	**-**
(22422) Kenmount Hill	**1995 YO5**	**9.91 ± 0.14**	**0.35 ± 0.01**	**0.45 ± 0.01**	**-**
(23690)	**1997 JD14**	**6.63 ± 0.24**	**0.31 ± 0.01**	**0.38 ± 0.02**	**D**
(25835) Tomzega	**2000 EO20**	**7.44 ± 0.22**	**0.32 ± 0.02**	**0.34 ± 0.02**	**-**
(27378)	**2000 EG55**	**8.92 ± 0.07**	**0.36 ± 0.01**	**0.39 ± 0.01**	**-***
(31056)	1996 RK25	1.71 ± 0.04	0.16 ± 0.01	0.05 ± 0.01	S
(31499)	**1999 CS64**	**6.60 ± 0.06**	**0.33 ± 0.01**	**0.31 ± 0.01**	**D**
(60378)	2000 AL165	2.00 ± 0.04	0.16 ± 0.01	0.08 ± 0.01	S
(52628)	1997 WO3	0.34 ± 0.07	0.03 ± 0.01	0.02 ± 0.01	L
(67244)	**2000 EH58**	**6.97 ± 0.12**	**0.32 ± 0.01**	**0.31 ± 0.01**	**-***
(76391)	**2000 FP7**	**7.57 ± 0.07**	**0.34 ± 0.01**	**0.34 ± 0.01**	**-**
(80052)	1999 JV62	1.16 ± 0.09	0.09 ± 0.01	0.07 ± 0.01	S
(81819)	**2000 KS35**	**9.36 ± 0.10**	**0.39 ± 0.01**	**0.40 ± 0.01**	**-***
(85911)	**1999 CY91**	**12.1 ± 0.15**	**0.38 ± 0.01**	**0.48 ± 0.01**	**-***

Note. — For each asteroid, we report the name, provisional designation, spectral slope (as measured over the 0.8-2.4 μm range), 0.85 - J color, K- J color, and Bus-DeMeo classification. **Bolded** entries indicate steep-sloped asteroids, e.g. those whose spectral slopes exceed the average spectral slope of an R group Trojan (4.99 %/100nm) in the infrared. Note that the Bus-DeMeo classification in some cases is ambiguous; for these asteroids, spectral classification was disambiguated by choosing the classification with the lowest absolute residual. Asteroids marked with a class of '-' were not assigned a classification within the Bus-DeMeo system as none of the taxonomic classes in that system gave residuals < 0.1. Classifications marked with an asterisk (*) were derived using both visible and infrared data (See Section 2.4)

Examining the 0.85 - J and J - K color indices of the asteroids observed with the IRTF in comparison to the Jupiter Trojans from Emery et al. (2010) (See Figure 4.2), we note that many of the D-types we identified plot within the main cluster of R group Trojans with 0.85 - J color indices between 0.2 and 0.35 and J - K color indices between 0.15 and 0.4. A cluster of four asteroids; (22422) 1995 YO5, (85911) 1999 CY91, (81819) 2000 KS35, and (27378) 2000 EG55 2000; have 0.85 - J and J - K color indices higher than the majority of R group Trojans, to the upper right of the majority of R group Trojans. We also note the cluster of four asteroids with 0.85 - J values near 0.25 and J - K values higher than 0.25. These asteroids are (467) Laura, (9934) Caccioppoli, (21867) 1999 TQ251, and (22110) 2000 QR7. They plot to the upper left of the main R group cluster, indicating they have higher J - K values than would be predicted from their 0.85 - J values, that is, they are redder at longer wavelengths. Spectrally, these asteroids lack the characteristic "rollover" from steeper red slopes at short wavelengths to shallower red slopes at longer wavelengths (beyond ~ 1.5 μm), showing approximately linearly increasing slopes in in the near-infrared.

We report the average spectral slopes over 0.35 - 1.0 μm and Bus-DeMeo classification for all asteroids observed using the LDT in Table 4.4. The individual spectrum for each asteroid is also displayed alongside the average spectra for the R and LR group Trojans from Emery et al. (2010) in Figure 4.3. We observed a total of 25 asteroids with the LDT, 19 of which were drawn from the final, most restrictive list of SDSS MOC 'red' candidate objects with multiple steep slope measurements and/or low albedos. Four of the other asteroids were drawn from the backup list of SDSS MOC candidates that had at least one steep slope observation, but did not consistently show steep slopes, and the remaining two were (203) Pompeja and (269) Justitia, which were observed after their steep spectral slopes were reported in Hasegawa et al. (2021). Of those 19, 10 asteroids have slopes equal to or exceeding the average R group Trojan and 10 are classified as D types.

Using the JPL Horizons ephemeris service, we retrieved the semimajor axis (a), orbital eccentricity (e), and orbital inclination (i). We also compiled the diameters and albedoes of those asteroids in our sample that were available in the NEOWISE catalog (Mainzer et al. (2019)). These properties, as well as the H magnitude of every asteroid we observed, are available in Appendix A. We visually examined plots of orbital elements a, e, and i versus measured spectral slopes for both the near-infrared and visible data and found no obvious correlations between spectral slope and any of these orbital elements (see Appendix A). Similarly, the binary classification of an asteroid as steep sloped or not did not depend on any of these orbital elements in a straightforward way. We also found no obvious correlations between diameter and spectral slope or diameter and steep sloped classification. Examining the relationship between spectral slope and albedo, we find that the majority of steep sloped asteroids (among those with known albedos) have NEOWISE albedos < 0.15, but low albedo does not guarantee a steep red spectral slope: dark primitive asteroids in our sample

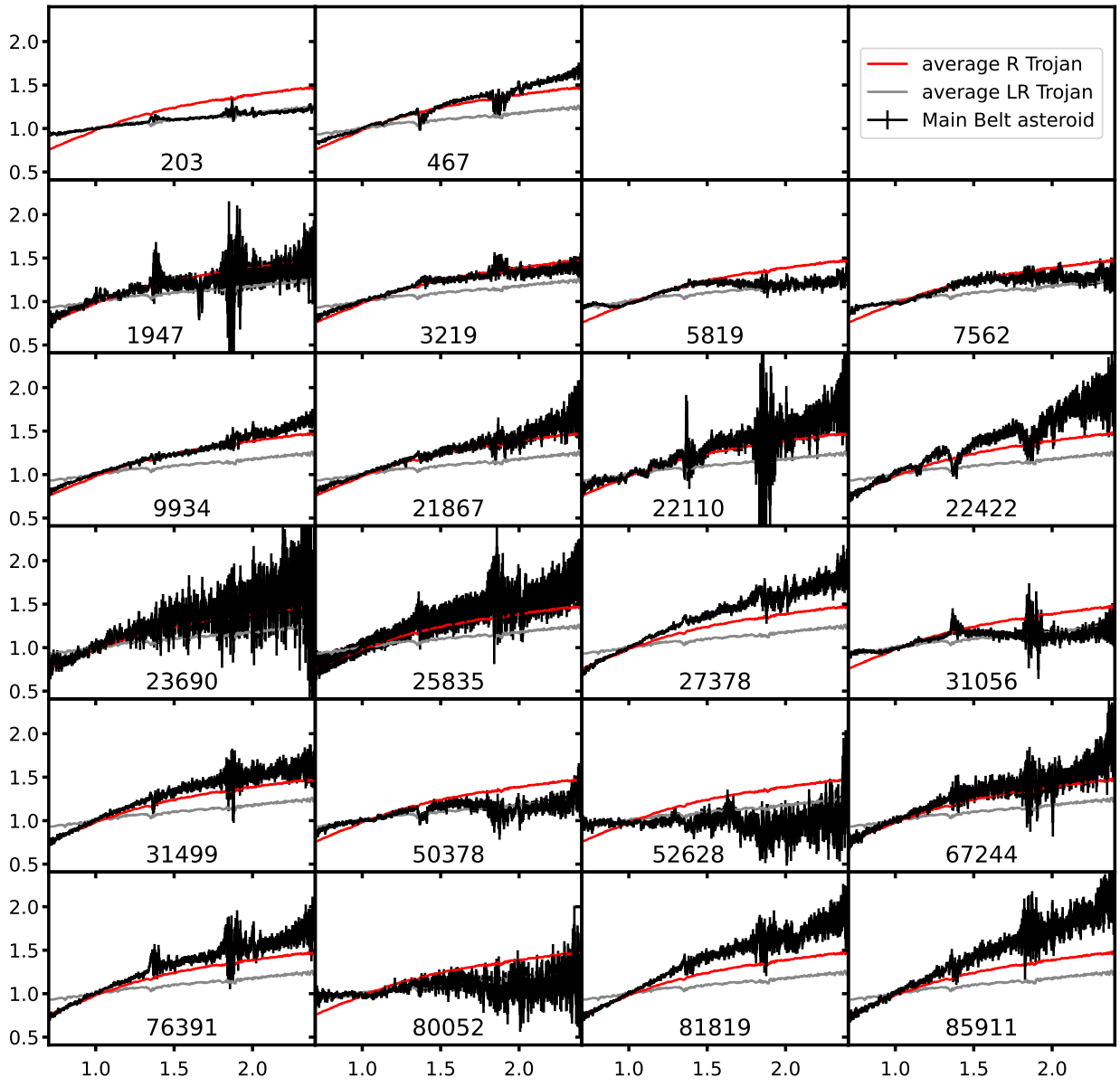

Figure 4.1 Near-infrared reflectance spectra of all candidate red objects observed with the IRTF. All spectra are normalized to 1 at 1 μm and displayed at the same scale to enable direct visual comparison. Each spectrum is plotted alongside the average R and LR group Trojan reflectance spectrum from Emery et al. (2010).

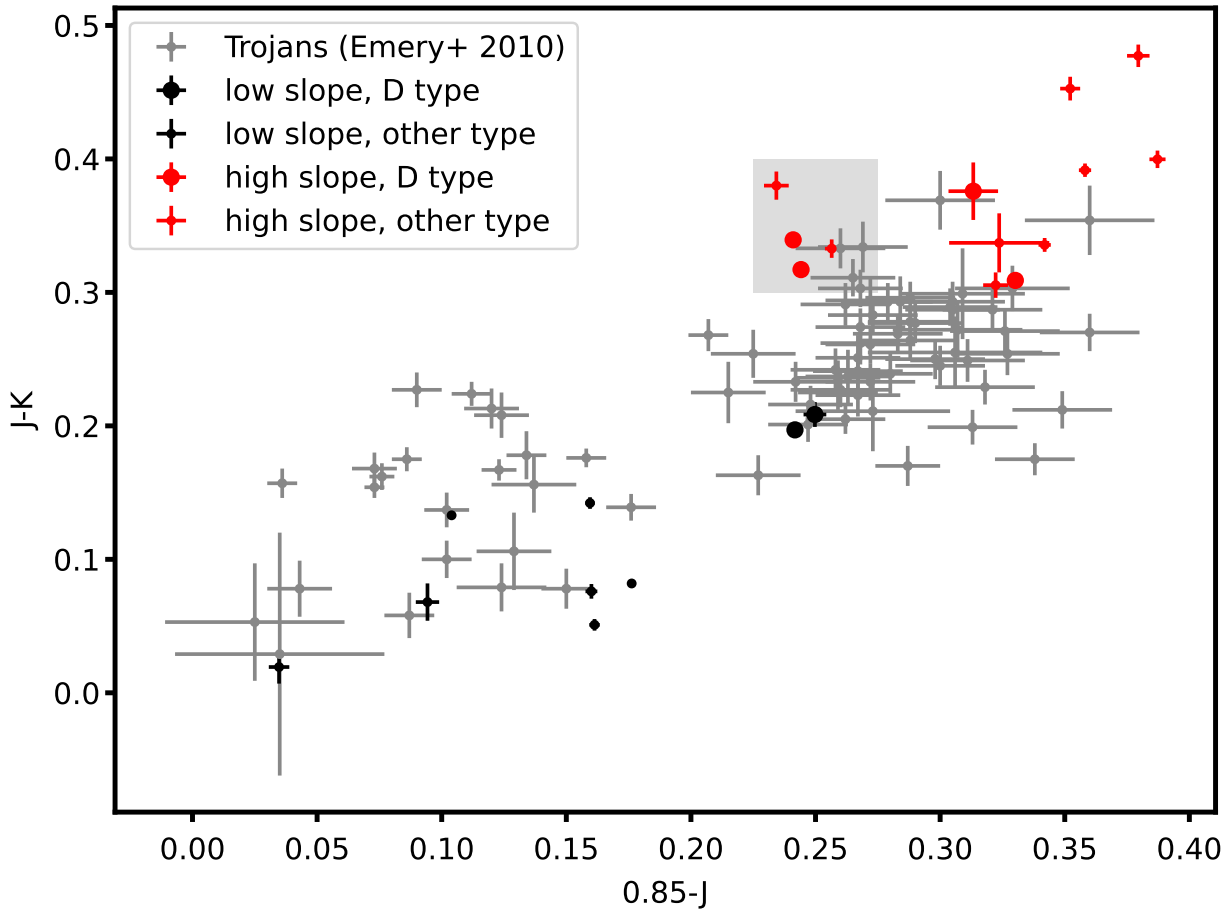

Figure 4.2 0.85 - J and J - K color indices of all asteroids observed with the NASA IRTF. Asteroids with spectral slopes steeper than the average R group Trojan are plotted in red, those with shallower slopes are plotted in black. Asteroids classified as D types are plotted with larger markers than those classified as all other types. The color indices of LR (lower left cluster, grey) and R (upper left cluster, grey) groups from Emery et al. (2010) are plotted for comparison. We note the existence of a subpopulation (boxed) of high-slope asteroids that have higher J - K color values than would be predicted based on their 0.85 - J color if this population was Trojan-like.

show a range of spectral slopes. One exception is the asteroid (7562) Kagiroino-Oka, which has a reported albedo of 0.283 (Mainzer et al. (2019)) a measured visible wavelength slope of 1.25 /μm.

Ten of the asteroids in our sample were observed in both the LDT and the IRTF. As noted in Section 4.2, we prioritize the spectral classifications derived from the combined LDT and IRTF spectra when determining which asteroids are D-types.

4.4 Discussion

The results of this survey can be extrapolated to the rest of the SDSS MOC catalog to estimate the prevalence of various populations of red asteroids in the Main Belt. We estimate the prevalence of a population of red asteroids by calculating the proportion of SDSS MOC-identified candidate red objects we confirmed to be a part of that population, then calculate how many asteroids in the entire SDSS MOC we expect would be that population, assuming the asteroids we observed are a representative sample. For the purposes of this extrapolation, we examine two different sub-populations of 'red' asteroids:

- **D-type asteroids.** This category includes all asteroids classified as D-type. For asteroids with multiple observations, we prioritize the taxonomic type determined using the full-wavelength range (0.35 - 2.5 μm), otherwise, classifications are based on all available spectral data.

- **Steep sloped asteroids.** This category includes all asteroids with measured slopes in the visible and/or near-infrared that exceed the spectral slope of the average R group Trojan over the observed wavelength range. These asteroids may be any taxonomic type.

We summarize the confirmation rates for each of these three asteroid sub-populations in Table 4.5. Our confirmation rate for D-type asteroids based on our selection criteria is $\sim$ 40%. This confirmation rate is significantly higher than the $\sim$ 20% confirmation rate of DeMeo et al. (2014) for candidate D-type inner Main Belt asteroids identified using SDSS MOC spectrophotometry. This may be due to increased prevelance of D-type Main Belt asteroids with semimajor axes $>$ 2.5 AU, but we note that our criteria for inclusion are stricter than those used in DeMeo et al. (2014), as we require our candidate asteroids to have spectral slopes exceeding that of the average R group Trojan asteroid and low geometric albedos (when available). In DeMeo et al. (2014), the criteria for inclusion was at least one D-type classification. As the average R group Trojan has a steeper spectral slope than the typical D-type asteroid (Emery et al. (2010)) and we required an object to have multiple steeply sloped observations and/or a low albedo to be included in our list of candidates, it is more likely that the more stringent inclusion criteria used in this paper led to the higher

Table 4.4. Slope measurements and classifications for asteroids observed with the LDT

Asteroid	Provisional Designation	$S_{0.35-0.7\mu m}$ % / 100 nm	Classification
(203) Pompeja	A879 SA	6.50 ± 0.07	X*
(269) Justitia	**A887 SA**	**18.7 ± 0.06**	**D**
(467) Laura	A901 AA	8.19 ± 0.06	D*
(1947) Iso-Heikila	**1935 EA**	**12.6 ± 0.28**	**D***
(1947) Iso-Heikila	**1935 EA**	**11.8 ± 0.17**	**D***
(3248) Farinella	1982 FK	10.4 ± 0.13	D*
(7562) Kagiroino-Oka	**1986 WO9**	**13.4 ± 0.82**	**-***
(8967) Calandra	4878 T-1	6.64 ± 0.73	K
(13381)	1998 WJ17	9.08 ± 1.9	D
(16551)	1991 RT14	10.0 ± 0.65	A
(17350)	1968 OJ	7.15 ± 0.83	S
(21867)	1999 TQ251	5.44 ± 0.70	-*
(22689)	1998 QQ84	-1.31 ± 0.49	Ch
(23248) Batchelor	**2000 WW178**	**20.6 ± 0.42**	**A**
(27378)	**2000 EG55**	**11.9 ± 0.52**	**-***
(31056)	**1996 RK25**	**12.3 ± 0.22**	**S***
(31786)	1999 KO13	10.5 ± 0.20	D
(33693)	1999 KA	8.75 ± 0.42	D
(36249)	**1999 VT178**	**11.3 ± 0.55**	**L**
(40131)	1998 QJ48	7.93 ± 0.31	D
(67141)	**2000 AC169**	**10.9 ± 0.29**	**L**
(81819)	**2000 KS35**	**16.0 ± 1.04**	**-***
(85911)	**1999 CY91**	**11.2 ± 0.77**	**-***
(106063)	**2000 SR319**	**11.3 ± 0.15**	**L**
(158762)	2003 RS	7.85 ± 1.74	D
(246945)	1999 RP116	7.78 ± 2.89	D

Note. — For each asteroid, we report the name, provisional designation, spectral slope (as measured over the 0.35 - 1.0 μm range), and Bus-DeMeo classification. **Bolded** entries indicate steep sloped asteroids, e.g. those whose spectral slopes exceed the average spectral slope of an R group Trojan (10.7 % /100 nm) in the visible. Note that classification in the visible is not definitive, and more certain classification requires near-infrared spectral coverage. Classifications marked with an asterisk (*) were derived using both visible and infrared data (See Section 2.4)

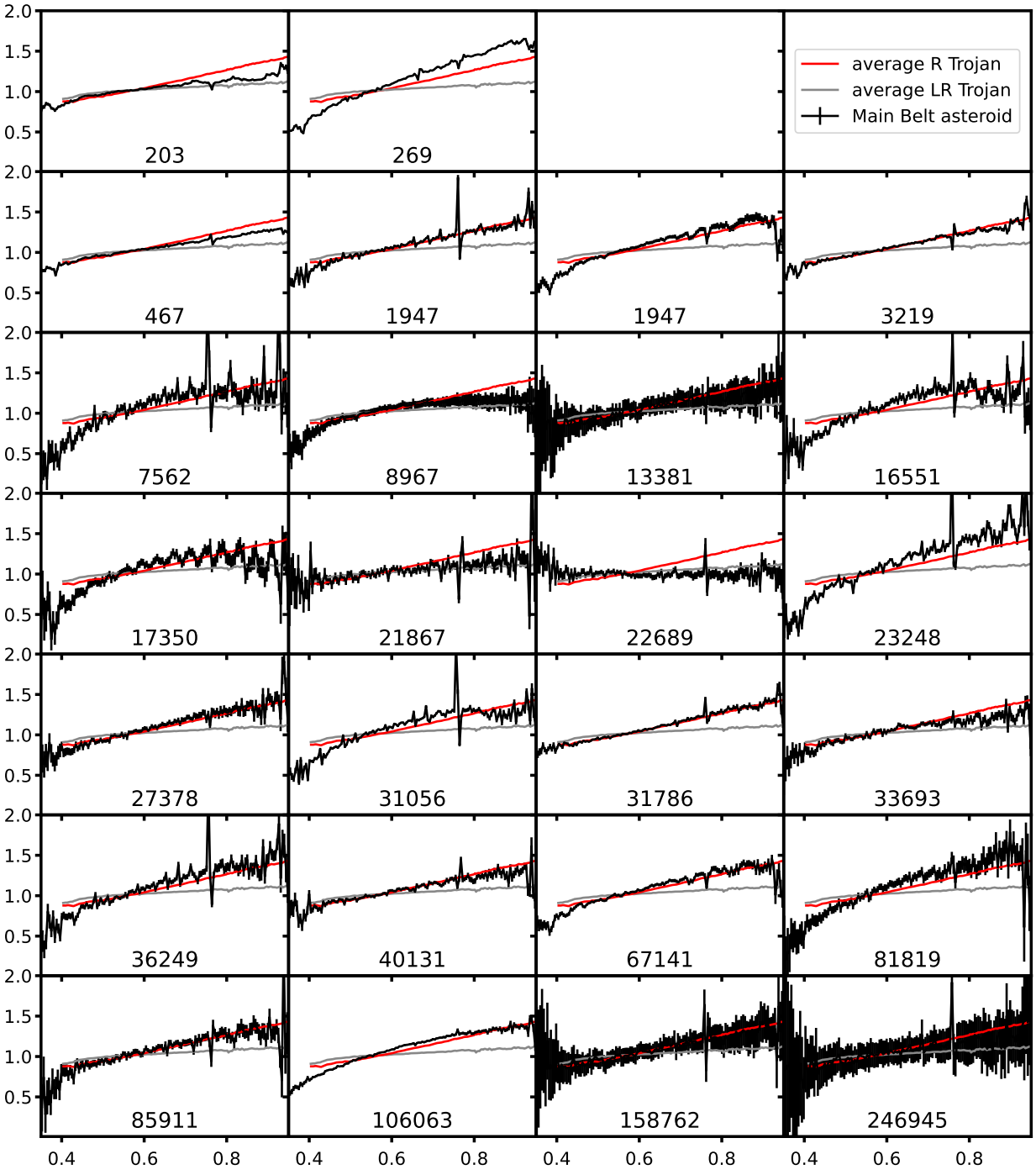

Figure 4.3 Visible reflectance spectra of all candidate red objects observed with the LDT. Spectra from the 2021 and 2022 apparitions of (1947) Iso-Heikila are plotted seperately. All spectra are normalized to 1 at 0.55 μm and displayed at the same scale to enable direct visual comparison. Each spectrum is plotted alongside the average R and LR group Trojan reflectance spectrum from Emery et al. (2010).

Table 4.5. Confirmation Rates of 'Red' Asteroid Subpopulations

Instrument	Sub-population	Number Observed	Confirmation Rate (%)	Extrapolated Population
IRTF	D-type	4	27	16
	Steep Sloped	10	67	40
	Total	15		
LDT	D-type	10	53	31
	Steep Sloped	10	53	31
	Total	19		
IRTF + LDT	D-type	12	43	26
	Steep Sloped	17	61	36
	Total	28		

Note. — We report the number of confirmed candidate objects in each 'red' sub-population (see text) among the IRTF, LDT, and complete spectral datasets. Confirmation rates are calculated by dividing the number of observed SDSS MOC 'red' candidate objects belonging to each subpopulatation by the total number of observed SDSS MOC 'red' candidate objects observed using each facility. Extrapolated population size is given by multiplying these confirmation rates by the total number (60) of SDSS MOC objects that met our strictest criteria for inclusion as 'red' candidate objects.

confirmation rate for D-type asteroids. Our confirmation rate for steep sloped asteroids is higher ($\sim 50\%$), reflecting the fact that not all steep sloped asteroids classified as D-types.

Not all of the asteroids observed in this study were identified as candidates according to the strictest set of criteria–five asteroids we observed were drawn from a list of backup objects with at least one steep slope observation but displayed high variability in slope and/or high albedos. Due to the small sample size of objects from this list, we refrain from drawing any conclusions about the confirmation rates of D-type, steep slope, or Main Belt Trojan analog asteroids among asteroids with inconsistently red slopes. However, we note that three of the five asteroids from the backup list had steeply red visible and/or near-infrared slopes, and one, (467) Laura, also classified as a D-type.

Our confirmation rates can be used to estimate the reliability of using SDSS MOC data to measure the spectral slopes of asteroids (See Figure 4.4). We observed a total of 23 asteroids drawn from the SDSS MOC. Comparing the range of slopes measured in the MOC to the range of slopes associated with measurement error from the LDT, we find that 10 asteroids show an overlap in measured slope ranges. A total of 12 asteroids have shallower (e.g. bluer) slopes in the LDT data than predicted by the MOC and 1 asteroid has a steeper (e.g. redder) slope in the LDT data than predicted by the MOC. This distribution suggests that SDSS MOC data tends to over-estimate spectral slopes. Discrepancies in slope between the LDT and SDSS MOC may be due to rotational variability in slope intrinsic to the object, like the variability in slope observed by Souza-Feliciano et al. (2020) among the Jupiter Trojans. However, the observed bias of the SDSS MOC observations towards overestimating the red slopes of asteroids suggests a bias in experimental design. To identify steeply red sloped candidates, we corrected SDSS MOC photometry to solar colors, which does not account for the potential reddening due to atmospheric extinction. Accounting for atmospheric reddening at increased airmasses (i.e. Fukugita et al. (1996)) or using solar analog colors measured at airmasses comparable to asteroid observations may increase the accuracy of spectral slope measurements based on SDSS MOC photometry. Among the 23 candidates observed, we note that only one asteroid predicted to have a high slope has a negative (i.e. blue) slope as observed by the LDT. This asteroid, (22689) 1998 QQ84 was observed only once in the SDSS MOC catalog, so we particularly caution against basing asteroid spectral slope measurements on single SDSS MOC observations.

Since the SDSS MOC data does not cover wavelength ranges longer than 0.9 μm, we refrain from directly comparing spectral slopes measured by the IRTF to those predicted from the SDSS MOC data. Many asteroid taxa show a change in slope from visible to near-infrared wavelengths, particularly primitive taxa like the D-types. Additionally, highly space weathered S-types can have steep spectral slopes in the visible that do not continue into the near-IR. Therefore, we caution against extrapolating visible slopes to the near-infrared. The asteroid (31056) 1996 RK25 demonstrates that steep visible slopes do not always indicate

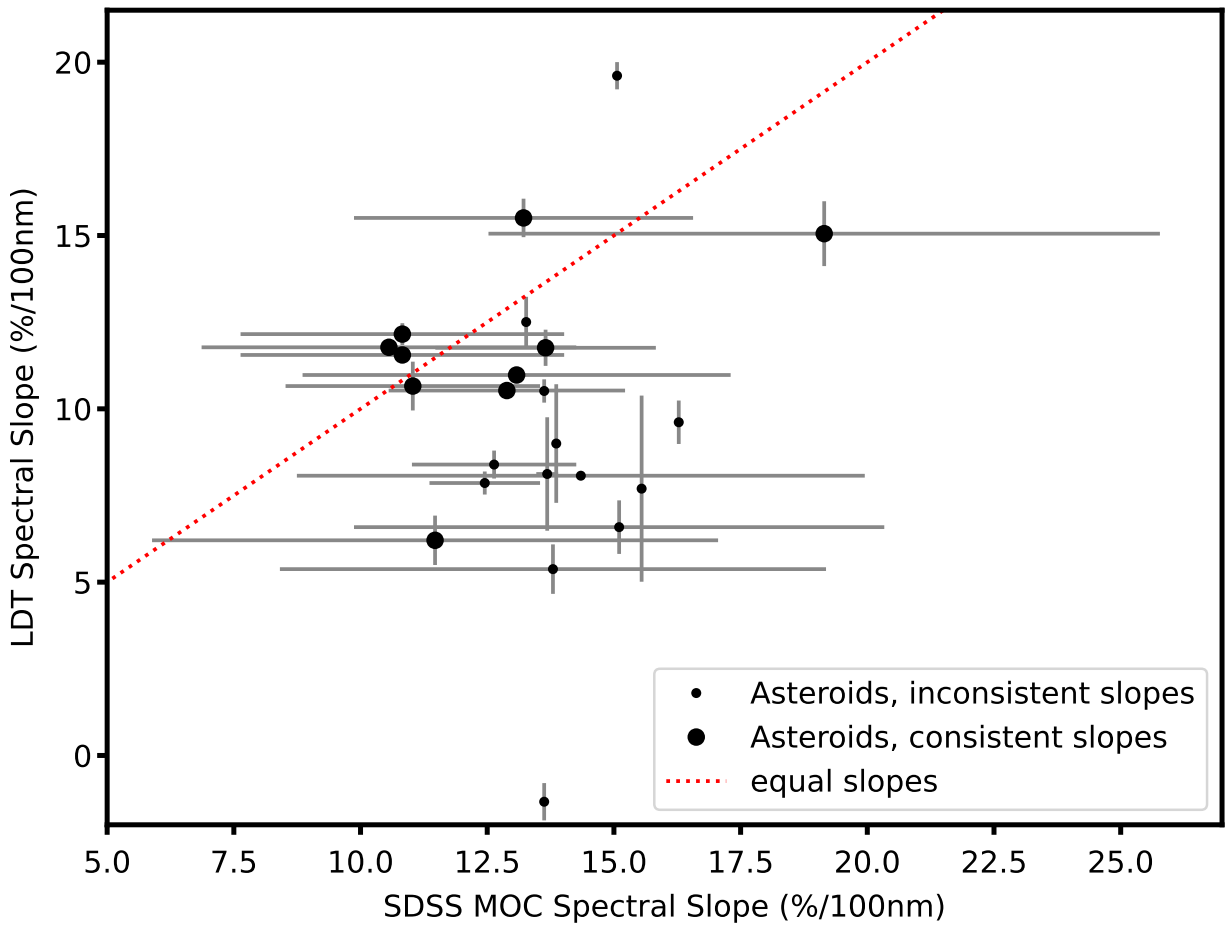

Figure 4.4 Comparison of asteroid spectral slopes measured using the SDSS MOC (x-axis) and Lowell Discovery Telescope (y-axis). Error bars in the x-direction represent the full range of slopes measured in the SDSS MOC for asteroids with multiple slope measurements. Error bars in the y-direction represent errors in slope corresponding to measurement uncertainty associated with the Lowell Discovery Telescope spectra. The dotted line represents the location of the 1:1 line where SDSS MOC and LDT slope measurements would be equal. Those asteroids plotted with a large marker show an overlap in measured slope ranges in the SDSS MOC and LDT data, those asteroids plotted with a small marker do now show an overlap in measured slope ranges between the two datasets.

steep near-infrared slopes. The range of visible slopes of (31056) 1996 RK25 predicted by SDSS photometry was 6.90 - 14.2 %/nm. In the LDT data, we measured a visible spectral slope of 12.3 %/nm, which non-uniquely indicated this object was a D-type. However, when we observed (31056) 1996 RK25 with the IRTF the prominent 1- and 2-μm absorptions in its infrared spectrum ruled out this interpretation. When the visible and near-infrared spectra were combined, the ambiguity in classification resolved, revealing (31056) 1996 RK25 is an Sw asteroid, with the w indicating a steep red slope that may be due to space weathering (DeMeo et al. (2009)). This example underscores the importance of including both visible and near-infrared wavelength regions in spectral classification to resolve potential ambiguity in spectral classification that cannot be addressed with visible-wavelength SDSS MOC photometry alone.

In addition to the candidate 'red' objects identified using the SDSS MOC, we also observed the asteroids (203) Pompeja and (269) Justitia following the 2021 discovery that these asteroids had extremely red, TNO-like slopes (Hasegawa et al. (2021)). Our data confirm the extremely red slope of (269) Justitia, but curiously, both IRTF and LDT observations of (203) Pompeja show this object has a spectral slope more typical of an X-type asteroid. Variations in slope on (203) Pompeja have also been noted in Hasegawa et al. (2022), which suggests differences in sub-observer longitude may be responsible for spectral slope variation, with some regions of (203) Pompeja exhibiting steeply red slopes. The geometric albedo for (203) Pompeja obtained by NEOWISE is 0.036 (Mainzer et al. (2019)), making (203) Pompeja a P-type asteroid in our observations.

Dynamical accounts of Solar System formation posit that the distribution of asteroids in orbital element space reflects a combination of the primordial distribution of materials and later modification caused by the preferential delivery of material from different regions of the protosolar nebula to the Main Belt. In Walsh et al. (2012), the predominance of S-type asteroids in the inner Main Belt and C-type asteroids in the outer Main Belt are explained as a consequence of Jupiter's inward migration (in accordance with the Grand Tack model) implanting primitive asteroids from beyond the initial, compact orbit of Saturn into the Main Belt. Similarly, Levison et al. (2009) demonstrates that the subsequent outward orbital migration of the giant planets into the proto-Kuiper Belt ($\sim 16-30$) AU resulted in the preferential delivery of primitive D- & P-type asteroids originating from same source region as the TNOs to the outer Main Belt. In contrast to the predictions of these models, we observe a lack of observed correlations between the orbital elements a, e, and i and spectral slope. We also observe a lack of correlation between the orbital elements a, e, and i and D-type classification. This result suggests that at the relatively small asteroid sizes sampled by this survey, steep slope asteroids are thoroughly mixed throughout the Main Belt. This result is consistent with DeMeo & Carry (2013), which demonstrated that while a gradient in taxonomic types exists for large (> 100 km) asteroids, this taxonomic gradient is much less pronounced for small asteroids. The detection of unexpected D-types in the inner Main Belt (DeMeo et al. (2014)) also supports this conclusion. This

size dependence suggests that after primitive D- & P-types were delivered to the Main Belt from their hypothesized parent population in the proto-Kuiper Belt, mechanisms of orbital evolution preferentially acted on smaller asteroids. These mechanisms may include the Yarkovsky effect, which preferentially alters the semi-major axes of smaller asteroids (Vokrouhlickỳ et al. (2000)) and mutual gravitational scattering during close encounters. The characteristic "V" shapes of asteroid families when plotted in semi-major axis and H-mag (a proxy for asteroid diameter) space demonstrate that a variety of mechanisms, including the Yarkovsky effect, gravitational scattering, and the generation of impact fragments lead to the preferential migration in semi-major axis of small asteroids from their probable parent bodies (Nesvornỳ et al. (2015)).

We also note a diversity in near-infrared spectral shape among steeply sloped asteroids. Many steeply sloped asteroids (e.g. (27378) 2000 EG55, (81819) 2000 KS35, and (85911) 1999 CY91) are not well matched by any of the taxonomic types in the Bus-DeMeo system. Objects like these, and the steeply red-sloped asteroid (269) Justitia may be better classified using taxonomic systems developed to classify extremely red objects, such as TNO color classifications (e.g. Perna et al. (2010)). In Hasegawa et al. (2021), (269) Justitia is classified as similar to the IR and RR TNO populations. The presence of asteroids like (269) Justitia in the Main Belt hint that the delineation between TNOs and asteroids is not entirely clear cut. Considering the asteroids and TNOs together in our evaluation of the spectra of primitive objects may improve our classification, and thus understanding, of the relationships between these liminal objects.

Some steeply sloped asteroids in our sample show a gradual shallowing of spectral slopes at long ($> 1.5\mu$m) wavelengths typical of D-type asteroids, while others show a steep and linear spectral slope that remains relatively constant over the entire near-infrared (0.7-2.5 μm) region of the spectrum. This diversity in spectral shape is further underscored by the 0.85 - J and J - K color indices of the steeply sloped asteroids. As noted in Section 4.3, there is a subpopulation of steeply sloped asteroids that have higher J - K color values than would be predicted based on their 0.85 - J color. A higher J - K color index indicates that the slopes of these asteroids do not fall off as much as expected at long wavelengths. These asteroids may represent a new, steeply red-sloped taxonomic type with spectral slopes similar to D-types from 0.75 - 1.5 μm, but higher slopes in the 1.5 - 2.5 μm region. For clarity, we refer to this proposed class of asteroids as Δ-type asteroids. The linear slopes of Δ-type asteroids in the near-IR distinguish them from D-type, R group Trojans as well as the RR, IR, and BR taxonomic types identified by (Perna et al. (2010)) among Centaurs and TNOs, which all show a flattening in slope at long ($> 1.5\mu$m) wavelengths.

If the Δ-type subpopulation represents a previously unrecognized population of red-sloped asteroids, its existence could challenge the assumption that all steeply red sloped asteroids originate in the outer Solar System. The steep red slopes of Centaurs and TNOs at short wavelengths ($< 1.5\mu$m) and subsequent flattening at longer wavelengths ($> 1.5\mu$m) are well matched by organic compounds irradiated in the lab

and are consistent with the chemical species predicted to be present in the TNO region (Hudson et al. (2008); Brunetto et al. (2006)). Similarly, the observed colors of the Jupiter Trojans can be explained by the initial formation of a TNO-like, organic-rich irradiation crust in the proto-Kuiper Belt followed by a neutralization in slope caused by a loss of volatile ices during the Trojan's migration to their current locations closer to the Sun (Wong & Brown (2016)). In contrast, the consistently linear slopes of the proposed Δ-type asteroids are not well matched by irradiated organics. Consistently linear, steeply-red slopes are instead found on space weathered surfaces in the inner Solar System, including mature, heavily irradiated lunar soils (Gaffey (2010)) and the moons of Mars (Rivkin et al. (2002)). The resemblance of Δ-type asteroids to the space weathered surfaces of the moons of Earth and Mars challenges the interpretation that these asteroids are primitive asteroids originating from beyond the orbit of Jupiter. Lunar soils, for example, are not primitive as they have undergone chemical processing and differentiation within the early lunar magma ocean Wieczorek et al. (2006). While the origins of the martian moons Phobos and Deimos are still debated, some authors suggest these moons formed in-situ in a circum-Martian debris disk, while others posit they are captured D-type asteroids based on their resemblance to Trojans and other Main Belt D-types (Rosenblatt (2011)). Comparison of the spectra of Phobos and Deimos to the Δ-type asteroids may shed light on the origins of these enigmatic moons.

The existence of Δ-type asteroids and their possible inner (e.g. interior to Jupiter) Solar System origins agrees with the results of Gartrelle et al. (2021b), which explores the subtle differences in spectral appearances of D-type asteroids at different heliocentric distances. That work found that Trojans tended to have lower slopes at long wavelengths than Main Belt asteroids. Similarly, D-type asteroids at lower heliocentric had steeper slopes in the 1.5–1.8 μm and 2.0–2.45 μm segments than those at higher heliocentric distances (Gartrelle et al. (2021b)). The increased prevalence of asteroids with steep slopes in the 1.5-2.45 μm region could indicate that these asteroids are sourced from regions interior to the orbit of Jupiter. Alternatively, increasing 1.5-2.45 μm slopes at lower heliocentric distances may indicate steepening slopes are a product of exposing primitive, TNO-like material to the increased thermal and ionizing radiation environment closer to the Sun. Laboratory studies of how organic irradiation crusts evolve spectrally when exposed to the thermal environment of the Main Belt could provide support for the idea that asteroids with linearly increasing, steep red slopes share a parent population with the typical D-type asteroids in the outer Main Belt and Trojan population. Particularly, if the loss of volatile compounds at the higher temperatures expected in the inner Main Belt result in a steepening in the 1.5-2.45 μm spectral region, the subtle differences in slope between Δ-type and D-type asteroids may be explained by differences in thermal histories.

4.5 Conclusions

Using the Sloan Digital Sky Survey's Moving Object Catalog, we identified 60 'red' candidate objects with spectrophotometric slopes exceeding the average slope of the R group Trojans. Using the NASA IRTF and the Lowell Discovery Telescope we conducted a survey to determine the spectral slopes and taxonomic classifications of 28 of these candidate objects to verify their steep spectral slopes and compare their spectra to those of Jupiter Trojans and other steeply red Solar System objects. We find that using our selection criteria, $\sim 50\%$ of candidate 'red' objects in the SDSS MOC have slopes equal to or exceeding the slope of the average R group Trojan. Examining the distribution of orbital elements of these objects, we find no obvious correlations between semimajor axis (a), eccentricity (e), and inclination (i) and spectral slope, indicating steeply red sloped objects are well mixed within the Main Belt. We additionally identify a diversity in spectral appearance among steeply sloped asteroids, which suggests multiple sub-types of red-sloped asteroids are present within the Main Belt. This spectral diversity among red-sloped asteroids hints at a multiplicity of origins for spectrally red-sloped material within the Main Belt. Further explorations of the visible and near-infrared spectra of these objects and integration of classification methods developed for asteroids with those developed for trans-Neptunian objects and Centaurs will lead to a greater understanding of the population of unusually red-sloped Main Belt asteroids.

4.6 Acknowledgements

The initial list of SDSS MOC candidate objects was compiled by Dr. Cristina Thomas. The IRTF observations of (203) Pompeja were taken by Lauren McGraw. This material is based upon work supported by the National Aeronautics and Space Administration under Grant No. 80NSSC20K0671 issued through Science Mission Directorate via the ROSES-2019 Solar System Observations program.

These results made use of the Lowell Discovery Telescope (LDT) at Lowell Observatory. Lowell is a private, non-profit institution dedicated to astrophysical research and public appreciation of astronomy and operates the LDT in partnership with Boston University, the University of Maryland, the University of Toledo, Northern Arizona University and Yale University. The upgrade of the DeVeny optical spectrograph has been funded by a generous grant from John and Ginger Giovale and by a grant from the Mt. Cuba Astronomical Foundation. Lowell observatory sits at the base of the San Francisco Peaks, on homelands sacred to Native Americans throughout the region. We honor their past, present, and future generations, who have lived here for millennia and will forever call this place home.

The authors acted as visiting Astronomers at the Infrared Telescope Facility, which is operated by the University of Hawaii under contract 80HQTR19D0030 with the National Aeronautics and Space Administration. The authors wish to recognize and acknowledge the very significant cultural role and reverence that the summit of Maunakea has always had within the indigenous Hawaiian community. We are most fortunate to have the opportunity to conduct observations from this mountain.

This research has made use of data and/or services provided by the International Astronomical Union's Minor Planet Center. This research has made use of the SIMBAD database, operated at CDS, Strasbourg, France. Taxonomic type results presented in this work were determined, in whole or in part, using the Bus-DeMeo Taxonomy Classification Web tool by Stephen M. Slivan, developed at MIT with the support of National Science Foundation Grant 0506716 and NASA Grant NAG5-12355.

Chapter 5
Conclusions

Throughout this doctoral thesis, I have demonstrated how different spectroscopic techniques can be used to understand the population of primitive asteroids from different, complementary perspectives. Using ground-based, space-based, and airborne observations spanning the ultraviolet to the mid-infrared, I have investigated the spectra of D- & P-type asteroids across the middle Solar System, revealing a diversity in spectral features among primitive asteroids in each wavelength region.

In Chapter 2, *Ultraviolet Spectroscopy of Lucy Mission Targets with the Hubble Space Telescope*, I present the ultraviolet spectra of Jupiter Trojans (617) Patroclus-Menoeitus, (11351) Leucus, (3548) Eurybates, and (21900) Orus. The spectra of (617) Patroclus-Menoetius and (21900) Orus show evidence of an increase in reflectance or "bump" in the near ultraviolet from 0.35-0.3 μm. Unlike previously discovered ultraviolet features in Trojan spectra, this "bump" feature does not appear to be correlated with visible and near-infrared spectral slope. Thus, this feature may indicate a novel compositional constraint for the surfaces of Trojans. I explore this possibility by using Hapke optical modeling to demonstrate that this "bump" feature can be explained by Rayleigh scattering due to sub-microscopic opaque particles. I suggest sub-microscopic opaques contribute to space weathering on Trojan surfaces. In addition to providing new constraints on Trojan surface composition, these spectra will also provide context for the recently launched Lucy mission to the Jupiter Trojans when it arrives at the Trojan clouds in the late 2020s.

In Chapter 3, *Comparative Mid-Infrared Spectroscopy of Dark, Primitive Asteroids: Does Shared Taxonomic Class Indicate Shared Silicate Composition?*, I compare mid-infrared spectra of Main Belt asteroids obtained using the Stratospheric Observatory for Infrared Astronomy (SOFIA) and Spitzer Space Telescope to literature spectra of Jupiter Trojans. Both populations of D- and P-type asteroids show evidence of 10- and 20-μm silicate emission features in their spectra, with most Main Belt asteroids in our sample resembling the Trojans in terms of spectral contrast and the presence of specific spectral features associated with crystalline olivine and pyroxene. However, I also demonstrate a diversity in appearance of the 10-μm feature. The 10-μm feature of asteroids in our sample are preferentially skewed towards shorter wavelengths

than those of the Trojans. Additionally, I note the unusual appearance of (368) Haidea in the mid-infrared, with a 10-μm feature that indicates an olivine poor composition. These results demonstrate the need for mid-infrared observations, such as those from JWST, to supplement our understanding of primitive asteroids from visible and near-infrared spectroscopy in order to distinguish between asteroids that otherwise appear spectrally similar.

In Chapter 4, *The Abundance of Red-Sloped Asteroids in the Main Belt*, I use the NASA Infrared Telescope Facility (IRTF) and the Lowell Discovery Telescope (LDT) to conduct follow up observations of candidate "red" sloped asteroids identified using spectrophotometry from the Sloan Digital Sky Survey (SDSS) Moving Object Catalog (MOC). I demonstrate that the criteria used to identify "red" sloped asteroids in the SDSS MOC correctly identifies asteroids with slopes equal to or exceeding the average slope of the R group Trojans $\sim 50\%$ of the time. I also show that the distribution of these asteroids is not correlated with location of asteroids in orbital element space, indicating that these at small sizes, asteroids with steep red slopes are relatively well mixed throughout the Main Belt. I further draw attention to the subtle spectral difference between different subpopulations of red sloped asteroids. As with the results of Ch. 3, these differences subtle differences suggest that the primitive asteroid population is more spectrally diverse than previously noted.

Taken together, these results demonstrate spectral diversity is present among D- & P-type asteroids throughout the electromagnetic spectrum. The variation in spectral features revealed by spectroscopy in different wavelength regions hints at underlying compositional diversity within the D- & P-type populations. In turn, compositional variability points towards difference in formation conditions among various D- & P-type subpopulations. In the ultraviolet, the presence of the "bump" feature in the R-group Trojan (21900) Orus and the LR-group Trojan (617) Patroclus-Menoetius is indicative of the presence of a space weathering agent present on the surfaces of (21900) Orus and (617) Patroclus-Menoetius that is absent from the surfaces of (3548) Eurybates and (11351) Leucus. This space weathering agent is demonstrably distinct from the chemical species responsible for the red spectral slopes of the Trojans as the presence of the UV feature is not correlated with VNIR spectral slope. Similarly, the mid-infrared spectra of D-type asteroids (267) Tirza, (368) Haidea, and (944) Hidalgo demonstrate that a shared VNIR taxonomic classification does not guarantee a shared silicate composition. (368) Haidea is a particularly olivine-poor D-type in contrast to (267) Tirza and (944) Hidalgo. This observation could indicate (368) Haidea formed in a particularly olivine-depleted region of the Solar System and distinct from the formation region(s) of (267) Tirza and (944) Hidalgo. Close examination of the VNIR spectra of steeply sloped red Main Belt asteroids also reveals multiple ways an asteroid can have a red slope. Some steeply red-sloped Main Belt asteroids show a flattening in slope longwards of 1.5 μm, consistent with the spectra of irradiated organics, while other steeply red-sloped Main

Belt asteroids retain a relatively linear slope throughout the near-IR range, similar to highly weathered lunar surfaces. The mechanisms responsible for these two reddening processes, irradiation simple organics leading to the formation of complex hydrocarbons and the formation of iron nanoparticles, point to distinct formation regions for these two sub-classes of steeply red sloped asteroids.

That the classes of primitive D- & P-type asteroids are more complex than initially thought is not surprising given that compositional variation among other taxa of asteroids has been demonstrated. For instance, the presence of the 0.7 μm and 3.0μm hydration features have been used to further identify the formation regions of subpopulations of C-complex asteroids (Bus & Binzel (2002); Takir & Emery (2012)) and link these asteroid subpopulations to specific classes of chondritic meteorites (Potin et al. (2020)). The deep 1- and 2- μm silicate bands present in the spectra of S-complex asteroids has allowed for detailed linkages between sub-classes of S-type asteroids observed remotely to specific meteorites examined in the lab (Gaffey et al. (1993)). Therefore, it is reasonable to expect a diversity in compositions and origins among the D- & P-types, too, given the rich complexities present in the spectra of other asteroid taxa. However, understanding the complexities of D- & P-type asteroids is frustrated by the subtly featured VNIR spectra of D- & P-types when compared to the relatively feature-rich C- and S-type asteroids. By expanding spectroscopic investigations beyond the VNIR, we can begin to identify the extent of spectral variation present among the D- & P-type asteroids. Continuing investigations from the UV to the mid-IR will only deepen our understanding of the breadth of spectral variation present. Understanding the mechanisms behind spectral variation among D- & P-type asteroids will lead to a more thorough understanding of the varied origins of primitive asteroids and reveal the early Solar System histories preserved by these enigmatic asteroids.

References

Beck, P., Garenne, A., Quirico, E., et al. 2014, Icarus, 229, 263, doi: https://doi.org/10.1016/j.icarus.2013.10.019

Bendjoya, P., Cellino, A., Di Martino, M., & Saba, L. 2004, Icarus, 168, 374, doi: https://doi.org/10.1016/j.icarus.2003.12.004

Bertin, E., & Arnouts, S. 1996, Astronomy and astrophysics supplement series, 117, 393, doi: 10.1051/aas:1996164

Bida, T. A., Dunham, E. W., Massey, P., & Roe, H. G. 2014, in Society of Photo-Optical Instrumentation Engineers (SPIE) Conference Series, Vol. 9147, Ground-based and Airborne Instrumentation for Astronomy V, ed. S. K. Ramsay, I. S. McLean, & H. Takami, 91472N, doi: 10.1117/12.2056872

Binzel, R. P., Rivkin, A. S., Stuart, J. S., et al. 2004, Icarus, 170, 259, doi: https://doi.org/10.1016/j.icarus.2004.04.004

Binzel, R. P., & Sauter, L. M. 1992, Icarus, 95, 222, doi: https://doi.org/10.1016/0019-1035(92)90039-A

Britt, D., & Pieters, C. 1994, Geochimica et Cosmochimica Acta, 58, 3905, doi: https://doi.org/10.1016/0016-7037(94)90370-0

Brown, A. J. 2014, Icarus, 239, 85, doi: https://doi.org/10.1016/j.icarus.2014.05.042

Brown, M., Schaller, E., & Fraser, W. 2011, The Astrophysical Journal Letters, 739, L60, doi: 10.1088/2041-8205/739/2/L60

Brown, M. E. 2016, The Astronomical Journal, 152, 159, doi: https://doi.org/10.3847/0004-6256/152/6/159

Brunetto, R., Barucci, M. A., Dotto, E., & Strazzulla, G. 2006, The Astrophysical Journal, 644, 646, doi: 10.1086/503359

Buie, M. W., Keeney, B. A., Strauss, R. H., et al. 2021, The Planetary Science Journal, 2, 202, doi: https://doi.org/10.3847/PSJ/ac1f9b

Bus, S., Gulbis, A., Elliot, J., et al. 2011, in EPSC-DPS Joint Meeting, 1834

Bus, S. J. 1999, Ph. D. Thesis, 311

Bus, S. J., & Binzel, R. P. 2002, Icarus, 158, 106, doi: https://doi.org/10.1006/icar.2002.6857

Cahill, J. T. S., Blewett, D. T., Nguyen, N. V., et al. 2012, Geophysical Research Letters, 39, doi: https://doi.org/10.1029/2012GL051630

Casagrande, L., Ramírez, I., Melendez, J., & Asplund, M. 2012, The Astrophysical Journal, 761, 16, doi: 10.1088/0004-637X/761/1/16

Cheng, E. S., & WFC3 Team. 1999, in American Astronomical Society Meeting Abstracts, Vol. 195, American Astronomical Society Meeting Abstracts, 85.06

Chihara, H., Koike, C., Tsuchiyama, A., Tachibana, S., & Sakamoto, D. 2002, Astronomy & Astrophysics, 391, 267, doi: https://doi.org/10.1051/0004-6361:20020791

Clark, B., Bus, S., Rivkin, A., Shepard, M., & Shah, S. 2004, The Astronomical Journal, 128, 3070

Clark, R. N., Swayze, G. A., Wise, R. A., et al. 2007, USGS digital spectral library splib06a, Tech. rep., US Geological Survey

Clark, R. N., Curchin, J. M., Jaumann, R., et al. 2008, Icarus, 193, 372, doi: https://doi.org/10.1016/j.icarus.2007.08.035

Clark, R. N., Cruikshank, D. P., Jaumann, R., et al. 2012, Icarus, 218, 831, doi: https://doi.org/10.1016/j.icarus.2012.01.008

Cloutis, E. A., McCormack, K. A., Bell, J. F., et al. 2008, Icarus, 197, 321, doi: https://doi.org/10.1016/j.icarus.2008.04.018

Cruikshank, D. P., Dalle Ore, C. M., Roush, T. L., et al. 2001, Icarus, 153, 348, doi: https://doi.org/10.1006/icar.2001.6703

Cushing, M. C., Vacca, W. D., & Rayner, J. T. 2004, Publications of the Astronomical Society of the Pacific, 116, 362, doi: 10.1086/382907

Cutri, R., Skrutskie, M., Van Dyk, S., et al. 2003, The IRSA 2MASS All-Sky Point Source Catalog

De Sanctis, M. C., Ammannito, E., Raponi, A., et al. 2015, Nature, 528, 241, doi: https://doi.org/10.1038/nature16172

DeMeo, F., & Carry, B. 2013, Icarus, 226, 723, doi: https://doi.org/10.1016/j.icarus.2013.06.027

DeMeo, F. E., Binzel, R. P., Carry, B., Polishook, D., & Moskovitz, N. A. 2014, Icarus, 229, 392, doi: https://doi.org/10.1016/j.icarus.2013.11.026

DeMeo, F. E., Binzel, R. P., Slivan, S. M., & Bus, S. J. 2009, Icarus, 202, 160

DeMeo, F. E., & Carry, B. 2014, Nature, 505, 629, doi: https://doi.org/10.1038/nature12908

Devogele, M., & Moskovitz, N. 2019, in EPSC-DPS Joint Meeting 2019, Vol. 2019, EPSC–DPS2019–841

Doressoundiram, A., Boehnhardt, H., Tegler, S. C., & Trujillo, C. 2008, The solar system beyond Neptune, 91

Dorschner, J., Begemann, B., Henning, T., Jaeger, C., & Mutschke, H. 1995, Astronomy and Astrophysics, 300, 503

Draine, B. 1985, The Astrophysical Journal Supplement Series, 57, 587

Dressel, L. 2021, Wide Field Camera 3 Instrument Handbook, Version 13.0

Emery, J., & Brown, R. 2004, Icarus, 170, 131, doi: https://doi.org/10.1016/j.icarus.2004.02.004

Emery, J., Cruikshank, D., & Van Cleve, J. 2006, Icarus, 182, 496, doi: https://doi.org/10.1016/j.icarus.2006.01.011

Emery, J. P., Burr, D. M., & Cruikshank, D. P. 2010, The Astronomical Journal, 141, 25, doi: https://doi.org/10.1088/0004-6256/141/1/25

Fayolle, M., Quirico, E., Schmitt, B., et al. 2021, Icarus, 367, 114574, doi: https://doi.org/10.1016/j.icarus.2021.114574

Fornasier, S., Dotto, E., Hainaut, O., et al. 2007, Icarus, 190, 622, doi: https://doi.org/10.1016/j.icarus.2007.03.033

Fukugita, M., Ichikawa, T., Gunn, J., et al. 1996, Astronomical Journal v. 111, p. 1748, 111, 1748

Gaffey, M. J. 2010, Icarus, 209, 564

Gaffey, M. J., Bell, J. F., Brown, R., et al. 1993, Icarus, 106, 573, doi: https://doi.org/10.1006/icar.1993.1194

Gail, H.-P. 2004, Astronomy & Astrophysics, 413, 571

Gartrelle, G. M., Hardersen, P. S., Izawa, M. R., & Nowinski, M. C. 2021a, Icarus, 354, 114043, doi: https://doi.org/10.1016/j.icarus.2020.114043

—. 2021b, Icarus, 363, 114295

Gilmour, C. M., Herd, C. D., & Beck, P. 2019, Meteoritics & Planetary Science, 54, 1951, doi: https://doi.org/10.1111/maps.13362

Gradie, J., & Tedesco, E. 1982, Science, 216, 1405

Grav, T., Mainzer, A. K., Bauer, J. M., Masiero, J. R., & Nugent, C. R. 2012, The Astrophysical Journal, 759, 49, doi: https://doi.org/10.1088/0004-637X/759/1/49

Grimm, R. E., & McSween Jr, H. Y. 1989, Icarus, 82, 244

Grundy, W., Noll, K., Buie, M., & Levison, H. 2018, Icarus, 305, 198, doi: https://doi.org/10.1016/j.icarus.2018.01.009

Guilbert-Lepoutre, A. 2014, Icarus, 231, 232, doi: https://doi.org/10.1016/j.icarus.2013.12.014

Gulbis, A. A., Elliot, J., Rojas, F., et al. 2010, in AAS/Division for Planetary Sciences Meeting Abstracts# 42, Vol. 42, 49–14

Hainaut, O., Boehnhardt, H., & Protopapa, S. 2012, Astronomy & Astrophysics, 546, A115, doi: https://doi.org/10.1051/0004-6361/201219566

Hamilton, V. E. 2000, Journal of Geophysical Research: Planets, 105, 9701, doi: https://doi.org/10.1029/1999JE001112

—. 2010, Geochemistry, 70, 7, doi: https://doi.org/10.1016/j.chemer.2009.12.005

Hapke, B. 1981, Journal of Geophysical Research: Solid Earth, 86, 3039

—. 1993, Theory of Reflectance Spectroscopy (Topics in Remote Sensing, vol. 3), Cambridge University Press, Cambridge

Hapke, B., Wells, E., Wagner, J., & Partlow, W. 1981, Icarus, 47, 361

Hargrove, K. D., Kelley, M. S., Campins, H., Licandro, J., & Emery, J. 2012, Icarus, 221, 453

Harris, A. W. 1998, Icarus, 131, 291

Hasegawa, S., Marsset, M., DeMeo, F. E., et al. 2021, The Astrophysical Journal Letters, 916, L6, doi: 10.3847/2041-8213/ac0f05

Hasegawa, S., DeMeo, F. E., Marsset, M., et al. 2022, The Astrophysical journal letters, 939, L9, doi: 10.3847/2041-8213/ac92e4

Hendrix, A. R., Vilas, F., & Li, J.-Y. 2016, Meteoritics & Planetary Science, 51, 105, doi: https://doi.org/10.1111/maps.12575

Henning, T. 2010, Annual Review of Astronomy and Astrophysics, 48, 0, doi: 10.1146/annurev-astro-081309-130815

Herter, T., Adams, J., Gull, G., et al. 2018, Journal of Astronomical Instrumentation, 7, 1840005, doi: 10.1142/S2251171718400056

Houck, J. R., Roellig, T. L., Van Cleve, J., et al. 2004, The Astrophysical Journal Supplement Series, 154, 18, doi: 10.1086/423134

Hudson, R., Palumbo, M., Strazzulla, G., et al. 2008, The Solar System Beyond Neptune, 507

Humes, O. A., Thomas, C. A., Emery, J. P., & Grundy, W. M. 2022, The Planetary Science Journal, 3, 190, doi: 10.3847/PSJ/ac8059

Ivezić, Ž., Juric, M., Lupton, R. H., Tabachnik, S., & Quinn, T. 2002, in Survey and Other Telescope Technologies and Discoveries, Vol. 4836, SPIE, 98–103, doi: https://doi.org/10.1117/12.457304

Ivezić, Ž., Tabachnik, S., Rafikov, R., et al. 2001, The Astronomical Journal, 122, 2749, doi: 10.1086/323452

Karlsson, O., Lagerkvist, C.-I., & Davidsson, B. 2009, Icarus, 199, 106, doi: https://doi.org/10.1016/j.icarus.2008.08.012

Kelley, M. S. 2021, sbpy. https://github.com/mkelley/mskpy

Kelley, M. S., Woodward, C. E., Gehrz, R. D., Reach, W. T., & Harker, D. E. 2017, Icarus, 284, 344, doi: https://doi.org/10.1016/j.icarus.2016.11.029

Khare, B., Thompson, W., Cheng, L., et al. 1993, Icarus, 103, 290

Khare, B. N., Sagan, C., Arakawa, E., et al. 1984, Icarus, 60, 127

Koike, C., Chihara, H., Tsuchiyama, A., et al. 2003, Astronomy & Astrophysics, 399, 1101, doi: https://doi.org/10.1051/0004-6361:20021831

Koike, C., Shibai, H., & Tuchiyama, A. 1993, Monthly Notices of the Royal Astronomical Society, 264, 654, doi: https://doi.org/10.1093/mnras/264.3.654

Kümmel, M., Walsh, J., Pirzkal, N., Kuntschner, H., & Pasquali, A. 2009, Publications of the Astronomical Society of the Pacific, 121, 59, doi: https://doi.org/10.1086/596715

Lamy, P., & Toth, I. 2009, Icarus, 201, 674, doi: https://doi.org/10.1016/j.icarus.2009.01.030

Lane, M. D., Glotch, T. D., Dyar, M. D., et al. 2011, Journal of Geophysical Research: Planets, 116, doi: https://doi.org/10.1029/2010JE003588

Lazzarin, M., Barbieri, C., & Barucci, M. 1995, The Astronomical Journal, 110, 3058

Levison, H. F., Bottke, W. F., Gounelle, M., et al. 2009, Nature, 460, 364, doi: https://doi.org/10.1038/nature08094

Levison, H. F., Olkin, C. B., Noll, K. S., et al. 2021, The Planetary Science Journal, 2, 171, doi: 10.3847/psj/abf840

Licandro, J., Campins, H., Kelley, M., et al. 2011, Astronomy & Astrophysics, 525, A34, doi: https://doi.org/10.1051/0004-6361/201015339

Lucey, P. G., & Noble, S. K. 2008, Icarus, 197, 348, doi: https://doi.org/10.1016/j.icarus.2008.05.008

Lucey, P. G., & Riner, M. A. 2011, Icarus, 212, 451, doi: https://doi.org/10.1016/j.icarus.2011.01.022

Luna, R., Satorre, M., Domingo, M., Millán, C., & Santonja, C. 2012, Icarus, 221, 186, doi: https://doi.org/10.1016/j.icarus.2012.07.016

Mainzer, A., Grav, T., Masiero, J., et al. 2011, The Astrophysical Journal, 736, 100, doi: https://doi.org/10.1088/0004-637X/736/2/100

Mainzer, A., Bauer, J., Cutri, R., et al. 2019, NEOWISE Diameters and Albedos V2.0, NASA Planetary Data System, doi: 10.26033/18s3-2z54

Marchis, F., Enriquez, J., Emery, J., et al. 2012, Icarus, 221, 1130, doi: https://doi.org/10.1016/j.icarus.2012.09.013

Marsset, M., DeMeo, F. E., Binzel, R. P., et al. 2020, The Astrophysical Journal Supplement Series, 247, 73, doi: https://doi.org/10.3847/1538-4365/ab7b5

Martin, A., Emery, J., & Loeffler, M. 2022, Icarus, 378, 114921, doi: https://doi.org/10.1016/j.icarus.2022.114921

Martin, A. C. 2022, Ph. D. Thesis

Martonchik, J. V., Orton, G. S., & Appleby, J. F. 1984, Applied optics, 23, 541

Marzari, F., & Scholl, H. 1998, Icarus, 131, 41

McAdam, M., Sunshine, J., Howard, K., & McCoy, T. 2015, Icarus, 245, 320, doi: https://doi.org/10.1016/j.icarus.2014.09.041

McCord, T. B., & Sotin, C. 2005, Journal of Geophysical Research: Planets, 110, doi: https://doi.org/10.1029/2004JE002244

McCoy, T. J., Mittlefehldt, D. W., & Wilson, L. 2006, Meteorites and the early solar system II

Meftah, M., Damé, L., Bolsée, D., et al. 2018, Astronomy & Astrophysics, 611, A1, doi: https://doi.org/10.1051/0004-6361/201731316

Mommert, M., Hora, J. L., Harris, A. W., et al. 2014, The Astrophysical Journal, 781, 25, doi: 10.1088/0004-637X/781/1/25

Morbidelli, A., Levison, H. F., Tsiganis, K., & Gomes, R. 2005, Nature, 435, 462, doi: https://doi.org/10.1038/nature03540

Morlok, A., Lisse, C., Mason, A., Bullock, E. S., & Grady, M. 2014, Icarus, 231, 338, doi: https://doi.org/10.1016/j.icarus.2013.12.018

Mueller, M., Marchis, F., Emery, J. P., et al. 2010, Icarus, 205, 505, doi: https://doi.org/10.1016/j.icarus.2009.07.043

Neese, C., E. 2017, ASTEROID TAXONOMY V1.0, NASA Planetary Data System, doi: https://doi.org/10.26033/e1p3-xm59

Nesvornỳ, D., Brož, M., Carruba, V., et al. 2015, Asteroids IV, 29, 7

Nesvornỳ, D., Vokrouhlickỳ, D., & Morbidelli, A. 2013, The Astrophysical Journal, 768, 45, doi: https://doi.org/10.1088/0004-637X/768/1/45

Noble, S. K., Pieters, C. M., & Keller, L. P. 2007, Icarus, 192, 629, doi: https://doi.org/10.1016/j.icarus.2007.07.021

Perna, D., Barucci, M. A., Fornasier, S., et al. 2010, Astronomy & Astrophysics, 510, A53, doi: https://doi.org/10.1051/0004-6361/200913654

Pieters, C. M., Taylor, L. A., Noble, S. K., et al. 2000, Meteoritics & Planetary Science, 35, 1101, doi: https://doi.org/10.1111/j.1945-5100.2000.tb01496.x

Pirani, S., Johansen, A., Bitsch, B., Mustill, A. J., & Turrini, D. 2019, Astronomy & Astrophysics, 623, A169

Potin, S., Beck, P., Usui, F., et al. 2020, Icarus, 348, 113826, doi: https://doi.org/10.1016/j.icarus.2020.113826

Rayner, J. T., Toomey, D., Onaka, P., et al. 2003, Publications of the Astronomical Society of the Pacific, 115, 362, doi: 10.1086/367745

Rivkin, A., Brown, R., Trilling, D., Bell Iii, J., & Plassmann, J. 2002, Icarus, 156, 64, doi: https://doi.org/10.1006/icar.2001.6767

Roig, F., Ribeiro, A., & Gil-Hutton, R. 2008, Astronomy & Astrophysics, 483, 911, doi: https://doi.org/10.1051/0004-6361:20079177

Rosenblatt, P. 2011, Astronomy & Astrophysics Review, 19, doi: 10.1007/s00159-011-0044-6

Rouleau, F., & Martin, P. 1991, The Astrophysical Journal, 377, 526

Rozehnal, J., Brož, M., Nesvorný, D., et al. 2016, Monthly Notices of the Royal Astronomical Society, 462, 2319, doi: https://doi.org/10.1093/mnras/stw1719

Sharkey, B. N., Reddy, V., Sanchez, J. A., Izawa, M. R., & Emery, J. P. 2019, The Astronomical Journal, 158, 204, doi: https://doi.org/10.3847/1538-3881/ab46c0

Sheppard, S. S. 2010, The Astronomical Journal, 139, 1394, doi: 10.1088/0004-6256/139/4/1394

Sheppard, S. S., & Trujillo, C. A. 2006, Science, 313, 511, doi: 10.1126/science.1127173

SOFIA/USRA. 2022a, FORCAST Basic Photometry. https://github.com/SOFIAObservatory/Recipes/blob/master/FORCAST-Basic_Photometry.ipynb

—. 2022b, FORCAST Grism Spectra: Basic Inspection and Assessment. https://github.com/SOFIAObservatory/Recipes/blob/master/FORCAST-Grism_Inspection.ipynb

Souza-Feliciano, A., De Prá, M., Pinilla-Alonso, N., et al. 2020, Icarus, 338, 113463, doi: https://doi.org/10.1016/j.icarus.2019.113463

Spitzer Science User Support and Instrument Teams and IRSA Science User Support Team. 2017, Spitzer Data Analysis Cookbook

Sultana, R., Poch, O., Beck, P., et al. 2023, Icarus, 395, 115492, doi: https://doi.org/10.1016/j.icarus.2023.115492

Takir, D., & Emery, J. P. 2012, Icarus, 219, 641, doi: https://doi.org/10.1016/j.icarus.2012.02.022

Tedesco, E., Noah, P., Noah, M., & Price., S. 2004, IRAS Minor Planet Survey V6.0, NASA Planetary Data System, doi: 10.26033/18s3-2z54

Tholen, D. J. 1984, Asteroid taxonomy from cluster analysis of photometry (The University of Arizona)

Tholen, D. J., & Barucci, M. A. 1989, Asteroids II, 298

Vernazza, P., Fulvio, D., Brunetto, R., et al. 2013, Icarus, 225, 517, doi: https://doi.org/10.1016/j.icarus.2013.04.019

Vinogradova, T. 2015, Monthly Notices of the Royal Astronomical Society, 454, 2436, doi: https://doi.org/10.1093/mnras/stv2115

Vokrouhlickỳ, D., Milani, A., & Chesley, S. 2000, Icarus, 148, 118, doi: https://doi.org/10.1006/icar.2000.6469

Wakeford, H., Sing, D., Stevenson, K., et al. 2020, The Astronomical Journal, 159, 204, doi: https://doi.org/10.3847/1538-3881/ab7b78

Walsh, K. J., Morbidelli, A., Raymond, S. N., O'brien, D., & Mandell, A. 2012, Meteoritics & Planetary Science, 47, 1941, doi: https://doi.org/10.1111/j.1945-5100.2012.01418.x

Warren, S. G. 1984, Applied optics, 23, 1206

—. 1986, Applied Optics, 25, 2650

Weissman, P. R., A'Hearn, M. F., McFadden, L., & Rickman, H. 2002, Asteroids III, 1, 669

Wenger, M., Ochsenbein, F., Egret, D., et al. 2000, Astronomy and Astrophysics Supplement Series, 143, 9, doi: https://doi.org/10.1051/aas:2000332

Westley, M. S., Baratta, G., & Baragiola, R. 1998, The Journal of chemical physics, 108, 3321

Wieczorek, M. A., Jolliff, B. L., Khan, A., et al. 2006, Reviews in mineralogy and geochemistry, 60, 221, doi: https://doi.org/10.2138/rmg.2006.60.3

Wong, I., & Brown, M. E. 2016, The Astronomical Journal, 152, 90, doi: https://doi.org/10.3847/0004-6256/152/4/90

Wong, I., Brown, M. E., Blacksberg, J., Ehlmann, B. L., & Mahjoub, A. 2019, The Astronomical Journal, 157, 161, doi: https://doi.org/10.3847/1538-3881/ab0e00

Wong, I., Brown, M. E., & Emery, J. P. 2014, The Astronomical Journal, 148, 112, doi: https://doi.org/10.1088/0004-6256/148/6/112

Wood, J. A. 1988, Annual Review of Earth and Planetary Sciences, 16, 53

Yang, B., Lucey, P., & Glotch, T. 2013, Icarus, 223, 359, doi: https://doi.org/10.1016/j.icarus.2012.11.025

Ye, Q.-Z., Hui, M.-T., Brown, P. G., et al. 2016, Icarus, 264, 48, doi: https://doi.org/10.1016/j.icarus.2015.09.003

Zellner, B., Tholen, D., & Tedesco, E. 1985, Icarus, 61, 355, doi: https://doi.org/10.1016/0019-1035(85)90133-2

Zolensky, M., Nakamura, K., Gounelle, M., et al. 2002, Meteoritics & Planetary Science, 37, 737, doi: https://doi.org/10.1111/j.1945-5100.2002.tb00852.x

Chapter 6

Appendices

6.1 Appendix A: Physical and Orbital Properties of Observed Asteroids

The material in this Appendix supplements the content of Chapter 4. I present the orbital elements of the asteroids observed over the course of the 2020B - 2023B observing semesters and demonstrate steeply red sloped asteroids are evenly distributed throughout the Main Belt at small sizes by noting a lack of correlation between orbital elements and measured spectral slopes.

Table 6.1. Physical and Orbital Properties of Observed Asteroids

Asteroid	Provisional Designation	a (AU)	e	i (deg.)	H (mag.)	Diameter (km)	Albdeo
(203) Pompeja	A879 SA	2.74	0.06	3.17	8.89	125	0.036
(269) Justitia	A887 SA	2.61	0.21	5.48	9.78	50.7	0.061
(467) Laura	A901 AA	2.95	0.11	6.44	10.9	39.5	0.037
(1947) Iso-Heikkila	1935 EA	3.15	0.04	11.9	11.4	31.6	0.049
(3248) Farinella	1982 FK	3.04	0.13	6.81	11.8	36.6	0.050
(5819) Lauretta	1984 UZ4	2.53	0.16	5.63	13.6	-	-
(7562) Kagiroino-Oka	1986 WO9	2.77	0.02	3.29	13.1	6.89	0.283
(8967) Calandra	4878 T-1	3.06	0.11	9.76	13.2	8.38	0.174
(9934) Caccioppoli	1985 UC	2.58	0.23	16.6	13.9	7.69	0.108
(13381)	1998 WJ17	3.99	0.21	4.20	12.5	15.7	0.103
(16551)	1991 RT14	2.77	0.11	15.3	13.3	7.8	0.179
(17350)	1968 OJ	2.75	0.14	13.2	14.4	-	-
(21867)	1999 TQ251	3.37	0.05	17.4	12.8	15.4	0.074
(22110)	2000 QR7	2.66	0.28	6.51	14.0	8.40	0.098
(22422) Kenmount Hill	1995 YO5	2.52	0.15	6.36	15.4	4.12	0.090
(22689)	1998 QQ84	3.09	0.13	12.9	13.9	-	-
(23248) Batchelor	2000 WW178	2.53	0.10	9.52	14.5	6.30	0.112
(23690)	1997 JD14	2.55	0.02	14.1	14.0	7.29	0.121
(25835) Tomzega	2000 EO20	3.19	0.08	15.3	13.3	12.2	0.090
(27378)	2000 EG55	3.18	0.11	9.86	13.7	8.99	0.105
(31056)	1996 RK25	2.64	0.13	14.8	13.7	-	-
(31499)	1999 CS64	3.15	0.09	15.9	12.8	15.3	0.054
(31786)	1999 KO13	2.66	0.08	10.9	13.8	8.61	0.127
(33693)	1999 KA	2.57	0.14	13.9	14.5	6.54	0.104
(36249)	1999 VT178	3.38	0.08	12.1	13.6	11.3	0.066
(40131)	1998 QJ48	3.00	0.06	3.53	13.7	9.11	0.093
(60378)	2000 AL165	2.93	0.16	11.0	14.0	7.12	0.139
(52628)	1997 WO3	2.63	0.05	2.49	14.7	-	-
(67141)	2000 AC169	2.74	0.16	7.95	14.7	4.63	0.143
(67244)	2000 EH58	3.40	0.08	8.78	13.3	12.5	0.059
(76391)	2000 FP7	3.03	0.19	12.2	14.4	7.38	0.051
(80052)	1999 JV62	3.13	0.21	15.9	14.2	4.14	0.24
(81819)	2000 KS35	2.66	0.26	6.17	15.7	-	-
(85911)	1999 CY91	2.67	0.18	5.64	15.2	-	-
(106063)	2000 SR319	3.13	0.23	16.9	13.4	-	-
(158762)	2003 RS	3.24	0.08	15.4	13.9	8.79	0.100
(246945)	1999 RP116	3.09	0.30	18.2	15.2	5.61	0.065

Note. — We list all the asteroids observed with the IRTF and/or LDT along with their names, provisional designations, semimajor axes (a) in AU, orbital eccentricity (e), orbital inclination (i) in degrees, H magnitude, diameter in km, and albedo. Orbital elements and H magnitudes are drawn from the JPL Horizons database, computed for Julian Date 2460000.5, diameters and albedos are drawn from the NEOWISE survey (Mainzer et al. (2019)) and are not available for entries marked with a '-'.

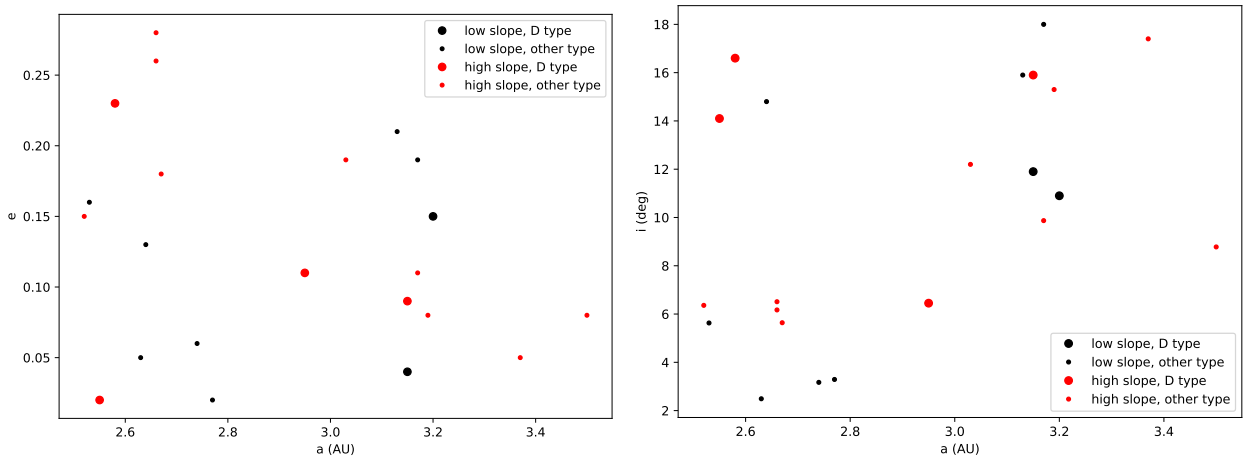

Figure 6.1 All asteroids observed by the IRTF plotted according to their orbital elements. In the left panel, semimajor axis (a, AU) is plotted with eccentricity (e). In the right panel, semimajor axis (a, AU) is potted alongside inclination (i, deg). Asteroids with spectral slopes greater than the average R group Trojan are plotted in red, those with lower slopes are plotted in black. Asteroids classified as D types are plotted with larger markers than those classified as all other types. There are no obvious trends in asteroid spectral classification in orbital element space, indicating D-types and steeply-sloped asteroids are well mixed within the Main Belt.

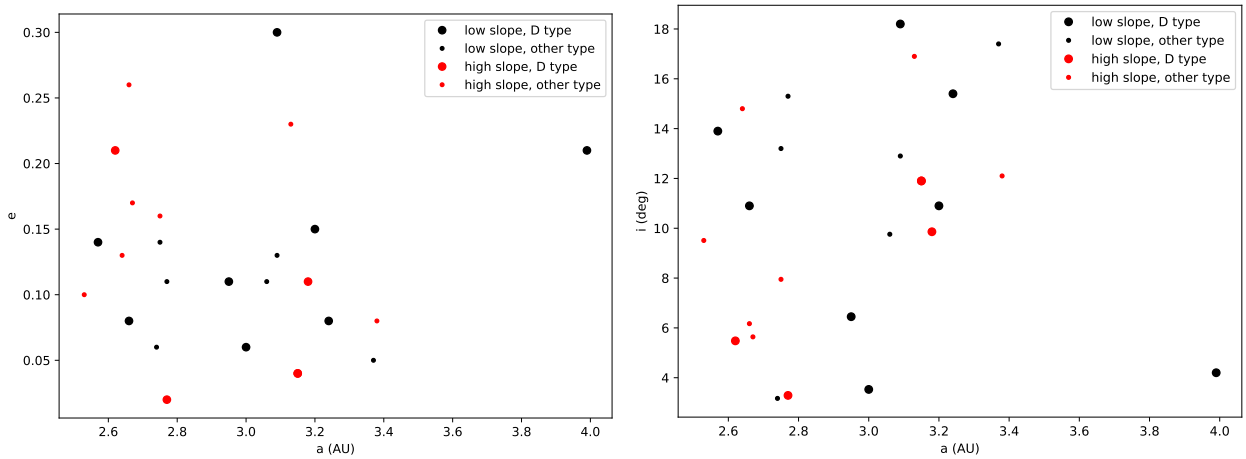

Figure 6.2 All asteroids observed by the LDT plotted according to their orbital elements. In the left panel, semimajor axis (a, AU) is plotted with eccentricity (e). In the right panel, semimajor axis (a, AU) is potted alongside inclination (i, deg). Asteroids with spectral slopes greater than the average R group Trojan are plotted in red, those with lower slopes are plotted in black. Asteroids classified as D types are plotted with larger markers than those classified as all other types. There are no obvious trends in asteroid spectral classification in orbital element space, indicating D-types and steeply-sloped asteroids are well mixed within the Main Belt.

6.2 Appendix B: Full List of Candidate Red Objects in the SDSS MOC

The material in this Appendix supplements the content of Chapter 4. The following list of asteroids represents the list of all asteroids in the Sloan Digital Sky Suvery Moving Object Catalog that met our criteria for survey inclusion (See Section 4.2.1).

Table 6.2. List of SDSS MOC "Red" Candidate Objects

Asteroid	a (AU)	e	i (deg.)	H (mag.)	Asteroid	a (AU)	e	i (deg.)	H (mag.)
1947	3.15	0.04	11.89	11.4	43957	2.55	0.15	8.51	14.6
3248	3.20	0.15	10.90	11.0	49603	3.03	0.04	4.23	14.0
7562	2.77	0.02	3.29	13.1	52628	2.63	0.05	2.49	14.7
8250	3.13	0.20	16.98	12.4	56181	2.65	0.13	6.47	14.8
8838	3.15	0.01	11.14	11.5	58981	2.64	0.27	3.12	16.3
8967	3.06	0.11	9.76	13.2	60378	3.17	0.19	18.00	13.9
9934	2.58	0.23	16.62	13.9	67141	2.75	0.16	7.95	14.7
13381	3.99	0.21	4.20	12.5	67244	3.50	0.08	8.78	13.3
13677	3.15	0.08	2.13	13.9	68156	3.07	0.07	13.31	14.2
16551	2.77	0.11	15.29	13.3	74549	3.11	0.23	15.31	14.1
22110	2.66	0.28	6.51	14.0	76391	3.03	0.19	12.23	14.4
22422	2.52	0.15	6.36	15.4	78152	3.08	0.34	15.62	13.7
22689	3.09	0.13	12.94	13.9	78569	3.22	0.13	14.34	14.2
23248	2.53	0.10	9.52	14.5	80052	3.13	0.21	15.95	14.2
23461	2.70	0.08	10.62	14.2	81819	2.66	0.26	6.17	15.7
23690	2.55	0.02	14.07	14.0	82050	3.12	0.22	15.87	13.8
24180	2.63	0.02	11.85	14.4	85911	2.67	0.18	5.64	15.2
25835	3.19	0.08	15.29	13.3	88541	2.65	0.12	16.40	14.7
26895	3.11	0.28	19.95	12.7	92326	3.96	0.25	5.52	13.2
27378	3.18	0.11	9.86	13.7	95563	3.19	0.17	15.28	14.4
28368	3.25	0.03	7.07	13.2	95981	2.69	0.27	12.21	15.3
30853	2.86	0.29	8.59	14.1	96574	3.11	0.23	15.17	14.4
31499	3.15	0.09	15.86	12.8	106063	3.13	0.23	16.87	13.5
31786	2.66	0.08	10.88	13.8	109714	3.10	0.07	15.31	14.3
33693	2.57	0.14	13.89	14.5	112478	3.10	0.20	15.36	14.4
34750	3.37	0.11	10.82	13.8	117121	2.99	0.12	15.44	14.7
36249	3.38	0.08	12.09	13.6	129104	3.09	0.15	17.84	14.8
40131	3.00	0.06	3.53	13.7	158762	3.24	0.08	15.37	13.9
42202	3.25	0.05	8.74	14.3	183564	3.10	0.21	21.92	14.5
42974	2.61	0.03	13.55	14.6	246945	3.09	0.30	18.22	15.2

Note. — We list all the asteroids observed with the IRTF and/or LDT along with their names, provisional designations, semimajor axes (a) in AU, orbital eccentricity (e), orbital inclination (i) in degrees, H magnitude. Orbital elements and H magnitudes are drawn from the JPL Horizons database, computed for Julian Date 2460000.5.